

AD-A044 801

SPERRY RESEARCH CENTER SUDBURY MASS

F/G 17/9

IMPULSE RESPONSE TARGET STUDY.(U)

SEP 77 C L BENNETT, R HIERONYMUS, H MIERAS

F30602-76-C-0209

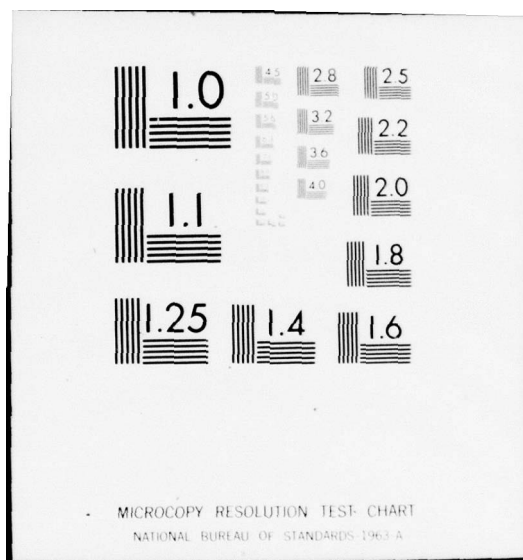
UNCLASSIFIED

RADC-TR-77-273

NL

1 OF 2
ADA044801





ADA 044801

RADC-TR-77-273
Final Technical Report
September 1977



IMPULSE RESPONSE TARGET STUDY

Sperry Research Center

Approved for public release; distribution unlimited.

AU NO. _____
DDC FILE COPY

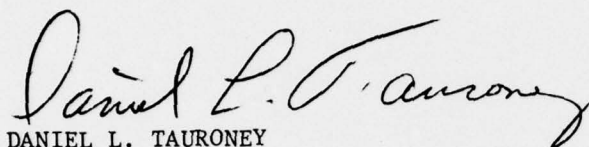
ROME AIR DEVELOPMENT CENTER
Air Force Systems Command
Griffiss Air Force Base, New York 13441

DDC
RECEIVED
OCT 3 1977
B

This report has been reviewed by the RADC Information Office (OI) and is releasable to the National Technical Information Service (NTIS). At NTIS it will be releasable to the general public including foreign nations.

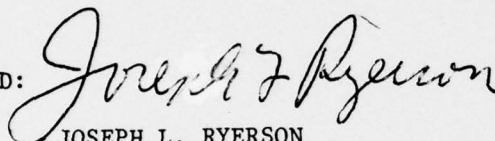
This report has been reviewed and is approved for publication.

APPROVED:



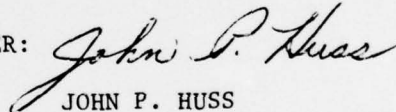
DANIEL L. TAURONEY
Project Engineer

APPROVED:



JOSEPH L. RYERSON
Technical Director
Surveillance Division

FOR THE COMMANDER:



JOHN P. HUSS
Acting Chief, Plans Office

If your address has changed or if you wish to be removed from the RADC mailing list, or if the addressee is no longer employed by your organization, please notify RADC (DAP) Griffiss AFB NY 13441. This will assist us in maintaining a current mailing list.

Do not return this copy. Retain or destroy.

UNCLASSIFIED

SECURITY CLASSIFICATION OF THIS PAGE (When Data Entered)

REPORT DOCUMENTATION PAGE		READ INSTRUCTIONS BEFORE COMPLETING FORM
1. REPORT NUMBER RADC-TR-77-273	2. GOVT ACCESSION NO.	3. RECIPIENT'S CATALOG NUMBER
4. TITLE (and Subtitle) IMPULSE RESPONSE TARGET STUDY.	5. TYPE OF REPORT & PERIOD COVERED Final Technical Report. 15 Apr 76 - 30 Apr 77.	6. PERFORMING ORG. REPORT NUMBER N/A
7. AUTHOR(s) C. L. Bennett R. Hieronymus H. Mieras	8. CONTRACT OR GRANT NUMBER(s) F30602-76-C-0209	10. PROGRAM ELEMENT, PROJECT, TASK AREA & WORK UNIT NUMBERS 62702F 45060575
9. PERFORMING ORGANIZATION NAME AND ADDRESS Sperry Research Center 100 North Road Sudbury MA 01776	11. CONTROLLING OFFICE NAME AND ADDRESS Rome Air Development Center (OCTM) Griffiss AFB NY 13441	12. REPORT DATE September 1977
14. MONITORING AGENCY NAME & ADDRESS (if different from Controlling Office) Same	13. NUMBER OF PAGES 122	15. SECURITY CLASS. (of this report) UNCLASSIFIED
16. DISTRIBUTION STATEMENT (of this Report) Approved for public release; distribution unlimited.	15a. DECLASSIFICATION/DOWNGRADING SCHEDULE N/A	
17. DISTRIBUTION STATEMENT (of the abstract entered in Block 20, if different from Report) Same		
18. SUPPLEMENTARY NOTES RADC Project Engineer: Daniel L. Tauroney (OCTM)		
19. KEY WORDS (Continue on reverse side if necessary and identify by block number) Space-Time Integral Equation; Impulse Response Augmentation Technique; Target Geometry; Impulse Response; Frequency Response		
20. ABSTRACT (Continue on reverse side if necessary and identify by block number) The space-time integral equation approach is extended to the problem of simple aircraft shapes. The target consisted of a cylindrical fuselage, and rectangular wings, stabilizers, and rudder. Calculations were compared to measurements. The inverse scattering problem was reformulated to take advantage of direct time domain method of solution. Solutions for the sphere, sphere capped cylinder, and flat end cylinder were developed.		

DD FORM 1473

EDITION OF 1 NOV 65 IS OBSOLETE

UNCLASSIFIED

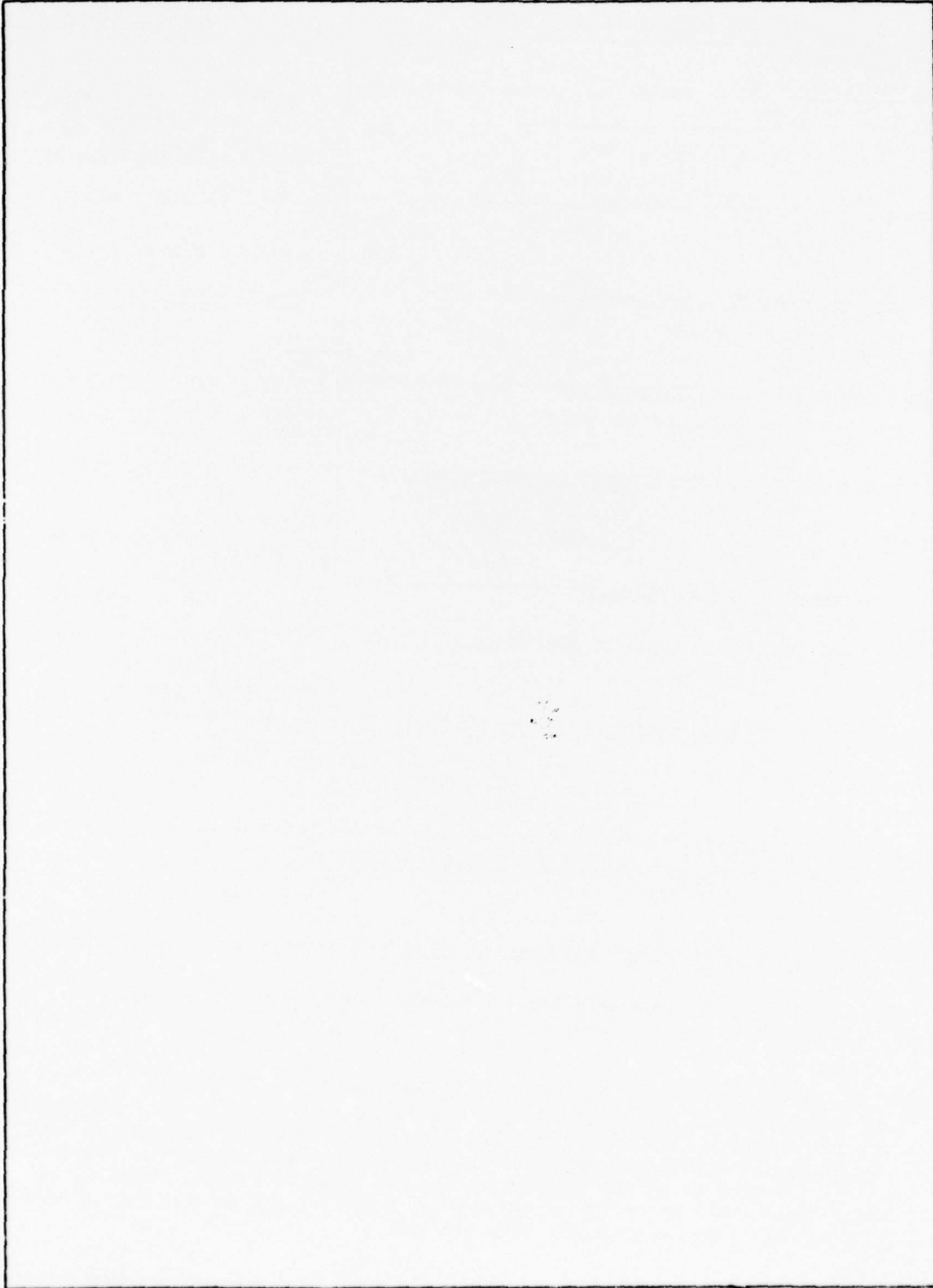
SECURITY CLASSIFICATION OF THIS PAGE (When Data Entered)

408199

1B

UNCLASSIFIED

SECURITY CLASSIFICATION OF THIS PAGE(When Data Entered)



UNCLASSIFIED

SECURITY CLASSIFICATION OF THIS PAGE(When Data Entered)

TABLE OF CONTENTS

<u>Section</u>		<u>Page</u>
1	INTRODUCTION	1
2	SPACE-TIME INTEGRAL EQUATION SOLUTION FOR SIMPLE AIRCRAFT MODELS	3
	2.1 General Problem	3
	2.2 Space-Time Integral Equation Solution	5
	2.2.1 Derivation of Space-Time Integral Equation	5
	2.3 Numerical Solution	12
	2.4 Time Domain Measurements	17
	2.4.1 Time Domain Measurement System	19
	2.4.2 Comparison of Measured and Calculated Responses	21
	2.5 Calculated Response of Aircraft Model	21
3	EXTENSION OF IMPULSE RESPONSE AUGMENTATION TECHNIQUE	31
	3.1 Review of the Impulse Response Augmentation Technique	31
	3.2 Application of Cylinder with Fins	37
	3.3 Results	44
4	TIME DOMAIN INVERSE SCATTERING - AXIAL INCIDENCE	55
	4.1 Derivation of Equations	56
	4.2 Numerical Solution	59
	4.3 Results	64
5	TIME DOMAIN INVERSE SCATTERING - OBLIQUE INCIDENCE	73
	5.1 General Problem	73
	5.2 Derivation of Inverse Scattering Equations	74
	5.3 First Order Ramp Response of Curvilinear Patch	81
	5.4 Numerical Solution Procedure	87
	5.5 Inverse Scattering Results	88
6	SUMMARY AND CONCLUSIONS	95
7	REFERENCES	99
8	APPENDIX	101
	8.1 Improved Space-Time Integral Equation Solution Technique	101
	8.2 Useful Differential Geometry Relationships	108
	8.3 Integration Over Self-Patch	110
	8.4 Transformation of Self-Patch Correction to the Incident H Coordinate System	114
	8.5 Projected Area of Newly Illuminated Region	116
	8.6 Initial Ramp Response of Specular Point	120

LIST OF ILLUSTRATIONS

Figure		Page
1	Aircraft sketch.	4
2	Simple aircraft model.	4
3	Equivalent problem of scattering from surfaces with fins attached.	6
4	Geometry of far scattered field.	18
5	Targets used for comparison of calculated and measured responses.	22
6	Comparison of calculated and measured responses, $a_n = 1$, $\alpha = 90^\circ$.	23
7	Comparison of calculated and measured responses, $a_n = 0.5$, $\alpha = 90^\circ$.	24
8	Comparison of calculated and measured responses, $\alpha = 0$, $a_n = 0.5$.	25
9	Calculated response of aircraft model at 0° , 30° , 60° , 90° .	26
10	Calculated response of aircraft at 90° , 120° , 150° , and 180° .	27
11	Comparison of responses of several finned cylinders at axial incidence.	29
12	Impulse response augmentation technique.	35
13	Geometry of cylinder with fin.	38
14	Smoothed impulse response of finned cylinder at various angles of incidence for TE polarization.	39
15	Smoothed impulse response of finned cylinder at various angles of incidence for TE polarization.	40
16	TE response of finned cylinder with radius a for 0° angle of incidence.	45
17	TE response of finned cylinder with radius a for 30° angle of incidence.	46

ACCESSION for	
NTIS	White Section <input checked="" type="checkbox"/>
DDC	Buff Section <input type="checkbox"/>
UNANNOUNCED	<input type="checkbox"/>
JUSTIFICATION	<input type="checkbox"/>
BY	
DISTRIBUTION/AVAILABILITY CODES	
Dist.	SPECIAL

LIST OF ILLUSTRATIONS (Cont.)

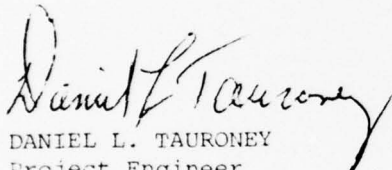
<u>Figure</u>		<u>Page</u>
18	TE response of finned cylinder with radius a for 60° angle of incidence.	48
19	TE response of finned cylinder with radius a for 90° angle of incidence	49
20	TE response of finned cylinder with radius a for 120° angle of incidence.	51
21	TE response of finned cylinder with radius a for 150° angle of incidence.	52
22	TE response of finned cylinder with radius a for 180° angle of incidence.	53
23	Geometry of rotationally symmetric scattering problem.	60
24	Direct time domain solution procedure.	62
25	Geometry of objects used for test of inversion procedure.	65
26	Far field ramp response (backscatter direction) for four objects tested.	66
27	Coordinate axes and view angle for perspective plots.	67
28	Contour estimates for a sphere.	68
29	Contour estimates for a cylinder with two sphere caps.	69
30	Contour estimates for a cylinder with a flat front end and a sphere-capped back end.	70
31	Contour estimates for a cylinder with a sphere-capped front end and a flat back end.	71
32	Inverse scattering of rotationally symmetric surface.	75
33	Unknown region ΔS for body with rotational symmetry, topview.	83

LIST OF ILLUSTRATIONS (Cont.)

<u>Figure</u>		<u>Page</u>
34	Self-patch integration at point inside ΔS .	83
35	Inverse scattering results — cross-section of sphere quadrant.	89
36	Inverse scattering results — sphere.	89
37	Inverse scattering results — cross-section of prolate spheroid.	91
38	Inverse scattering results — prolate spheroid.	92
39	Inverse scattering results — cross-section of sphere-capped cylinder.	93
40	Inverse scattering results — sphere-capped cylinder.	94
41	Projected area of newly illuminated region.	117

EVALUATION

The contractor was successful in computing the impulse response for a simple aircraft target at several aspect angles. The space-time integral approach has led to many new results associated with this model. These results can be used to obtain the radar response of these targets over the entire spectrum. This, in turn, can be used to compute the response of a target due to any incident radar waveform, regardless of wave shape or carrier frequency. The technique developed on the effort not only applies to the aircraft identification portion of TPO R2E but also to the analysis of targets which are constructed of composite materials and have radar absorbing materials incorporated in highly reflecting areas.


DANIEL L. TAURONEY
Project Engineer

SECTION 1

INTRODUCTION

This document is submitted as the final report in response to the requirements set forth in Contract No. F30602-76-C-0209 between the Sperry Corporate Research Center (SCRC), Sudbury, Massachusetts, and the Air Force Systems Command, Rome Air Development Center (RADC), Griffiss Air Force Base, New York. The primary objectives of this program, performed during the period 15 April 1976 through 30 April 1977 were to (1) improve and expand computer programs that had previously been delivered to RADC and (2) to extend the techniques previously developed by SCRC for computing the smoothed impulse response and the impulse response of relatively simple targets to complex targets which have fins, edges, and curved surfaces. The first objective was carried out and described in an interim report [1]. The second objective is discussed in detail in this report.

In Sec. 2 the space-time integral equation approach is extended to the case of simple aircraft models. Techniques are developed for computing the smoothed impulse response of a simple aircraft model consisting of a cylindrical fuselage, rectangular wings, rectangular stabilizers, and a rectangular rudder. The techniques are verified by comparison with direct time domain measurements. Smoothed impulse response results are displayed for the simple aircraft model at numerous aspect angles and specific portions of the response are related to scattering by local regions of the target. This appears to be the first solution technique that has been developed to handle these simple aircraft models.

The extension of the impulse response augmentation technique to cylinders with fins attached is discussed in Sec. 3. In particular, results are obtained for the example of a cylinder with square fins and a length to diameter ratio of 2:1 for a series of aspect angles that go from 0° to 180° .

In Sec. 4 the inverse scattering problem for axial incidence on a rotationally symmetric target is reformulated to take advantage of the

direct time domain method of solution. The previously developed iterative method was cumbersome and time consuming. The new "marching on in time" approach is faster and more straightforward. In Sec. 4 this new approach is described and demonstrated on a sphere, sphere-capped cylinder and a sphere-cap, flat-end cylinder and displayed on three dimensional plots. The results are compared with those obtained using the iterative technique.

The extension of the direct time domain approach to the inverse scattering problem to the case of rotationally symmetric targets at oblique incidence is discussed in Sec. 5. The techniques are developed and demonstrated on three targets. Conclusions are presented in Sec. 6.

SECTION 2

SPACE-TIME INTEGRAL EQUATION SOLUTION FOR SIMPLE AIRCRAFT MODELS

The space-time integral equation is valid for any conducting target shape and solution techniques have been developed for a number of important target classes [2-6]. In this section the solution techniques are developed for a simple aircraft model and verified by comparison of calculated and measured results. Sec. 2.1 describes the general problem and Sec. 2.2 describes the space-time integral equation and its solution for this new target class. The time domain measurement procedure is reviewed and the measured and calculated results are compared in Sec. 2.3. The calculated smoothed impulse response of the simple aircraft model is presented and discussed in Sec. 2.4.

2.1 GENERAL PROBLEM

The target class considered in this work consists of a conducting surface with protruding wings as shown in Fig. 1. The problem is to calculate the smoothed impulse response of this target class as a function of aspect angle. In order to make the problem amenable to solution by existing space-time integral equation techniques, the target is modeled as shown in Fig. 2. In this model the fuselage is represented by a conducting right-circular cylinder and the wings, stabilizers, and rudder are represented by thin, flat rectangular conducting plates.

In this work a smoothed impulse excitation is treated, yielding the target response well into the resonance region. High frequency augmentation techniques exist to extend the solution over the entire frequency domain. These techniques have been described earlier [4] and in Sec. 3 of this report.

In the numerical implementation described here, the direction of incidence is taken to be in the plane of symmetry and the polarization is taken to be perpendicular to the plane of symmetry (TE mode) as illustrated



FIG. 1 Aircraft sketch.

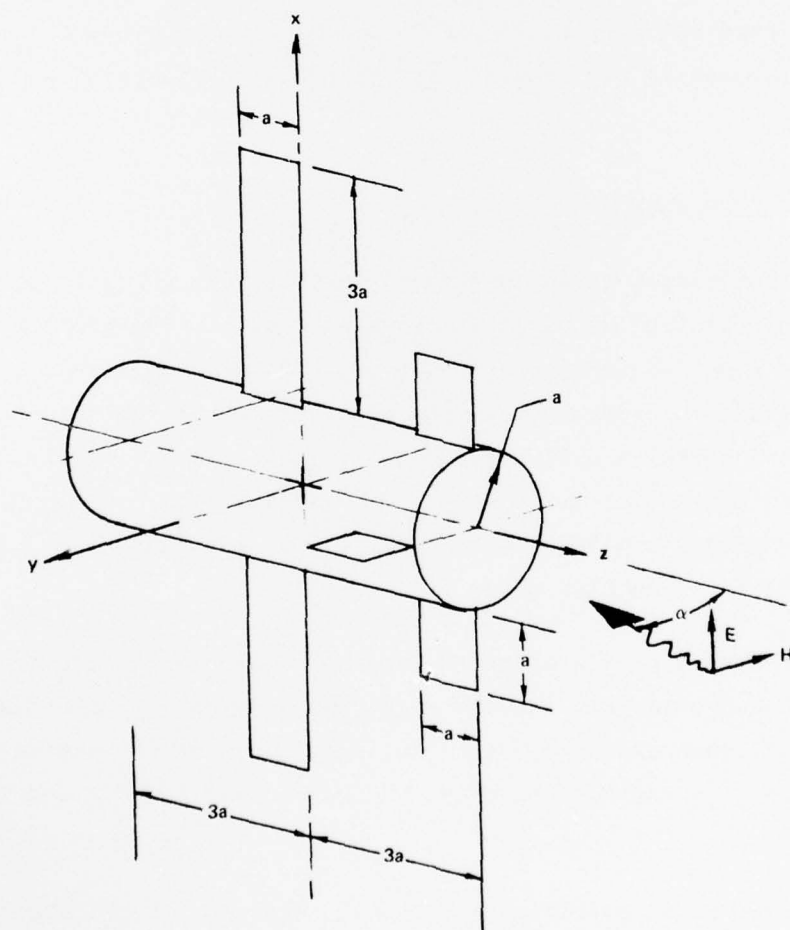


FIG. 2 Simple aircraft model.

in Fig. 2. It should be noted that most of these restrictions are not inherent to the space-time integral equation technique and could be removed at the expense of only computation time and complexity. For example, the fuselage could be any convex surface, the various fins could be flat plates with more general straight-edge contours, and the symmetry conditions could be removed to allow computation at arbitrary incidence with arbitrary polarization.

2.2 SPACE-TIME INTEGRAL EQUATION SOLUTION

The problem of determining the scattering by cylinders with fins attached is of great practical interest, since this serves as a model for numerous missiles and aircraft. To the authors' knowledge, there has been no adequate procedure developed for the solution of this complex scattering problem in either the time domain or the frequency domain. This section describes the method for solving the problem of scattering by a cylinder with multiple sets of fins. This is an extension of techniques developed earlier for cylinders with a single set of fins [5]. Basically this approach consists of developing two simultaneous space-time integrodifferential equations and their subsequent computer solution by marching on in time. These equations contain terms which may be interpreted as:

- (a) The influence of cylinder currents on other cylinder currents.
- (b) The influence of fin currents on cylinder currents.
- (c) The influence of fin currents on other fin currents.
- (d) The influence of cylinder currents on fin currents.

The neighborhood along the line where a fin is attached to the cylinder is accounted for by application of boundary conditions at the edge of the fin.

2.2.1 Derivation of Space-Time Integral Equation

The technique used here to develop the space-time integrodifferential equation for surfaces with fins attached is to consider the equivalent of this scattering problem shown in Fig. 3. In this equivalent statement of the problem, the conducting surface has been replaced by source surface

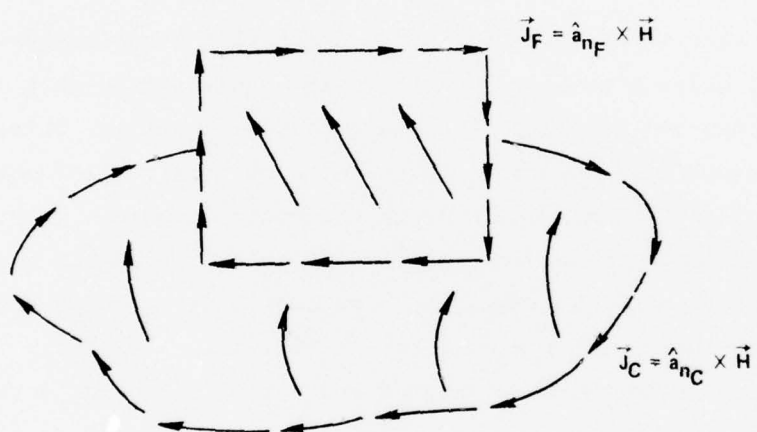


FIG. 3 Equivalent problem of scattering from surfaces with fins attached.

currents and the conducting fins have been replaced by source fin currents. Since these source currents are now radiating in free space, the techniques used for the case of scattering from surfaces alone can be combined with the techniques used for the case of scattering from flat plates alone to solve the problem of scattering from surfaces with fins attached. The integral equation for the surface currents is obtained by considering the problem in Fig. 3, in which the scatterer has been replaced by source currents \vec{J} which are equal to

$$\vec{J} = \hat{a}_n \times \vec{H}.$$

Since these currents are radiating in free space, the free-space Green's function may be used to find the expression for the total \vec{H} field at an arbitrary point in space, which is

$$\vec{H}(\vec{r}, t) = \vec{H}^i(\vec{r}, t) + \frac{1}{4\pi} \int_S \left[\frac{1}{R} + \frac{1}{Rc} \frac{\partial}{\partial \tau} \right] \vec{J}(\vec{r}', \tau) \times \hat{a}_R dS' \quad (1)$$

$$\tau = t - R/c$$

where

\vec{r} = position vector to the observation point

\vec{r}' = position vector to the integration point

$$R = |\vec{r} - \vec{r}'|$$

$$\hat{a}_R = \frac{\vec{r} - \vec{r}'}{R}$$

c = the speed of light.

An integral equation for the current density \vec{J} may be obtained by specializing the arbitrary space point \vec{r} to a point on the surface of the scatterer and then applying the boundary conditions to cast \vec{H} in terms of \vec{J} . Performing the limiting procedure and applying the boundary condition yields the integral equation

$$\vec{J}(\vec{r}, t) = 2\hat{a}_n \times \vec{H}^i(\vec{r}, t) + \frac{1}{2\pi} \int_S \hat{a}_n \times \left\{ \left[\frac{1}{R^2} + \frac{1}{Rc} \frac{\partial}{\partial \tau} \right] \vec{J}(\vec{r}', \tau) \times \hat{a}_R \right\} dS' \quad (2)$$

$\tau = t - R/c$

where \vec{r} is now located on the surface of the scatterer. Equation (2) is a space-time vector integral equation for the current density \vec{J} on the surface of the scatterer. The first term in the right-hand side of Eq. (2) may be considered the source term and represents the direct influence of the incident field on the current at the observation point (\vec{r}, t) . The integral term on the right-hand side of Eq. (2) gives the influence of currents at other surface points on the current at (\vec{r}, t) .

The factor of 2 in going from Eq. (1) in free space to Eq. (2) on the surface arises due to the following well known boundary value argument. Consider the small patch at the surface point \vec{r} . The field \vec{H} at \vec{r} is due to the effect of the patch plus the effect from the rest of the surface and the incident field. If we move \vec{r} just inside the conducting surface (where we know the field to be zero), the contribution from the patch changes sign. The magnitude of the effect of the patch is thus the same as that due to the remainder of the surface and the incident field. Taking the limit as the patch size goes to zero, we thus obtain for the field just outside the surface twice the value of Eq. (1). Performing the cross product with \hat{a}_n we then obtain Eq. (2).

The currents flowing on the surface are a function not only of the incident field but also of the currents at other cylinder surface points and fin surface points. Equation (2) can be expanded to display these two contributions explicitly and give the total space-time integral equation for the cylinder surface currents as

$$\begin{aligned} \vec{J}_C(\vec{r}, t) = & 2\hat{a}_n \times \vec{H}^i(\vec{r}, t) + \frac{1}{2\pi} \int_C \hat{a}_n \times \left\{ \left[\frac{1}{R^2} + \frac{1}{R} \frac{\partial}{\partial \tau} \right] \vec{J}_C(\vec{r}', \tau) \times \hat{a}_R \right\} dS' \quad (3) \\ & + \frac{1}{2\pi} \int_F \hat{a}_n \times \left\{ \left[\frac{1}{R^2} + \frac{1}{R} \frac{\partial}{\partial \tau} \right] \vec{J}_F(\vec{r}', \tau) \times \hat{a}_R \right\} dS'. \end{aligned}$$

$\tau = t - R$
 $\tau = t - R$

In Eq. (3) the units of time have been changed from seconds to light-meters, where one light-meter is defined as the time it takes an electromagnetic wave traveling at velocity c to travel a distance of one meter.

The integrodifferential equation for the fin currents is obtained by starting with the expression for the electric field in terms of the electric and magnetic potentials. The geometry of the problem is displayed in Fig. 2. In this particular formulation, the fins lie in the x - z and y - z planes and the incident field makes an angle α with the x - z plane. For this geometry, the total electric field is given by

$$\vec{E}(\vec{r}, t) = \vec{E}^i(\vec{r}, t) - \mu \frac{\partial \vec{A}(\vec{r}, t)}{\partial t} - \nabla \phi(\vec{r}, t) \quad (4)$$

where

\vec{A} = magnetic vector potential such that $\vec{H} = \nabla \times \vec{A}$

ϕ = electric potential

μ = permeability of space.

Next, apply to Eq. (4) the Lorentz gauge relation

$$\nabla \cdot \vec{A} + \epsilon \frac{\partial \phi}{\partial t} = 0$$

where ϵ is the permittivity of space, yielding

$$\epsilon \frac{\partial \vec{E}(\vec{r}, t)}{\partial t} = \epsilon \frac{\partial \vec{E}^i(\vec{r}, t)}{\partial t} + \nabla(\nabla \cdot \vec{A}) - \mu \epsilon \frac{\partial^2 \vec{A}(\vec{r}, t)}{\partial t^2} \quad (5)$$

Then applying the E-field boundary condition that the component of the total E-field tangent to the fin vanishes everywhere on the fin, Eq. (5) can be expressed as

$$\nabla \cdot \nabla \cdot \vec{A}(\vec{r}, t) - \frac{\partial^2 \vec{A}(\vec{r}, t)}{\partial t^2} = -\epsilon \frac{\partial \vec{E}^i(\vec{r}, t)}{\partial t} \quad (6)$$

or, in a more simplified form

$$\square^2 \vec{A} + \nabla \vec{A} = -\epsilon \frac{\partial \vec{E}^i}{\partial t} \quad (7)$$

where

$$\square^2 \vec{A} = \left(\frac{\partial^2}{\partial x^2} - \frac{\partial^2}{\partial t^2} \right) A_x \hat{a}_x + \left(\frac{\partial^2}{\partial y^2} - \frac{\partial^2}{\partial t^2} \right) A_y \hat{a}_y + \left(\frac{\partial^2}{\partial z^2} - \frac{\partial^2}{\partial t^2} \right) A_z \hat{a}_z,$$

the wave operator.

$$\nabla \vec{A} = \frac{\partial}{\partial x} \left(\frac{\partial A_y}{\partial y} + \frac{\partial A_z}{\partial z} \right) \hat{a}_x + \frac{\partial}{\partial y} \left(\frac{\partial A_z}{\partial z} + \frac{\partial A_x}{\partial x} \right) \hat{a}_y + \frac{\partial}{\partial z} \left(\frac{\partial A_x}{\partial x} + \frac{\partial A_y}{\partial y} \right) \hat{a}_z$$

$$\vec{A}(\vec{r}, t) = \frac{1}{4\pi} \int \left(\frac{\vec{J}(\vec{r}', \tau)}{R} \right) dS'.$$

$$\tau = t - R$$

In order to obtain an expression for the fin currents directly, it is necessary to express the magnetic vector potential \vec{A} as the sum of two components, one due to the observation point ("self" patch) and the other due to the remainder of the patches. If the fin grid patches are small enough, then the current over a given patch can be assumed constant. This makes it possible to express \vec{A} as

$$\vec{A}(\vec{r}, t) = \gamma \vec{J}_F(\vec{r}, t) + \frac{1}{4\pi} \int_{\text{Non-Self Patches}} \left(\frac{\vec{J}(\vec{r}', \tau)}{R} \right) dS' \quad (8)$$

$\tau = t - R$

where

$$\gamma = 2 \cdot \left(\frac{\Delta S}{\pi} - \left(\frac{\delta}{2} \right)^2 - \frac{\delta}{2} \right)$$

ΔS = area of patch containing \vec{r}

δ = thickness of fin.

Substituting Eq. (8) into Eq. (7) yields the fin currents directly

as

$$\square^2 \vec{J}_F(\vec{r}, t) + \boxtimes \vec{J}_F(\vec{r}, t) = \frac{1}{Y} \left\{ -\epsilon \frac{\partial E^i}{\partial t} - \square^2 \vec{A}_{NS}(\vec{r}, t) - \boxtimes \vec{A}_{NS}(\vec{r}, t) \right\} \quad (9)$$

where

$$\vec{A}_{NS} = \frac{1}{4\pi} \int_{\text{Non-Self Patches}} \frac{\vec{J}(\vec{r}', \tau)}{R} dS'$$

$\tau = t - R$

The surface currents contributing to \vec{A}_{NS} are both cylinder currents and fin currents. The contribution of both of these can be separated in Eq. (9) and displayed explicitly to give the expression for the current flowing on the fin

$$\square^2 \vec{J}_F(\vec{r}, t) + \boxtimes \vec{J}_F(\vec{r}, t) = \frac{1}{Y} \left\{ -\epsilon \frac{\partial E^i}{\partial t} - \square^2 \left[\vec{A}_{FNS}(\vec{r}, t) + \vec{A}_C(\vec{r}, t) \right] - \boxtimes \left[\vec{A}_{FNS}(\vec{r}, t) + \vec{A}_C(\vec{r}, t) \right] \right\} \quad (10)$$

where $\vec{A}_C(\vec{r}, t)$ is the magnetic vector potential due to the cylinder current.

The fin currents at the free-space edges and at the fin-cylinder join are given by the boundary conditions

$$\begin{aligned} \vec{J}_\perp(\vec{r}, t) &= 0, \quad \vec{J}_\parallel(\vec{r}, t) \rightarrow \infty && \text{(free-space edge)} \\ \frac{\partial \vec{J}_\perp}{\partial n}(\vec{r}, t) &= 0, \quad \vec{J}_\parallel = 0 && \text{(fin-cylinder join)} \end{aligned} \quad (11)$$

where

$$\begin{aligned} \vec{J}_\perp(\vec{r}, t) &= \text{current component perpendicular to the edge or join} \\ \vec{J}_\parallel(\vec{r}, t) &= \text{current component parallel to the edge or join.} \end{aligned}$$

Thus, the space-time integral equations (3) and (10) together with the boundary conditions in Eq. (11) form the solution for the surface currents on a cylinder with fins attached.

In most applications, the quantity of interest is the far-scattered field. This can be computed directly from the surface currents. The far-field expression for the scattered magnetic field, \vec{H}^s , may be obtained from Eq. (1) by noting that the contribution of the first term within the integral becomes negligible when R becomes very large. In addition,

$$\hat{a}_R \rightarrow \hat{a}_r$$

and

$$\frac{1}{R} \rightarrow \frac{1}{r}$$

Thus, the expression for the far field, with time expressed in light-meters, becomes

$$\vec{r} \vec{H}^s(\vec{r}, t) = \frac{1}{4\pi} \int_S \frac{\partial \vec{J}(\vec{r}', \tau)}{\partial \tau} \times \hat{a}_r \, dS'. \quad (12)$$

$$\tau = t - R$$

2.3 NUMERICAL SOLUTION

To obtain a solution of the space-time integral equations for a cylinder with fins attached, each of the components of the problem must be represented mathematically. First, the geometry of the scatterer and the characteristics of the incident field must be numerically specified. From these, the surface and fin currents can be computed using numerical representations of Eqs. (3) and (10). This is accomplished by carrying out the integration and differentiation numerically and using a "marching on in time" procedure. The far-scattered field can be computed directly from the current densities by using a numerical representation of Eq. (12).

To describe the scatterer geometrically, the scattering surface is divided into curvilinear patches of approximately equal area with a space sample point at the center of each patch. The spacing of these sample points (and thus, the size of the patches) is chosen small enough to give both a good representation of the scatterer itself and of the currents that exist on the scatterer. The sample point spacing affects the time increment Δt at which the current densities can be calculated. The time increment must not exceed the time it takes a wave, moving at the speed of light, to travel between the closest space points. This insures that the integral equation can be expressed as a recurrence relation in time and that a matrix inversion is not necessary to obtain a solution.

The space-time integral equations (3) and (10) represent, in principle, the solution of the scattering problem for cylinders with fins attached for an arbitrary incident field. Although the equations can be solved for each incident field separately, it is very inefficient to do so. Since in most practical scattering problems the excitation is a plane wave, a more efficient way to approach this problem is to compute the scattered response when the incident wave is an electromagnetic impulse. Once the impulse response of a target has been obtained, the response due to any incident plane wave, whose spectrum is contained within the spectrum of an impulse, can be calculated by a simple convolution procedure. Moreover, the impulse response is intimately related to the actual geometry of the target, and thus, the potential for developing techniques to determine the impulse response of a scatterer by an inspection of its geometry is ever present.

For the numerical solution, however, it is not practical to use an ideal impulse for an excitation. Thus, in this solution a regularized or smoothed impulse is used. The form of this illumination at the origin is the Gaussian regularization of an impulse, namely

$$H^i(t) = \frac{n}{\sqrt{\pi}} e^{-n^2 t^2} \quad (13)$$

which converges to a delta functional as n goes to infinity. The time domain integral equations can be solved exactly for bodies with linear

dimensions up to several pulse widths of this regularized impulse. In this solution consideration is limited to bodies of this size.

The currents flowing on the cylinder and on the fin are computed using numerical representations of Eqs. (3) and (10). For the purpose of discussing the numerical solution, only the x-components of these equations will be considered. Similar representations are used for the calculation of the other components.

For the numerical solution, Eq. (3) for the x-component of the cylinder current at sample point i and time t is represented as

$$J_{Cx}(r_i, t) = \frac{1}{\gamma_i} \left[2 n_{yi} H_z^i - n_{zi} H_y^i \right] + \frac{1}{2\pi} \sum_{\ell=1}^N F(J_x) n_{yi} \frac{n_{Ry}}{R} + n_{zi} \frac{n_{Rz}}{R} - F(J_y) n_{yi} \frac{n_{Rx}}{R} - F(J_z) n_{zi} \frac{n_{Rx}}{R} \Delta S_\ell \quad (14)$$

where

γ_i = self-term correction factor for observation patch i

(H_y^i, H_z^i) = the y- and z-components of the incident field at patch i, time t

N = number of grid patches on the cylinder and fin

$F(J) = J(r_\ell, \tau)/R + \partial J(r_\ell, \tau)/\partial \tau$

$J_x(r_\ell, \tau)$ = the x-component of the current density at patch ℓ , time τ

$\tau = t - R$

t = time in light-meters

R = distance from the integration patch ℓ to the observation patch i: $R = \sqrt{(x_i - x_\ell)^2 + (y_i - y_\ell)^2 + (z_i - z_\ell)^2}$

a_{ni} = unit normal at patch i, (n_{xi}, n_{yi}, n_{zi})

\hat{a}_R = unit vector from patch ℓ to patch i , (n_{Rx}, n_{Ry}, n_{Rz})

$$n_{Rx} = \frac{x_i - x_\ell}{R}$$

$$n_{Ry} = \frac{y_i - y_\ell}{R}$$

$$n_{Rz} = \frac{z_i - z_\ell}{R}$$

ΔS_ℓ = area of patch ℓ .

The time differentiation and interpolation necessary for the evaluation of the integrands appearing in Eq. (3) are performed numerically by representing the surface current with a fourth-order polynomial. In order to achieve the best accuracy, the five points used for the representation are chosen such that the current is evaluated as near as possible to the middle of them.

The numerical representation of Eq. (10) for the x-component of the fin current at (r_i, t) is obtained by representing the second time derivative of the fin current by a three-point difference approximation, yielding

$$J_{Fx}(r_i, t) \approx 2J_{Fx}(r_i, t - \Delta t) - J_{Fx}(r_i, t - 2\Delta t) + \frac{\Delta t^2}{\gamma_i} \left(\epsilon \frac{\partial E_x^i(r_i, t - \Delta t)}{\partial t} + \frac{\partial^2 A_x}{\partial x^2} + \frac{\partial^2 A_z}{\partial x \partial z} + \frac{\partial^2 A_y}{\partial x \partial y} - \frac{\partial^2 A_{xNS}}{\partial t^2} \right) \quad (15)$$

where

Δt = solution time step

$$A_x = \gamma_i J_{Fx}(r_i, t - \Delta t) + A_{xNS}$$

$$A_{x_{NS}} = \sum_{\substack{\ell=1 \\ \ell \neq i}}^N \frac{J_x(r_\ell, \tau)}{R} \Delta S_\ell$$

$$\tau = t - \Delta t - R.$$

The space and time derivatives in Eq. (15) are evaluated using three- and five-point difference approximations. For the time interpolation a linear approximation is used.

The equations for the surface and fin currents are solved with a digital computer by simply marching on in time. The computation starts at a point in time before the incident field reaches the scatterer and proceeds sequentially in time in the same manner that nature would solve the problem in the real world. It is important to note that since the minimum spacing between space sample points on the surface is not less than Δt , then Eqs. (14) and (15) give the current density in terms of other currents at times not later than $(t - \Delta t)$ which are already known. Thus, the integral Eqs. (3) and (10) have been reduced to recurrence formulas in time and the need to perform matrix inversions has been eliminated.

Once the current densities have been computed, the far-scattered field can be calculated directly using a numerical representation of Eq. (12). For computation purposes, Eq. (12) is expanded in rectangular coordinates yielding

$$H_x^S(r, t) = \frac{1}{4\pi r} \sum_{\ell=1}^N \left[\frac{\partial J_y(r_\ell, \tau)}{\partial \tau} n_{rz} - \frac{\partial J_z(r_\ell, \tau)}{\partial \tau} n_{ry} \right] \Delta S_\ell \quad (16)$$

$$H_y^S(r, t) = \frac{1}{4\pi r} \sum_{\ell=1}^N \left[\frac{\partial J_z(r_\ell, \tau)}{\partial \tau} n_{rx} - \frac{\partial J_x(r_\ell, \tau)}{\partial \tau} n_{rz} \right] \Delta S_\ell \quad (17)$$

$$H_z^S(r, t) = \frac{1}{4\pi r} \sum_{\ell=1}^N \left[\frac{\partial J_x(r_\ell, \tau)}{\partial \tau} n_{ry} - \frac{\partial J_y(r_\ell, \tau)}{\partial \tau} n_{rx} \right] \Delta S_\ell \quad (18)$$

where

$$\vec{H}^S = H_x^S \hat{a}_x + H_y^S \hat{a}_y + H_z^S \hat{a}_z$$

$$\hat{a}_r = n_{rx} \hat{a}_x + n_{ry} \hat{a}_y + n_{rz} \hat{a}_z .$$

The time differentiation and interpolation necessary for the evaluation of $\partial J(r, \tau) / \partial \tau$ are performed numerically using a five-point Lagrange interpolation formula.

A sketch of the geometry parameters used for the description of the far-scattered field is drawn in Fig. 4. In this sketch the incident field is shown propagating in the yz-plane and making an angle α with the z-axis. The scattered fields produced by the surface currents are then computed in the two principal planes. The scattered field is computed in the yz-plane at angles ψ_{yz} with respect to the direction of propagation of the incident wave. In this plane the two orthogonal components used to represent the scattered field are the component perpendicular to the yz-plane, H_{yzx}^S , and the component tangent to the yz-plane, H_{yzt}^S . The other plane in which the scattered field is computed is the px-plane, which is formed by the direction of propagation of the incident wave and the x-axis. In this plane the two components used to represent the scattered field are the component perpendicular to the px-plane, H_{pxp}^S , and the component tangent to the px-plane, H_{pxt}^S . These scattered fields are computed at angles ψ_{px} , which are measured with respect to the direction of propagation of the incident wave.

2.4 TIME DOMAIN MEASUREMENTS

The computer program incorporating the methods described in the preceding section was verified by comparing the calculated time domain smoothed impulse response with measurements made on the Sperry Research Center time domain scattering range. This patented measurement system [7], which has been described in detail [5,8,9], is reviewed in Sec. 2.4.1 and the calculated and measured results are compared in Sec. 2.4.2.

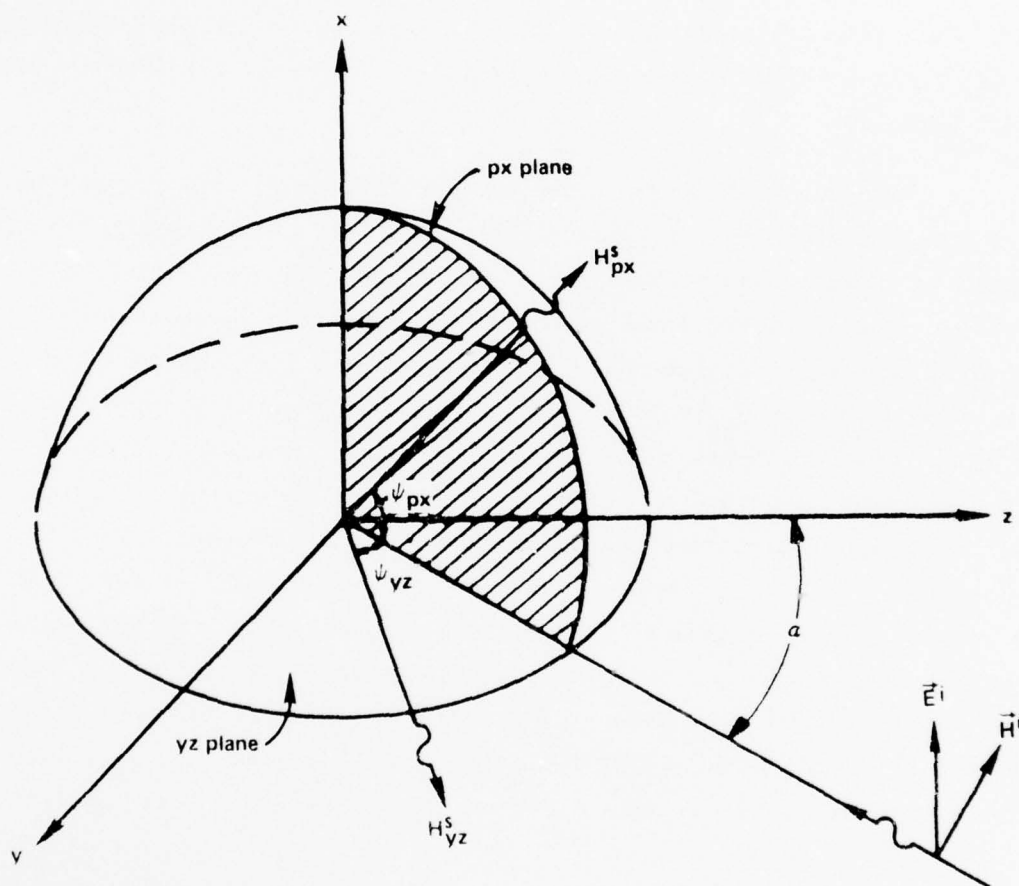


FIG. 4 Geometry of far scattered field.

2.4.1 Time Domain Measurement System

The time domain scattering range is a system for obtaining a low-noise response in the nanosecond region. It consists of a ground plane scattering range, a step function source, a sampling oscilloscope receiver, and a laboratory instrumentation computer for control and processing. The system signal source is a high-voltage switch which generates a 300 V step function with a risetime less than 100 ps. The signal is radiated, virtually undistorted, from a wire transmitting antenna protruding through a circular ground plane 20 feet in diameter. This wave illuminates the target and the resulting scattered waveform is received on a coaxial horn antenna, which essentially smoothes and differentiates the signal and thus provides the smoothed impulse response of the target. The received waveform is sampled by a 12 GHz oscilloscope that has been triggered by the initial pulse and whose sampling gate deflection is under the control of a small instrumentation computer. Unprocessed data are displayed on the oscilloscope CRT while the sampled-and-held waveform is passed through a low-pass filter, digitized, read into the computer, and stored on magnetic tape automatically. This system has been designed to correct the long-term timing drift and/or amplifier drift. In addition, the waveforms are stored in such a way that they are ready for the subsequent operations of averaging (to remove short-term noise) and baseline processing. The effects of a time varying baseline are subtracted from measured waveforms to improve system accuracy.

The salient characteristics of the range are the speed and simplicity with which multi-octave frequency-domain data can be obtained. These advantages accrue because the time-domain scattering range yields an "uncontaminated" interval of time between the arrival of the direct wave and the arrival of unwanted reflections. Targets are usually located anywhere from two to five feet from the transmitting antenna. The response from the antenna tip and the table edge occur at approximately 15 ns. Thus, a "clean window" exists between 4 ns and 15 ns which can be used to view the target responses. The entire region between the direct transmission and the table edge response forms a convenient time "window" to view the target response and allows one to "gate out" (in time) unwanted reflections. Thus, undis-

torted transient target responses can be viewed without resorting to elaborate and expensive anechoic chambers. In addition, a single time-domain measurement obviates the requirement for tedious measurement of the amplitude and phase responses at many frequencies.

The accuracy of the measurement system has been estimated for the results presented in this section. The peak of the incident pulse as measured on the sampling oscilloscope is approximately 400 mV, and a typical target response has a peak value in the vicinity of 10 mV. When using the 10 mV scale on the sampling oscilloscope, the standard deviation of the sample mean is estimated to be

$$\sigma_{\bar{v}} = 0.5 \text{ mV}$$

if 16 scans are averaged. Thus, the estimated standard deviation of the sample mean \bar{v} is in the vicinity of 5% of the peak value of the target response.

The signal received directly from the source is also measured. Taking the distances between source, receiver and target into account, the frequency response of the target is obtained by numerically deconvolving the source signal from the response. The source is not exactly the Gaussian smoothed impulse used for the calculated response (Eq. 13). Therefore, a convolution procedure is carried out on the measured response to permit comparison with the calculated response in the time domain. The width of the smoothed impulse is chosen to be slightly greater than the width of the source signal. This has the effect of reducing high frequency noise in the response. Taking the smoothed impulse width greater yet, i.e. reducing the higher frequency contents of the incident pulse, smoothes the response further at the expense of a reduction in the fast structure of the response. In these measurements the incident pulse width was about 0.59 ns or 7". The comparisons were made at smoothed impulse widths of 8" and 16". The target lengths were 8" and 12".

2.4.2 Comparison of Measured and Calculated Responses

The targets chosen for comparison were 8" long and 12" long right circular cylinders, each of radius 2", and each with a set of 4" square fins at the ends, as illustrated in Fig. 5.

In Fig. 6 the responses of these two targets are shown at broadside incidence ($\alpha = 90^\circ$) for $an = 1$. The target radius a is 2" and the nominal pulse width is defined as $4/n = 8"$. The time scale is t/a (t is in light-meters) and the response has been normalized to $r_0 H/a$. (See ref. 4 for a discussion on scaling and normalization.) The solid curve represents the calculated response, the dotted curve the convolved measured response.

While the agreement is remarkably close, it is interesting to observe the deviations (of less than 10% of peak value) in the rapidly fluctuating peaks of the signals. These disagreements are greatly reduced when the comparison is made at $an = 0.5$ (corresponding to a pulse width of 16") as is done in Fig. 7 for these same targets. Inaccuracies thus begin to appear at shorter wavelengths. It is believed that these inaccuracies are almost entirely due to the relatively coarse patch structure of the numerical representation of the target used in the response calculations. On the basis of experience with space-time integral equation calculations on other targets with edges, it is known that even greater accuracy can be obtained by more detailed structuring of the target representation, in particular, near the fin edges.

As an additional comparison, the results are given in Fig. 8 for the same targets viewed tail-on ($\alpha = 0$) with $an = 0.5$.

2.5 CALCULATED RESPONSE OF AIRCRAFT MODEL

The model chosen for these calculations is shown in Fig. 2. The calculated responses are plotted in Figs. 9 and 10 for aspect angles from 0° to 180° at 30° intervals.

It is instructive to note the composition of the response. Consid-

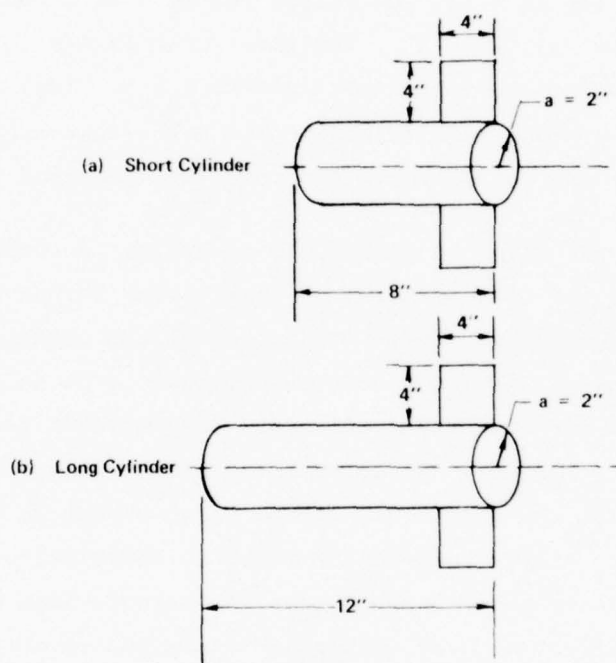
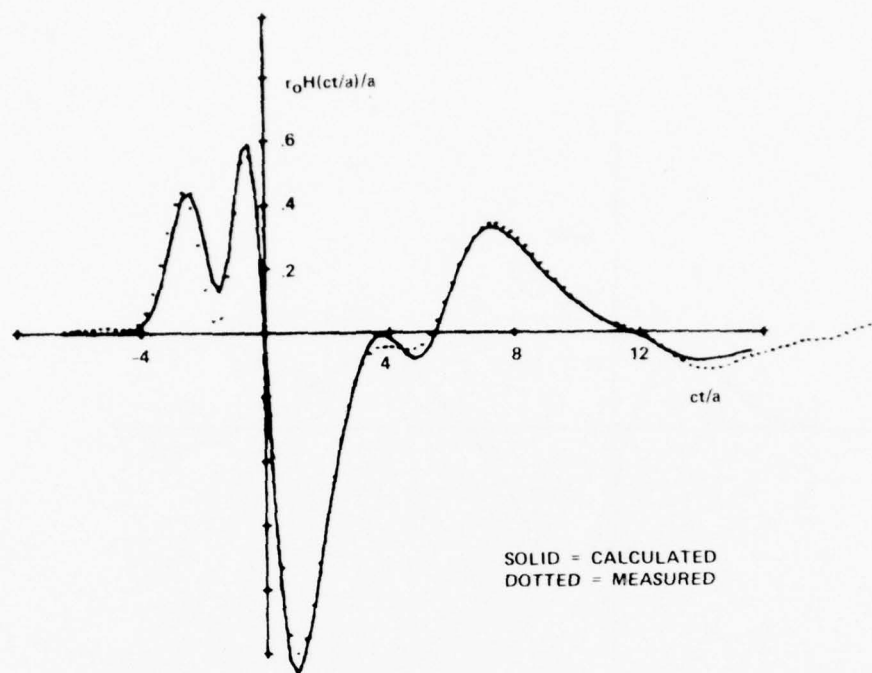
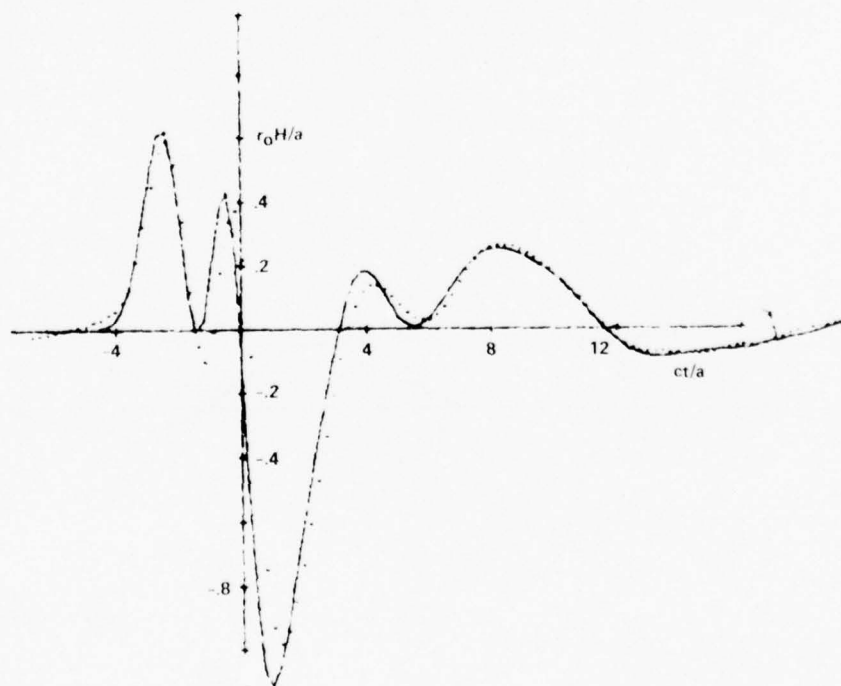


FIG. 5 Targets used for comparison of calculated and measured responses.

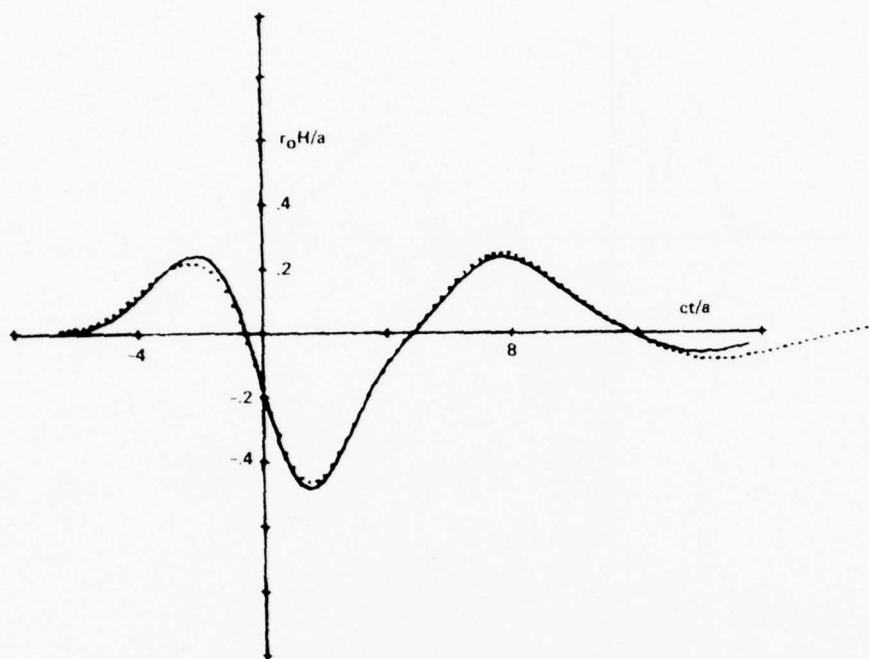


(a) Short Cylinder

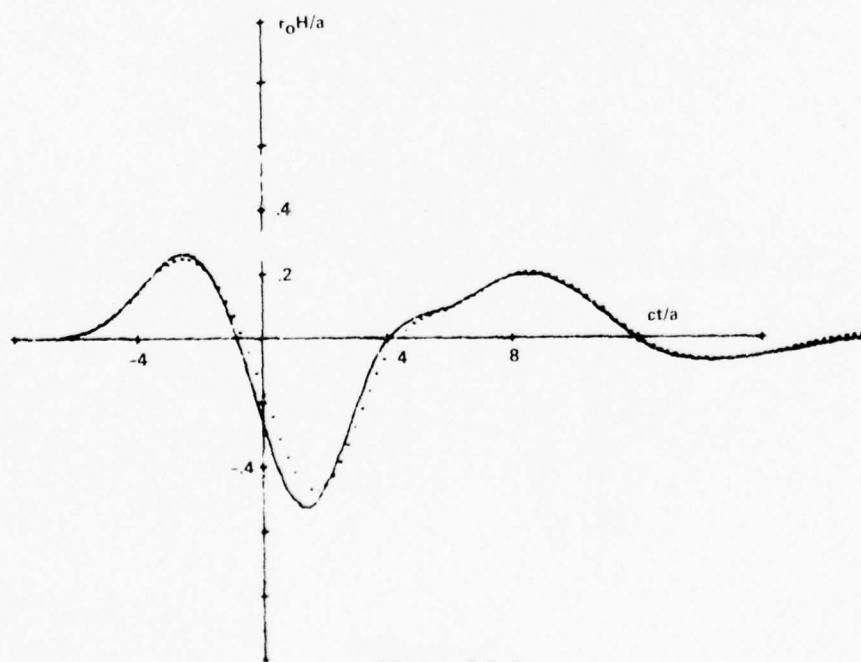


(b) Long Cylinder

FIG. 6 Comparison of calculated and measured responses, $an = 1$, $\alpha = 90^\circ$.



(a) Short Cylinder



(b) Long Cylinder

FIG. 7 Comparison of calculated and measured responses, $\alpha n = 0.5$, $\alpha = 90^\circ$.

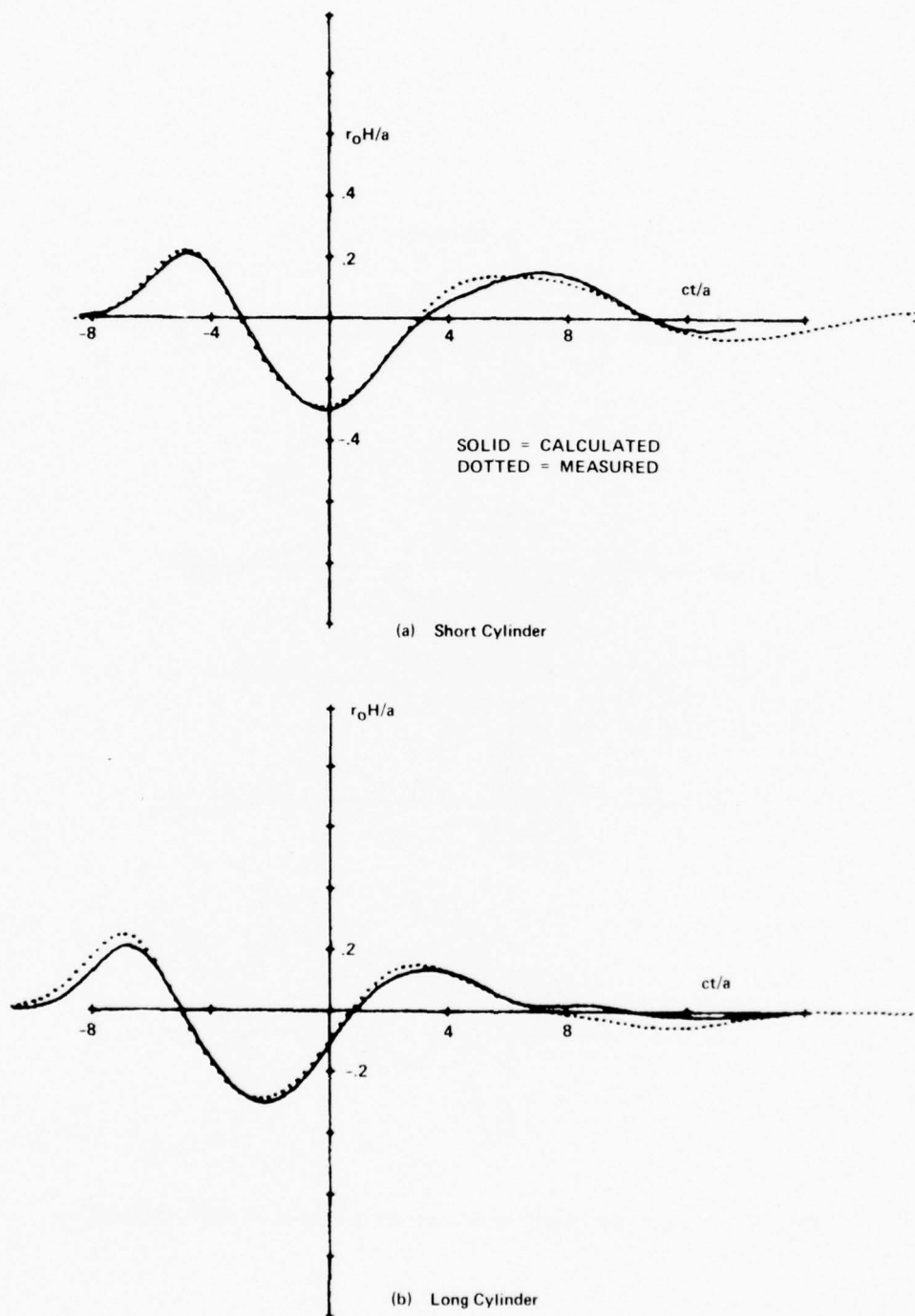


FIG. 8 Comparison of calculated and measured responses, $\alpha = 0$, $an = 0.5$.

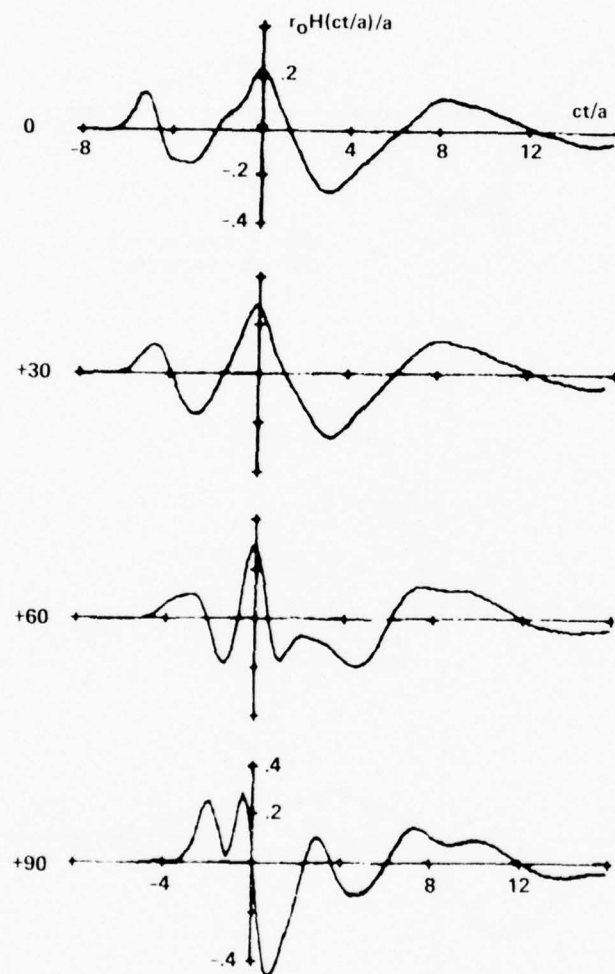


FIG. 9 Calculated response of aircraft model at 0°, 30°, 60°, 90°.

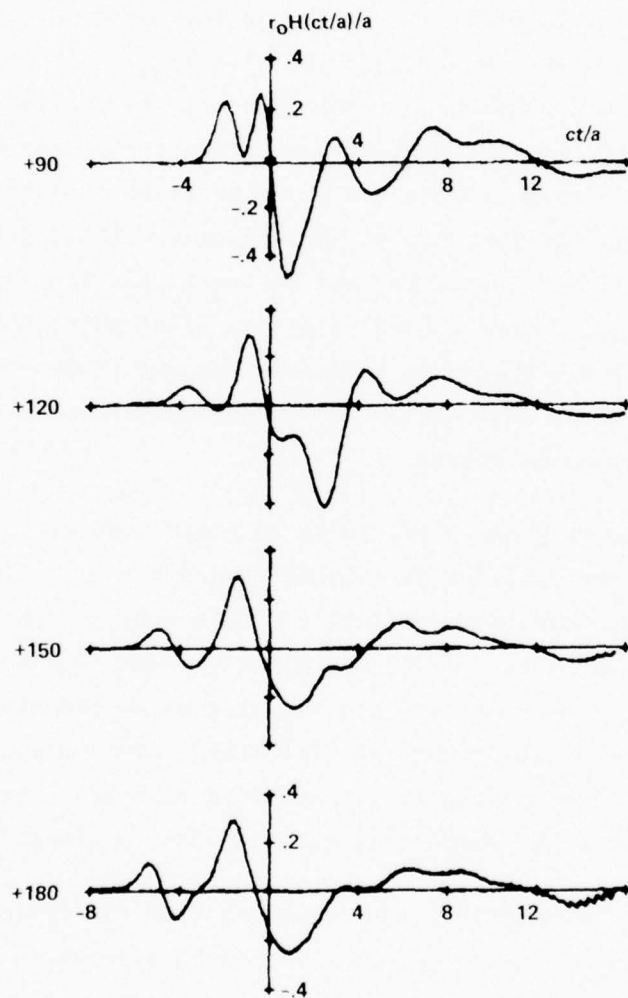


FIG. 10 Calculated response of aircraft model at 90° , 120° , 150° , and 180° .

er the tail-on aspect ($\alpha = 0^\circ$): The initial positive swing is due to the return from the cylinder face and the leading edges of the small fins. The negative swing at $t = -4$ is due both to the differentiating effect of the cylinder face and the trailing edge of the small fins. A creeping wave effect due to small fin currents interactions via the cylinder surface can be seen near $t = -1.5$ just before the large positive peak from the leading edges of the large fins at $t = 0$. This is followed by a large negative swing from the large fin far edges and fin-fin creeping wave interactions at $t = 8$. The creeping wave effects continue after that, damping out near $t = 16$. In Fig. 11 these effects are illustrated in more detail. Shown are the responses of the same target at 0° aspect without fins and with each set of fins separately. For comparison purposes, the time scale (in light-meters) of the graph and the sketch of the incident pulse and the space scale of the target are the same; similarly the amplitude of incident and response pulses are the same scale. The behavior described above is very evident in this series of graphs.

Returning to Figs. 9 and 10 it is noted that as the aspect changes, the response from the cylinder face moves toward $t = 0$; while the response from the small fins moves more rapidly toward $t = 0$, joining that of the large fins at $\alpha = 90^\circ$. At $\alpha = 90^\circ$ the positive peak (due to the fins) near $t = 0$ is strong enough to obscure the negative swing expected at that time from a broadside response of the cylinder alone. The negative swings of cylinder body, small and large fins combine in the large response near $t = +1$. After $t = 2$ the response is entirely due to creeping waves.

At angles beyond 90° , the responses from the cylinder face and the large fins become evident before $t = 0$ as they separate with increasing α , while the response from the small fins shows as a small perturbation at times increasingly later than $t = 0$.

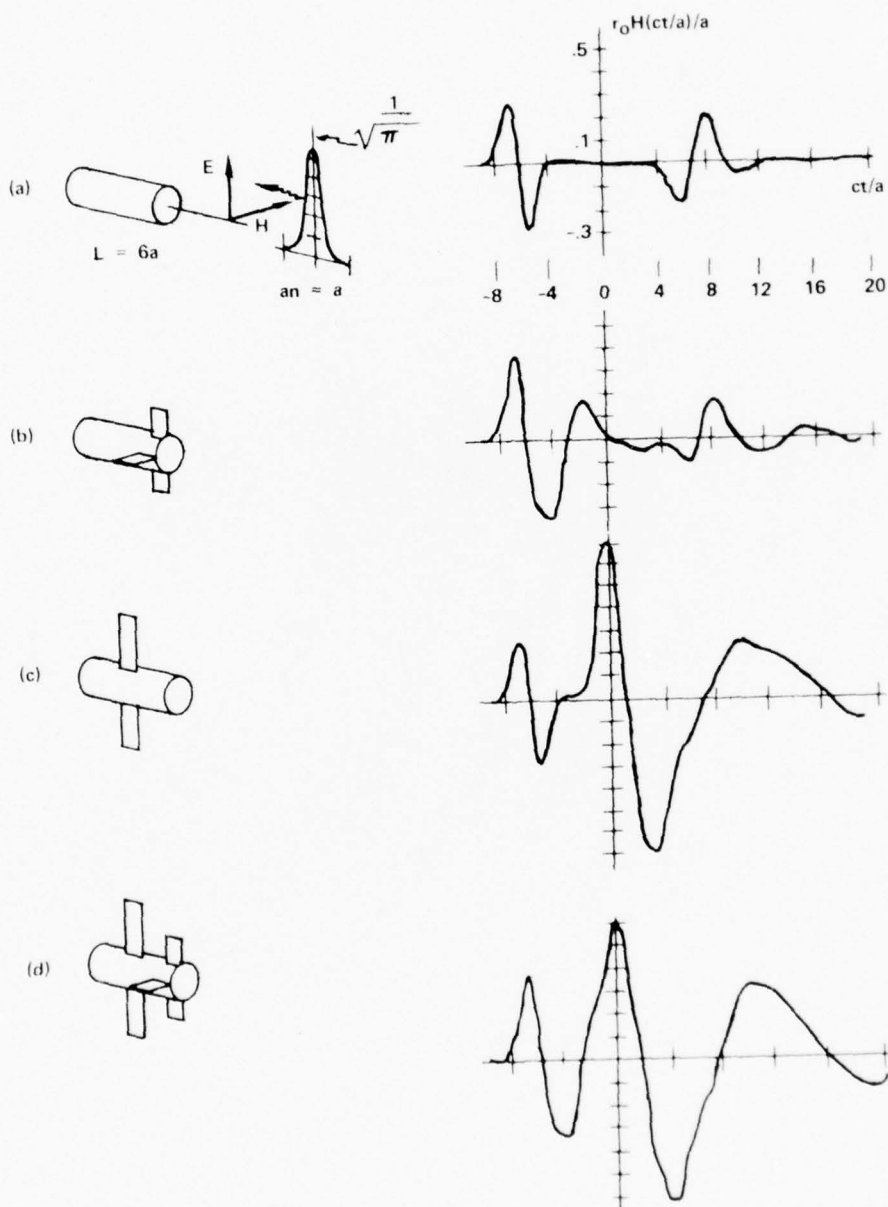


FIG. 11 Comparison of responses of several finned cylinders at axial incidence.

SECTION 3

EXTENSION OF IMPULSE RESPONSE AUGMENTATION TECHNIQUE

The space-time integral equation approach solves the scattering problem directly in the time domain. This approach is valid for any excitation; however, the most useful excitation has been found to be the regularized (or smoothed) impulse given in Eq. (13). The response due to this excitation, $r_o H^S(t_f/a)$, is the regularized (or smoothed) impulse response of the target and is computed exactly with the space-time integral equation using the techniques described in Sec. 2.2. This approach yields results for targets with sizes up to several pulse widths or, equivalently in the frequency domain, several wavelengths.

A technique has been developed which uses the space-time integral equation approach as the basis and extends the results to obtain the impulse response and frequency response of an arbitrary target over the entire spectrum [4]. This technique has been demonstrated for several smooth convex targets including the sphere, the prolate spheroid, and the sphere-capped cylinder. It has also been applied to targets with edges including right circular cylinders, flat-end sphere-cap cylinders at axial incidence and square flat plates [4,5]. The purpose of the sections which follow is to describe the extension of the impulse response augmentation technique. Sec. 3.1 provides a review of the impulse response augmentation technique. The extension to cylinders with fins attached at arbitrary incidence is described in Sec. 3.2.

3.1 REVIEW OF THE IMPULSE RESPONSE AUGMENTATION TECHNIQUE

In order to simplify the notation in these sections the electromagnetic field variables are equated to their linear system counterparts as follows:

$$H^i(t/a) \rightarrow e(t) = \text{incidence pulse}$$

$r_0 H^S(t_f/a) \rightarrow r(t)$ = smoothed impulse response

$h(t)$ = impulse response

$t/a \rightarrow t$ = time

$H^i(ka)/a \rightarrow E(\omega)$ = transform of $e(t)$

$r_0 H^S(ka)/a \rightarrow R(\omega)$ = transform of $r(t)$

$H(\omega)$ = frequency response

$ka \rightarrow \omega$ = frequency

where

H^i = incident magnetic field intensity

H^S = far scattered magnetic field intensity

r_0 = distance of far field observer from origin

t/a = normalized time

ka = normalized frequency

a = characteristic linear dimension of target.

The scaling and normalization that is indicated above yields curves which are independent of target size.

The impulse response augmentation technique, first suggested in 1968 [2] and first demonstrated for smooth convex targets in 1973 [4], and for targets with edges in 1974 [5], deals directly with the smoothed impulse response of the targets in the far field. The smoothed impulse response is computed using a space-time integral equation approach and has yielded good results up to body sizes of several pulse widths or, equivalently, up to body sizes of several wavelengths. The regions of slow variation in the smoothed impulse response remain the same in the exact impulse response; thus it is only necessary to determine the structure of the singular regions and any other regions of fast variation. But the singular portions of the

exact impulse response that result from scattering by specular points on smooth convex targets can be computed exactly, and hence, do not need to be computed by solving the space-time integral equation. The impulse response augmentation technique combines the smoothed impulse response, the known singular contribution to the impulse response, and the theory of Fourier transforms to produce the total impulse response and the frequency response (system function) of the target at all frequencies.

The impulse response augmentation technique is most easily understood by considering the most basic approach to the deconvolution (or system identification) problem. A linear system (in this case electromagnetic scattering by a target) is characterized by its impulse response $h(t)$ or, equivalently, its system function (or frequency response) $H(\omega)$. Of course,

$$h(t) \leftrightarrow H(\omega)$$

where \leftrightarrow denotes Fourier transform. The excitation $e(t)$ of the linear system in this case is the regularized (or smoothed) impulse

$$e(t) = \frac{n}{\sqrt{\pi}} e^{-(nt)^2} \quad (19)$$

which produces the regularized (or smoothed) impulse response $r(t)$ of the system. This response is given by

$$r(t) = e(t) * h(t) \quad (20)$$

where $*$ represents a convolution. In the problem being considered here, $e(t)$ is specified analytically and $r(t)$ is computed by solving the space-time integral equation. It is desired to find $h(t)$ and/or $H(\omega)$. This is the system identification or deconvolution problem.

One way to solve this problem, at least in principle, is to transform Eq. (20) and rearrange to obtain

$$\begin{aligned} H(\omega) &= \frac{R(\omega)}{E(\omega)} \\ h(t) &= F^{-1} \{ H(\omega) \} \end{aligned} \quad (21)$$

where

$$E(\omega) \leftrightarrow e(t)$$

$$R(\omega) \leftrightarrow r(t)$$

$F^{-1}\{H(\omega)\}$ is the inverse Fourier transform of $H(\omega)$.

However, the estimate of the system response $\hat{r}(t)$ that is computed contains some uncertainty or noise, and thus, the transform of the computed smoothed impulse response $\hat{R}(\omega)$ also contains some noise. In using Eq. (21) to compute the estimate of the system function, it can be shown that this noise grows exponentially [4], and therefore, this brute force technique will not yield valid large body results.

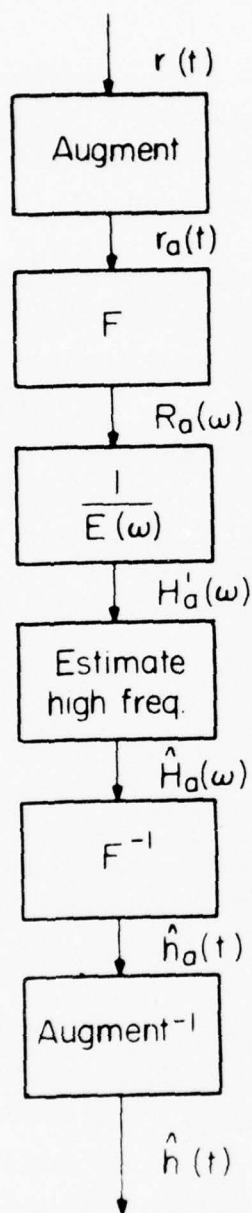
The impulse response augmentation technique is displayed in block diagram form in Fig. 12. This technique first augments the smoothed impulse response to remove the contribution from singular portions of the impulse response that are known exactly. This produces the augmented smoothed impulse response $r_a(t)$ that is given by

$$r_a(t) = r(t) - e(t) * f_a(t) \quad (22)$$

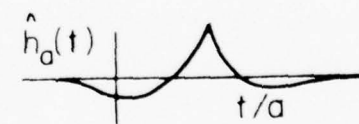
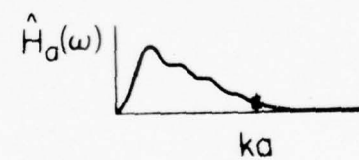
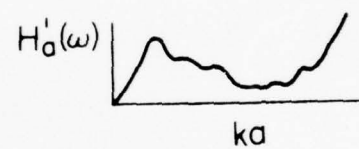
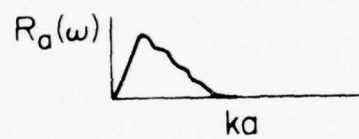
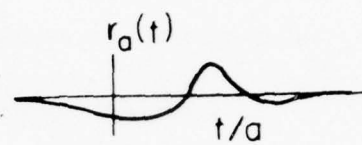
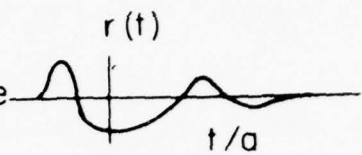
where $f_a(t)$ is a suitable augmentation function that contains the known singular portions of the impulse response.

Next, the transform of the augmented smoothed impulse response, $R_a(\omega)$, is computed and divided by the transform of the incident pulse to yield the augmented frequency response, $\hat{H}_a(\omega)$. This function contains noise which increases exponentially at frequencies above some value. However, it is known that the augmented frequency response must go to zero with increasing frequency. Thus, an estimate of the high frequency behavior of the augmented frequency response, $\hat{H}_a(\omega)$, is of the form

$$\hat{H}_a(\omega) = \begin{cases} \hat{H}_a(\omega) & ; \omega \leq \omega_c \\ F(\omega) & ; \omega \geq \omega_c \end{cases} \quad (23)$$



Smoothed
impulse response



Impulse response

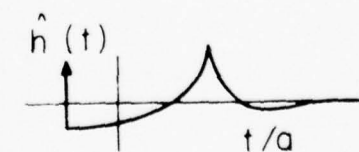


FIG. 12 Impulse response augmentation technique.

where ω_c is the boundary point and $F(\omega)$ is the high frequency estimate of $H_a(\omega)$. The inverse Fourier transform of $\hat{H}_a(\omega)$ then yields the estimate of the augmented impulse response, $\hat{h}_a(t)$.

Finally, the inverse of the augmentation procedure is performed on $\hat{h}_a(t)$, which yields the estimate of the impulse response, $\hat{h}(t)$. Moreover, an estimate of the system function, $\hat{H}(\omega)$, is obtained by applying the inverse of the augmentation procedure in the frequency domain to $\hat{H}_a(\omega)$.

The augmentation function represents the contributions of the singular portions of the impulse response which are known exactly. These singular portions may contribute to not only the high frequency behavior but also to the low frequency behavior of the response, as in the case of an impulse. These contributions are removed by subtracting the effect of the augmentation function $f_a(t)$ from the response to yield the augmented response as given in Eq. (22), which is repeated here for convenience:

$$r_a(t) = r(t) - e(t) * f_a(t) \quad (22)$$

or

$$h_a(t) = h(t) - f_a(t).$$

Since the effect of the high frequency contributions has been removed, then it remains to estimate the manner in which the lower frequency components approach zero with increasing frequency.

It has been found in previous work [4-6] that the augmentation functions should be chosen such that they account for the singular contributions to the impulse response but at the same time possess a transform that contains only linear phase variations. The functions which satisfy this simple criterion are singularity functionals and pseudo-functions that contain only a single discontinuity. Some functionals which possess this characteristic are the doublet, the impulse, the step, and Hadamard's pseudo-functions [10]. It has also been found for smooth convex targets that the singular portion of the impulse response at the leading edge region

would be given by the physical optics approximation for aspect angles where the response was polarization independent, such as axial incidence on rotationally symmetric targets. For the case of smooth convex targets with a polarization dependent response, the first order physical optics correction will yield the proper singular portion of the impulse response at the leading edge. For the case of targets with edges the singular returns from the edge regions of these targets is obtained by use of the results obtained from geometric theory of diffraction.

3.2 APPLICATION TO CYLINDER WITH FINS

In this section the impulse response augmentation technique is applied to the case of a cylinder with fins attached. This work extends the techniques that were developed on a previous effort [6] for the case of axial incidence to the case of oblique incidence. The approach used in this work is to combine the two techniques previously developed for open thin surfaces and for right circular cylinders to obtain the impulse response of a cylinder with fins attached.

The smoothed impulse response of this target was obtained using the space-time integral equation solution technique described in Sec. 2.2. The target is centered at the origin with the axis of the cylinder coincident with the z-axis as shown in Fig. 13. The cylinder has a length to diameter ratio of 2:1. Four square fins with a width of one cylinder diameter are placed symmetrically around the cylinder body. The target is illuminated by an incident plane wave with an incident pulse width equal to the length of the cylinder. The smoothed impulse response of this target was calculated for seven angles of incidence that range from 0° to 180° in 30° increments [5]. The results which have been shown to be in good agreement with measurements are displayed in Fig. 14 for 0° to 90° and in Fig. 15 for 90° to 180° .

The impulse response augmentation technique next requires a suitable augmentation function as discussed in Sec. 3.1. For the cylinder with fins the augmentation function will be taken as the sum of the augmentation

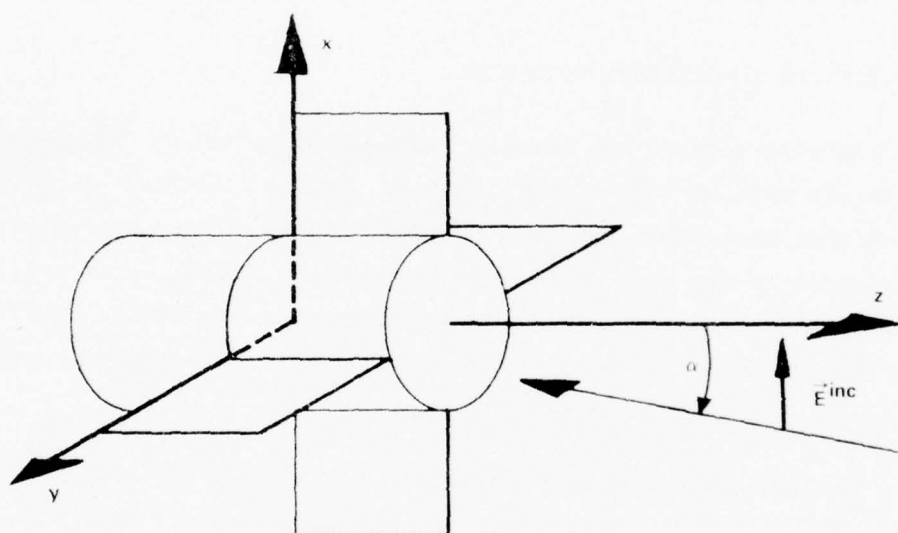


FIG. 13 Geometry of cylinder with fin.

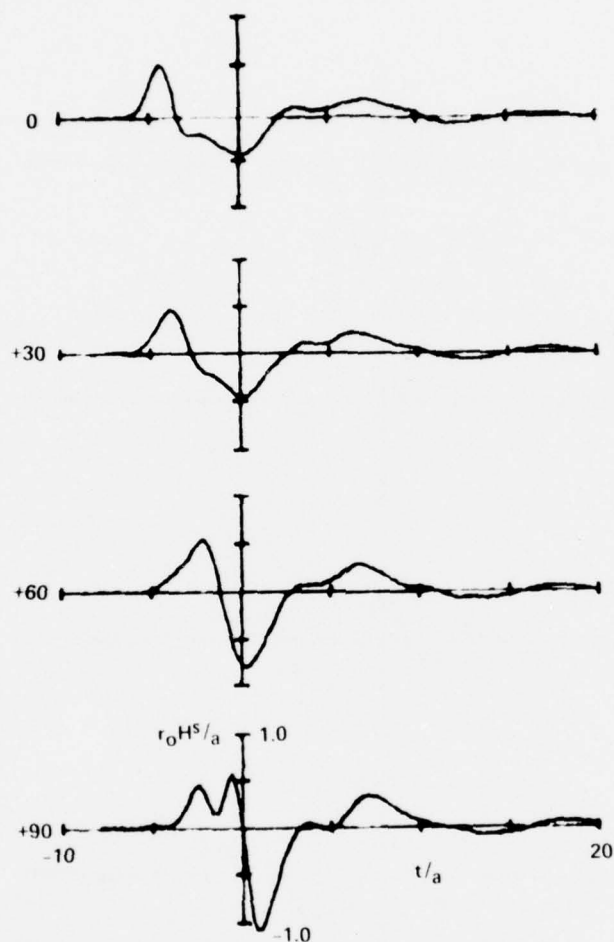


FIG. 14 Smoothed impulse response of finned cylinder at various angles of incidence for TE polarization.

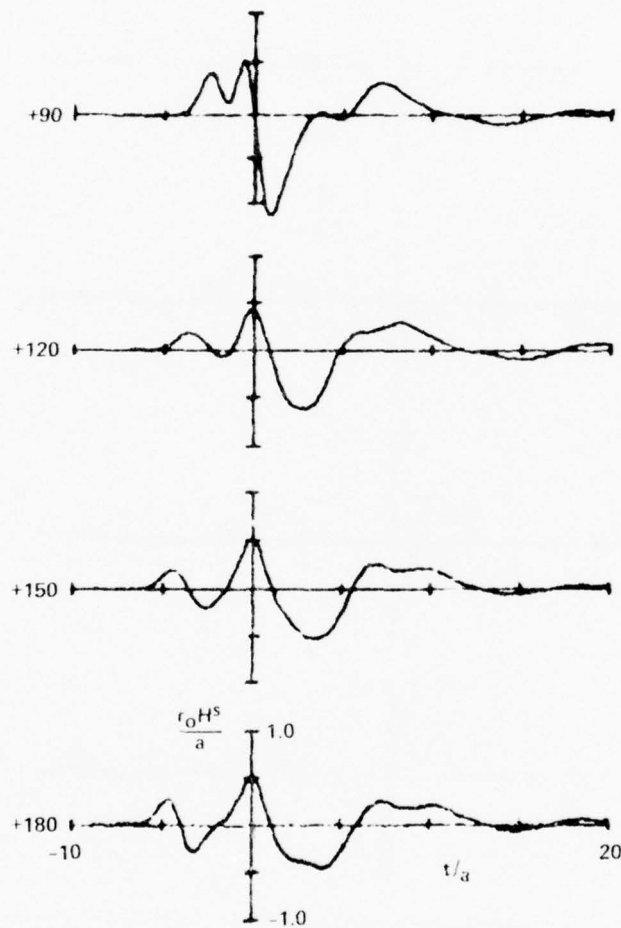


FIG. 15 Smoothed impulse response of finned cylinder at various angles of incidence for TE polarization.

functions for the rectangular plate and the right circular cylinder [6].
Thus, the augmentation function is given by

$$\begin{aligned}
 f_a(t) = & D_{z_1} \delta'(t/a - T_{zF_1}) + P_{z_1} \delta(t/a - T_{zF_1}) + S_{z_1} U(t/a - T_{zF_1}) \\
 & + P_{z_2} \delta(t/a - T_{zF_2}) + H_{z_3} (t/a - T_{zF_3})^{-\frac{1}{2}} U(t/a - T_{zF_3}) \\
 & + D_z \delta'(t/a - T_{zC_1}) + P_z \delta(t/a - T_{zC_1}) \\
 & + G_z (t/a - T_{zC_1})^{-3/2} U(t/a - T_{zC_1}) \\
 & + A_1 (t/a - T_{zC_1})^{-\frac{1}{2}} U(t/a - T_{zC_1}) \\
 & + A_2 (t/a - T_{zC_2})^{-\frac{1}{2}} U(t/a - T_{zC_2}) \\
 & + A_3 (-t/a + T_{zC_3})^{-\frac{1}{2}} U(-t/a + T_{zC_3}) \\
 & + f_{a_4}(t/a - T_{zC_4})
 \end{aligned} \tag{23}$$

where

- D_{z_1} = the doublet coefficient given by the physical optics approximation for the fin at broadside incidence
- P_{z_1} = the impulse coefficient due to the near edge of the fin
- S_{z_1} = the step coefficient due to the response from the sides of the fin
- P_{z_2} = the impulse coefficient due to the far edge of the fin
- H_{z_3} = the $t^{-\frac{1}{2}}$ pseudo-function coefficient due to surface traveling waves on the fin
- D_z = the doublet coefficient given by the physical optics approximation for the cylinder at axial incidence.

P_z = the impulse coefficient for the cylinder at axial incidence

G_z = the $t^{-3/2}$ pseudo-function coefficient due to the specular return from the side of the cylinder at broadside incidence

A_1, A_2, A_3 = the $t^{-1/2}$ pseudo-function coefficients due to the return from the edges of the cylinder

T_{zF1} = the time at which the leading edge of the impulse response from the fin begins

T_{zF2} = the time at which the singular contribution from the far edge of the fin begins

T_{zF3} = the time at which the singular contribution from the single excursion traveling wave on the fin begins

$T_{zC1}, T_{zC2}, T_{zC3}$ = the time at which the singular returns from three edges of the cylinder begin

T_{zC4} = the time at which the cylinder creeping wave appears

$$f_{a4}(t/a - T_{zC4}) = F^{-1} A_4 e^{-B\omega^{1/3}} e^{-j\omega T_{zC4}}$$

A_4 = the cylinder creeping wave coefficient

$$B = 2.051$$

The values used for the above parameters are summarized in Table 1. They were previously obtained for the case of the right circular cylinder and the rectangular plate [5,6].

Once the augmentation function is obtained, the augmented frequency response is calculated by subtracting the transform of the augmentation function from the frequency response. The high frequency estimate used to obtain the estimate of the total augmented frequency response takes the form

TABLE 1
SUMMARY OF PARAMETERS USED TO REPRESENT
THE AUGMENTATION FUNCTION AND THE AUGMENTED FREQUENCY RESPONSE

Parameter	Angle of Incidence						
	0°	30°	60°	90°	120°	150°	180°
D _{z1}	0	0	0	1.273	0	0	0
P _{z1}	0.701	0.686	0.955	-0.317	0.955	0.686	0.701
S _{z1}	-0.166	-0.181	-0.260	0	-0.260	-0.181	-0.166
P _{z2}	-0.224	-0.049	-0.318	0	-0.318	-0.049	-0.224
H _{z3}	0	0	0	0.203	0	0	0
D _z	0.5	0	0	0	0	0	0.5
P _z	0.141	0	0	0	0	0	0.141
G _z	0	0	0	-0.318	0	0	0
A ₁	-0.035	0.382	0.290	-0.123	0.290	0.382	-0.035
A ₂	-0.284	-0.016	-0.081	0	-0.081	-0.016	-0.284
A ₃	0	-0.106	-0.012	0	-0.012	-0.106	0
T _{zF1}	-4.0	-3.464	-2.0	0	0	0	0
T _{zF2}	0	0	0	0	2.0	3.464	4.0
T _{zF3}	0	0	0	4.0	0	0	0
T _{zC1}	-4.0	-4.464	-3.732	-2.0	-3.732	-4.464	-4.0
T _{zC2}	4.0	2.464	0.268	-2.0	0.268	2.464	4.0
T _{zC3}	0	-2.464	-0.268	2.0	-0.268	-2.464	0
T _{zC4}	5.9	5.754	5.025	3.037	5.025	5.754	5.9
A ₄	3.428	3.272	1.449	4.587	1.449	3.272	3.428
ω _C	1.4	2.05	2.0	1.8	2.5	2.05	2.0

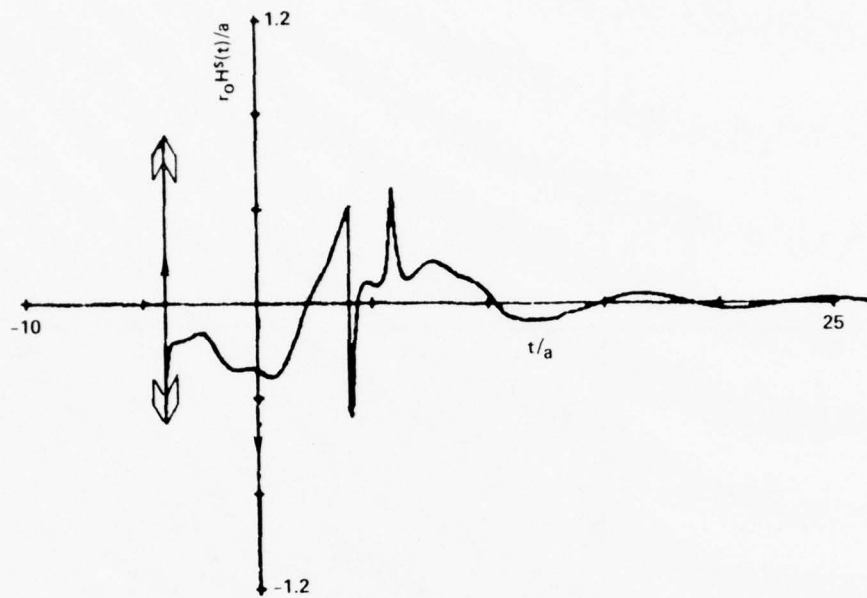
$$\hat{H}_a(\omega) = \begin{cases} H_a(\omega) & ; \omega \leq \omega_c \\ A H_a(\omega) e^{-\left(\frac{\omega}{2n}\right)^2} & ; \omega \geq \omega_c \end{cases}$$

where the cutoff point ω_c is chosen such that the phase of $H_a(\omega)$ is still in the linear region and A is computed so that $\hat{H}_a(\omega_c) = H_a(\omega_c)$. These coefficients are also displayed in Table 1. The results for the impulse response and the frequency response are displayed in Figs. 16-22 and described in the following.

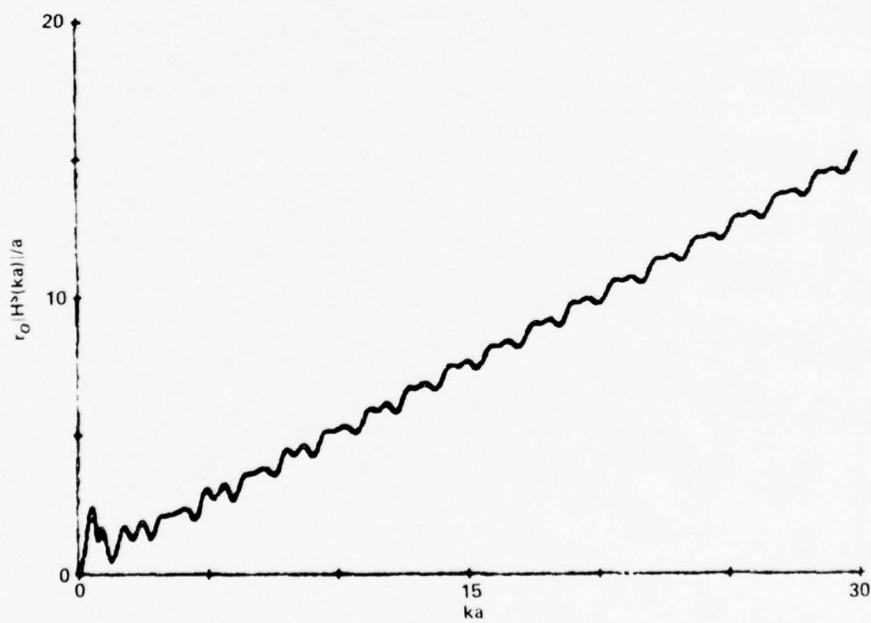
3.3 RESULTS

TE impulse response of the finned cylinder for axial incidence is displayed in Fig. 16a and the corresponding frequency response is displayed in Fig. 16b. The initial return of the impulse response at $t/a = -4.0$ consists of a doublet, impulse, and $t^{-\frac{1}{2}}$ pseudo-function from the cylinder face and edge. Also contained in this leading edge of the impulse response is an impulse with a positive sign due to the fin edge. This is followed at $t/a = 0$ by a negative impulse from the far fin edge. At $t/a = 4$ there appears a $t^{-\frac{1}{2}}$ pseudo-function from the far cylinder edge. Finally, a creeping wave can be observed at $t/a \approx 6$. In Fig. 16b the corresponding frequency response is displayed. This response increases linearly with increasing frequency due to the doublet in the impulse response at $t/a = -4$. The ripples in this response are mainly due to the interference between this doublet and the returns from the far fin edges, the far end of the cylinder, and the creeping wave.

The TE impulse response and frequency response of a finned cylinder is shown for a 30° angle of incidence in Fig. 17. The initial return from the near edge of the cylinder face appears at $t/a \approx -4.5$. This is followed at $t \approx -3.5$ by a positive impulse and a negative step from the near fin edge. Next, a "backward" $t^{-\frac{1}{2}}$ pseudo-function appears at $t/a \approx -2.5$ from the far



(a) Impulse Response



(b) Frequency Response

FIG. 16 TE response of finned cylinder with radius a for 0° angle of incidence.

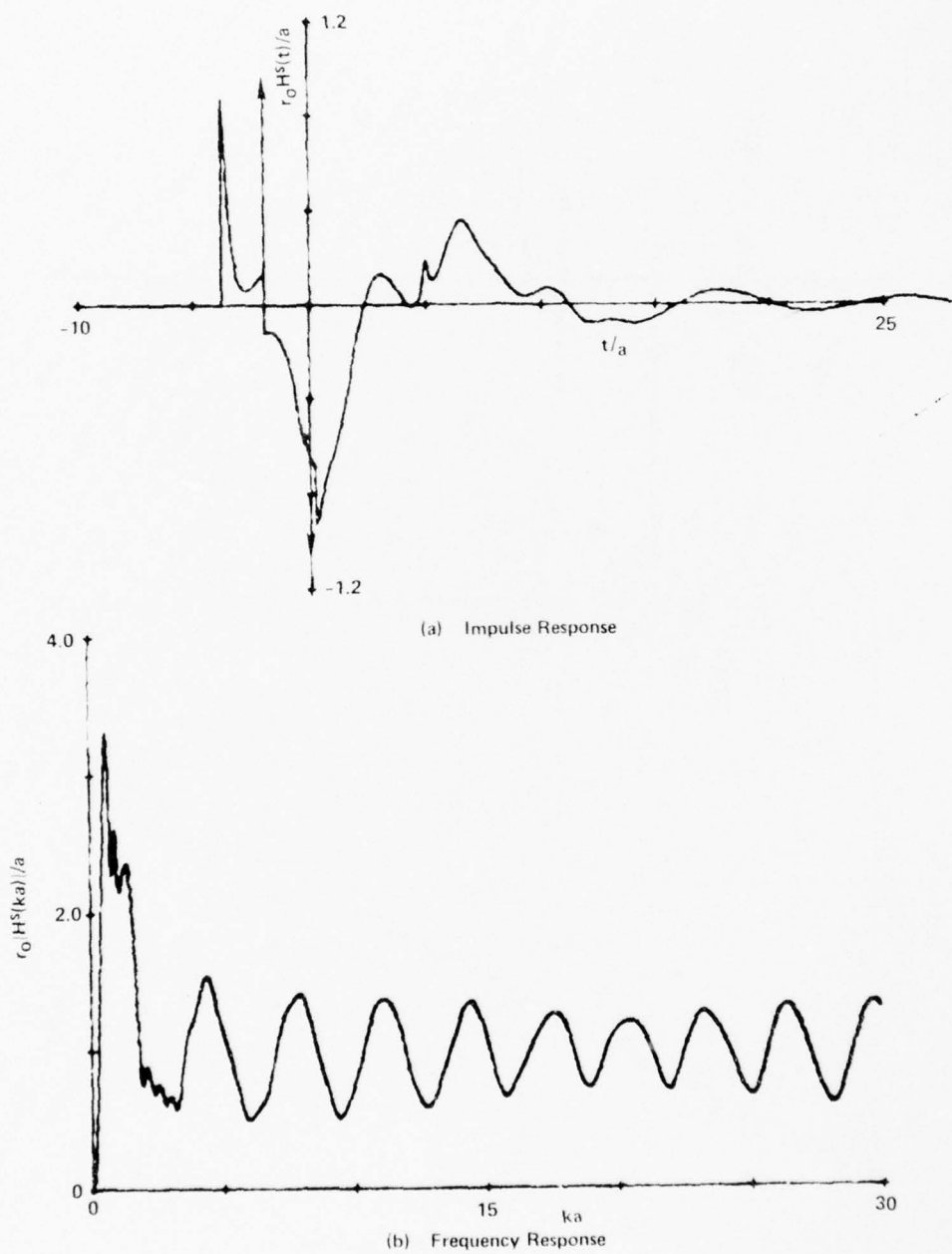
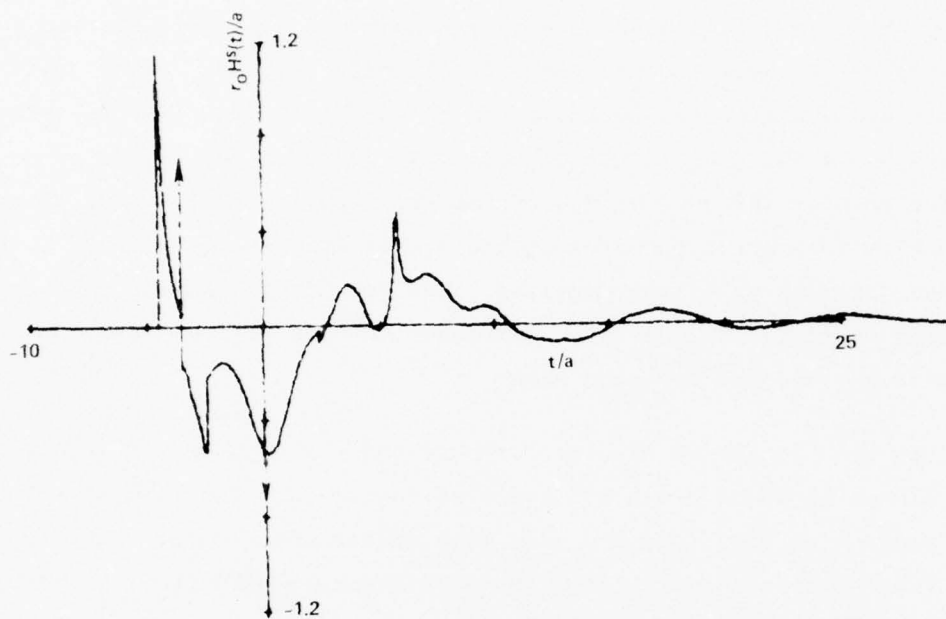


FIG. 17 TE response of finned cylinder with radius a for 30° angle of incidence.

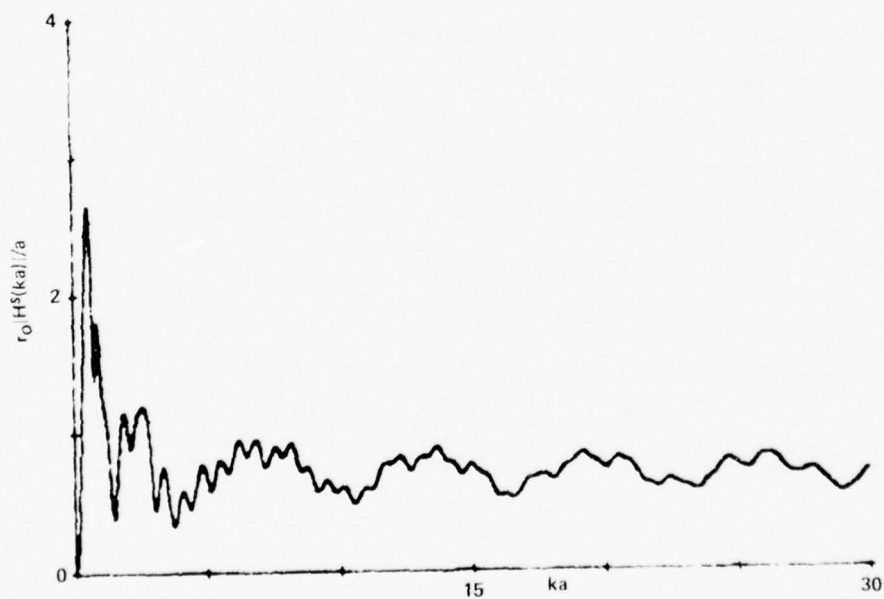
edge of the front face. At $t/a=0$ a negative impulse is observed due to the far edge of the fin. Following this is a negative $t^{-\frac{1}{2}}$ pseudo-function from the far edge of the cylinder at $t/a \approx 2.5$. Finally at $t/a \approx 5.8$ the creeping wave that travels around the cylinder can be seen. In Fig. 17b the corresponding frequency response is displayed. This response approaches a constant value at high frequencies due to the two impulses from the edges of the fin. The slow resonances observed at the higher frequencies are due to the interference between these two impulses. The more rapid ripples superimposed on this slow waveform are due to interference between the impulses, the $t^{-\frac{1}{2}}$ pseudo-functions and the creeping wave.

In Fig. 18 the TE impulse response and the frequency response of a finned cylinder is shown for a 60° angle of incidence. The initial return is a $t^{-\frac{1}{2}}$ pseudo-function from the near edge of the front face. This is followed at $t/a=-2$ by a positive impulse and a negative step from the near edge of the fin. Next, at $t/a \approx -.3$ appears a "backward" $t^{-\frac{1}{2}}$ pseudo-function followed at $t/a=0$ by a negative impulse from the far edge of the fin. Next at $t/a \approx +.3$ a $t^{-\frac{1}{2}}$ function occurs due to the near edge of the far cylinder face. Finally, at $t/a \approx 5.0$ the creeping wave that travels around the cylinder can be observed. In Fig. 18a the corresponding frequency response is displayed. As the frequency increases, this response continues to ripple about a constant value due to the interference between the two impulses from the fin edges.

The TE impulse response and frequency response for the finned cylinder at a 90° aspect angle is shown in Fig. 19. The initial return in the impulse response is a $t^{-3/2}$ pseudo-function together with a negative impulse. Next, at $t/a=0$ appears a doublet and a negative impulse due to the return from the face and edge of the fin. This is followed at $t/a \approx 3.1$ by the effect of a creeping wave that travels around the cylinder. In Fig. 19b the corresponding frequency response is shown. One can observe in this figure that the frequency response increases linearly with frequency due to the doublet. Moreover, it oscillates about this ever increasing value due to the interference between the doublet and the $t^{-3/2}$ pseudo-function.

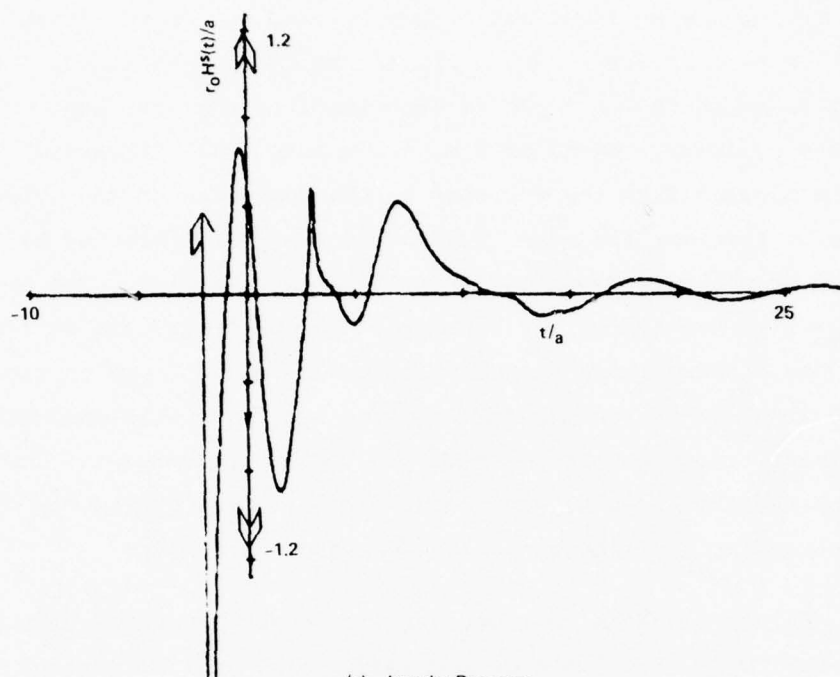


(a) Impulse Response

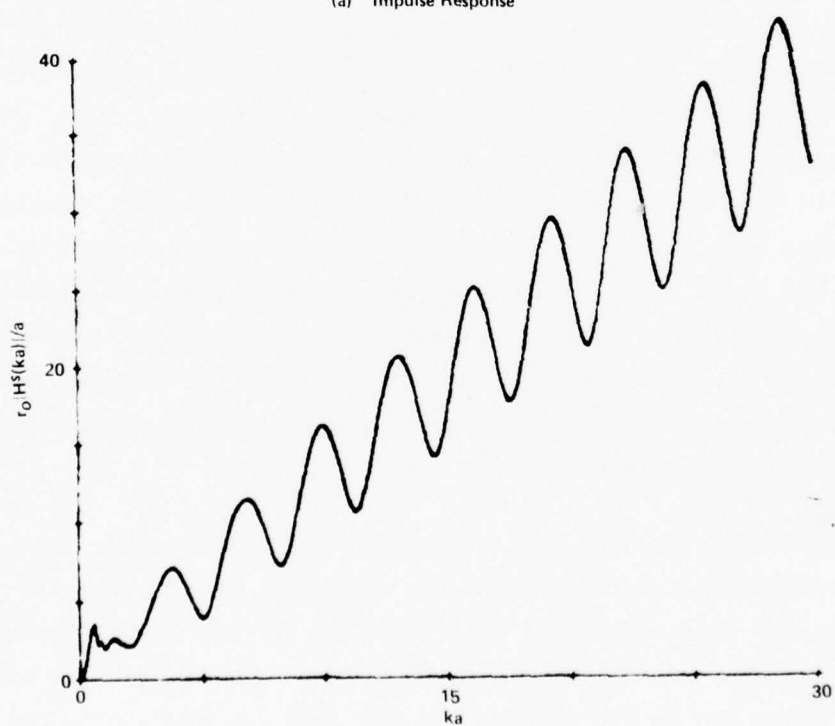


(b) Frequency Response

FIG. 18 TE response of finned cylinder with radius a for 60° angle of incidence.



(a) Impulse Response



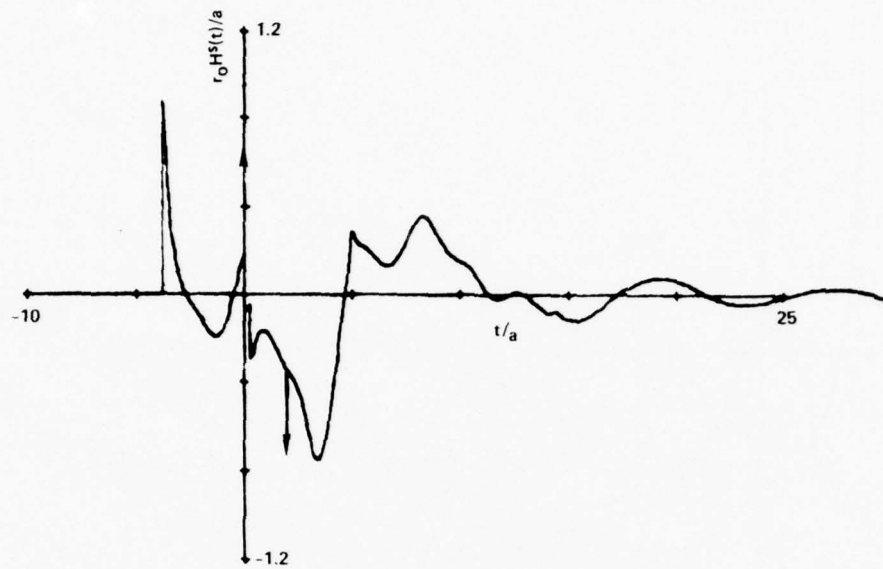
(b) Frequency Response

FIG. 19 TE response of finned cylinder with radius a for 90° angle of incidence.

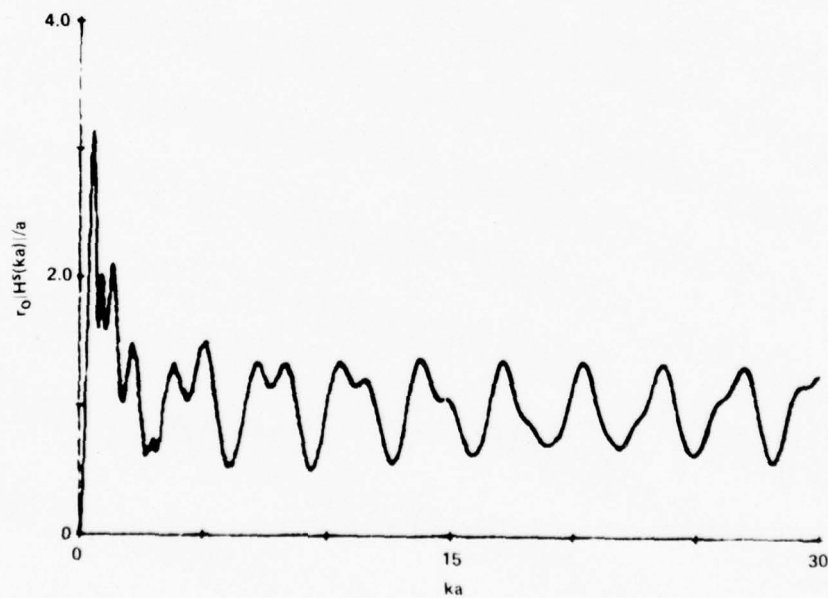
The TE impulse response and frequency response of the finned cylinder is shown in Fig. 20 for a 120° angle of incidence. The initial return of the impulse response is a $t^{-\frac{1}{2}}$ pseudo-function from the near edge of the near face of the cylinder. Next, at $t/a \approx -.3$ a very small "backward" $t^{-\frac{1}{2}}$ pseudo-function appears from the far edge of the near face of the cylinder. An impulse due to the near fin edge is observed at $t/a = 0$ followed by a $t^{-\frac{1}{2}}$ pseudo-function from the far edge of the cylinder at $t/a \approx +.3$. The negative impulse at $t/a = 2$ is due to the far fin edge. The creeping wave at $t/a \approx 5.0$ can be seen. The corresponding frequency response is displayed in Fig. 20b. Again, the two impulses in the impulse response interfere with each other to give an oscillating frequency response at the higher frequencies. The $t^{-\frac{1}{2}}$ pseudo-function and the creeping wave cause distortion of what would otherwise be a very regular oscillation in the frequency response.

Fig. 21 displays the TE impulse response and frequency response of a finned cylinder for a 150° angle of incidence. The initial part of this response at $t/a \approx -4.5$ is a $t^{-\frac{1}{2}}$ pseudo-function from the near edge of the near face of the cylinder. This is followed at $t/a \approx -2.5$ by a "backward" $t^{-\frac{1}{2}}$ pseudo-function from the far edge of the near face of the cylinder. At $t/a = 0$ the impulse and negative step from the near fin edge occurs. Following this at $t/a \approx 2.5$ a $t^{-\frac{1}{2}}$ pseudo-function appears due to the far edge of the far cylinder face. This is followed by a small negative impulse at $t/a = +4$ from the far fin edge. Finally, the creeping wave can be seen at $t/a \approx 5.8$ in the impulse response. The corresponding frequency response shown in Fig. 21b again approaches a constant value at high frequencies. The rippling in this structure is due to the interference between the impulse, the $t^{-\frac{1}{2}}$ pseudo-functions, and the creeping wave.

Fig. 22 displays the TE impulse response and frequency response of a finned cylinder for a 180° angle of incidence. The doublet and impulse that appear at the leading edge of this response are due to the specular and edge returns from the front face of the cylinder. The impulse and negative step at $t/a = 0$ are due to the return from the near fin edge. The return due to the far fin edge and far cylinder appears at $t/a = 4$ and finally the

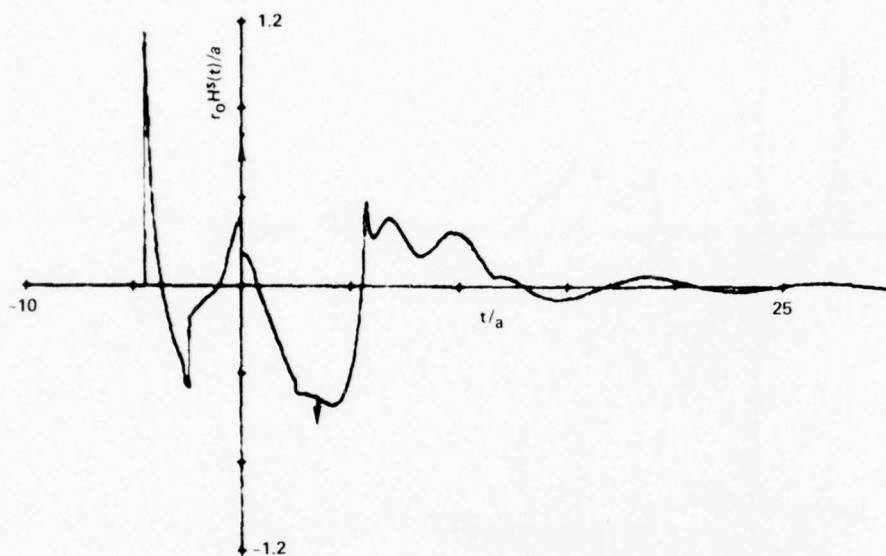


(a) Impulse Response

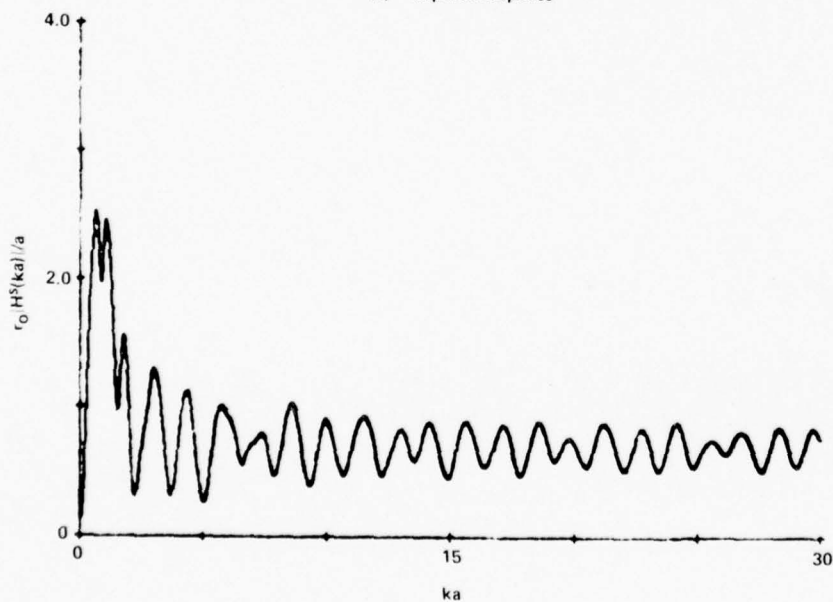


(b) Frequency Response

FIG. 20 TE response of finned cylinder with radius a for 120° angle of incidence.

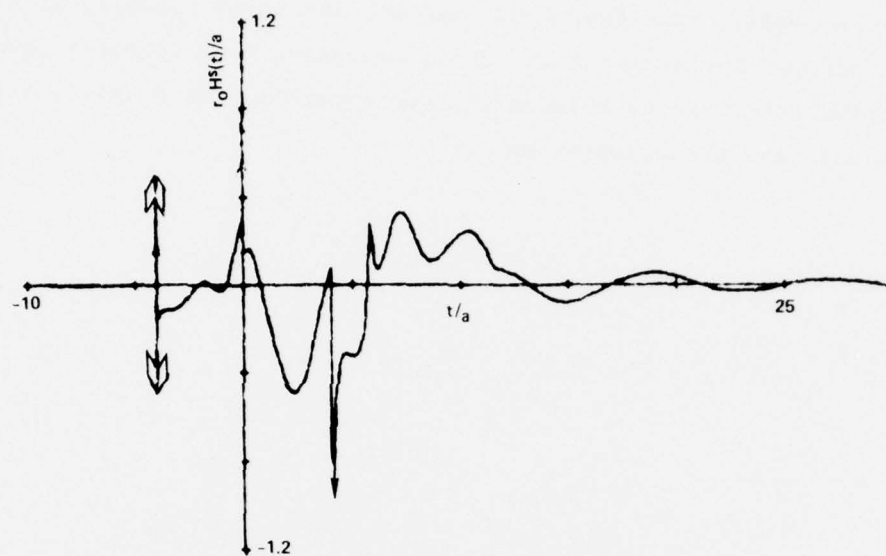


(a) Impulse Response

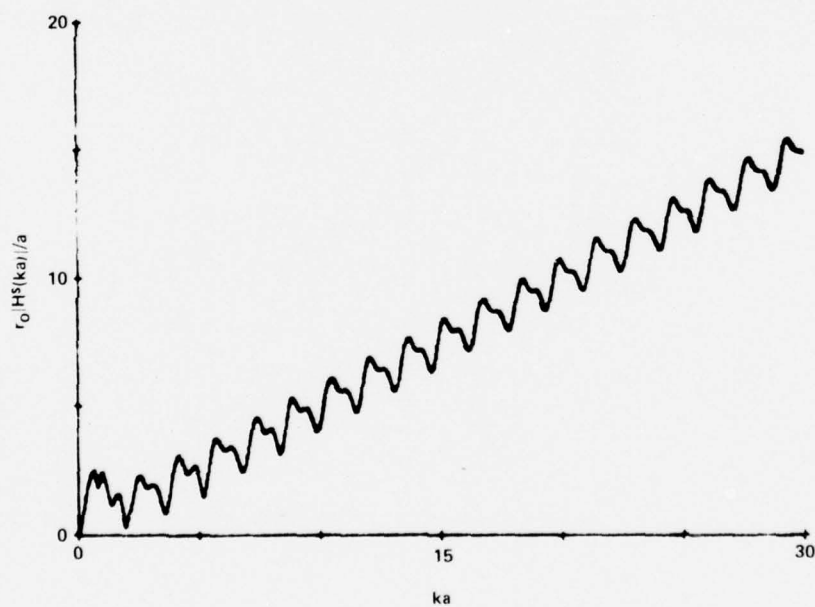


(b) Frequency Response

FIG. 21 TE response of finned cylinder with radius a for 150° angle of incidence.



(a) Impulse Response



(b) Frequency Response

FIG. 22 TE response of finned cylinder with radius a for 180° angle of incidence.

creeping wave can be seen at $t/a \approx 6$. The corresponding frequency response is displayed in Fig. 22b. This frequency response increases linearly with increasing frequency. Furthermore, it oscillates about this linearly increasing value due to the interference between the two impulses, the doublet, the $t^{-\frac{1}{2}}$ pseudo-functions, and the creeping wave.

SECTION 4

TIME DOMAIN INVERSE SCATTERING - AXIAL INCIDENCE

The inverse scattering problem consists of determining the structure of an unknown scatterer given information about a field incident upon the scatterer and the response of the scatterer to that field. Most of the attempts at solving the inverse scattering problem have been carried out in the frequency domain. The inherent advantages of employing time domain techniques appear to have been first documented by Kennaugh and Cosgriff [11]. They showed that if physical optics currents were postulated on the surface of the scatterer, then they produced an approximate impulse response that was simply the second derivative of the projected area function of the scatterer.

Many researchers have developed approaches [12,13] to the inverse scattering problem that have been based on extensions of this result. Another approach based on polarization information in the impulse response has also been developed [14,15]. These approaches have reproduced the scatterer geometry with varying degrees of success. This would be expected since the relation between the impulse response and the two derivatives of the area function is exact only at the leading edge of the scattered field response, a single point in time. After the leading edge, the response is altered by currents arriving from other space points. Therefore, the physical optics solution must be "corrected" by these currents flowing on the body. For a given object, if the incident pulse width is short compared to body size (the optical limit) then the correction currents will have a small effect, and optical rays can be placed in one-to-one correspondence with points on the body. On the other hand, if the size of the body is comparable to a pulse width, then the "correction" terms have a strong effect on the solution and the physical optics solution is degraded. In the case of small bodies, the correction terms dominate the result and the physical optics solution is meaningless.

In this study, the inverse scattering problem is formulated as an inversion of the space-time integral equation. This approach to determining

the response of the scatterer incorporates both the effects of the incident field directly and those due to the correction currents flowing on the body and was first suggested in 1974 [5]. By using a complete description of the surface current interactions, this formulation should yield a very close approximation to the target geometry.

4.1 DERIVATION OF EQUATIONS

In order to derive the inversion procedure, it is necessary to first examine the direct solution of the scattering problem. The direct problem consists of determining the scattered field given a description of the incident field and the scatterer geometry. This problem is solved by first computing the currents flowing on the scatterer surface. From these currents the scattered field can be calculated directly.

The expression for the surface currents is derived from an expression for the total field at an arbitrary point in space (see Sec. 2.2.1). This arbitrary point is specialized to a point on the scatterer surface and the appropriate boundary conditions are applied. This yields an equation for the surface current \vec{J} at point \vec{r} on the scatterer surface and time t as

$$\vec{J}(\vec{r}, t) = 2\hat{a}_n \times \vec{H}^i(\vec{r}, t) + \vec{J}_c(\vec{r}, t) \quad (24)$$

where

$$\vec{J}_c(\vec{r}, t) = \frac{1}{2\pi} \int_S \hat{a}_n \times \left[\frac{1}{R} + \frac{1}{R} \frac{\partial}{\partial \tau} \right] \vec{J}(\vec{r}', \tau) \times \hat{a}_R \, dS'$$

$$\tau = t - R$$

$\vec{H}^i(\vec{r}, t)$ = incident magnetic field

\hat{a}_n = unit vector normal to surface

\vec{r} = position vector to observation point

\vec{r}' = position vector to integration point

$$R = |\vec{r} - \vec{r}'|$$

$$\hat{a}_R = \frac{\vec{r} - \vec{r}'}{R}$$

t = time in light-meters.

The first term on the right-hand side of Eq. (24) may be considered the source term and represents the direct influence of the incident field on the current at the observation point (\vec{r}, t) . Moreover, this term, when applied to the illuminated side of the scatterer, yields the familiar physical optics approximation for the surface current. The second term on the right-hand side of Eq. (24) represents the influence of currents at other surface points on the current at (\vec{r}, t) . It is important to note that the influence of the current at other points on the surface on the current at (\vec{r}, t) is delayed in time by R , the distance between the two points. This allows Eq. (24) to be solved by a "marching on in time" procedure rather than necessitating matrix inversion.

Once the surface currents have been determined the far scattered field can be calculated from them using

$$\vec{H}^S(\vec{r}, t) = \frac{1}{4\pi r_0} \frac{\partial}{\partial \tau} \int \vec{J}(\vec{r}', \tau) \times \hat{a}_r \, dS' \quad (25)$$

$$\tau = t - R$$

where

r_0 = distance to the far-field observer

\hat{a}_r = unit vector from the integration point to the far-field observer.

If the surface current expression in Eq. (24) is substituted in Eq. (25), then the result is

$$\begin{aligned}
r_{0I} \vec{H}^S(\vec{r}, t) &= \frac{1}{4\pi} \frac{\partial}{\partial \tau} \int \left(2\hat{a}_n \times \vec{H}^i(\vec{r}', \tau) \times \hat{a}_r \right) dS' \\
&\quad \tau = t - R \\
&+ \frac{1}{4\pi} \frac{\partial}{\partial \tau} \int \left(\vec{J}_c(\vec{r}', \tau) \times \hat{a}_r \right) dS' \\
&\quad \tau = t - R
\end{aligned} \tag{26}$$

If the incident field is an impulse, then the first term in Eq. (26) is simply the term that has been recognized previously [11] to be proportional to the second derivative of the area function. Assuming the incident wave is an electromagnetic impulse, then Eq. (26) becomes

$$\begin{aligned}
r_{0I} \vec{H}^S(\vec{r}, t) &= \frac{1}{2\pi} \frac{\partial^2 S(t_s)}{\partial t^2} \hat{a}_H + \frac{1}{4\pi} \frac{\partial}{\partial \tau} \int \left(\vec{J}_{cI}(\vec{r}', \tau) \times \hat{a}_r \right) dS' \\
&\quad \tau = t - R
\end{aligned} \tag{27}$$

where

$r_{0I} \vec{H}^S(\vec{r}, t)$ = the impulse response of the target

$S(t_s)$ = the silhouette area of the scatterer as delineated by the incident impulse assumed moving over the scatterer at one half the free-space velocity

r_0 = distance of far-field observer from the origin

$$t = t_s + r_0$$

$$\hat{a}_H = \frac{\vec{H}^i}{|\vec{H}^i|}$$

$\vec{J}_{cI} = \vec{J}_c$ that results from an incident impulse.

This equation may be simplified by integrating twice to obtain

$$\vec{r}_{OR}^{\vec{S}}(\vec{r}, t) = \frac{1}{2\pi} S(t_S) \hat{a}_H + \frac{1}{4\pi} \frac{\partial}{\partial \tau} \int_S \vec{J}_{CR}(\vec{r}', \tau) \times \hat{a}_r dS' \quad (28)$$

$$\tau = t - R$$

where

$\vec{r}_{OR}^{\vec{S}}$ = the ramp response of the target

$\vec{J}_{CR} = \vec{J}_C$ that results from an incident ramp waveform.

Thus, by direct consideration of the space-time integral equation the exact relationship between the target response and the target geometry has been obtained. In particular, Eq. (28) gives the target ramp response in terms of both the target area function and the contribution due to the "correction currents," \vec{J}_C . Moreover, it is important to note that the correction currents as given in Eq. (24) are time-retarded functions of currents at other space points, and thus will be zero at the leading edge of the incident wavefront as it travels across the target. It is this feature, exclusive to the time domain formulation, that allows the determination of the target geometry from its ramp (or equivalently, impulse) response.

4.2 NUMERICAL SOLUTION

In order to test the effectiveness of this approach, the technique was applied to the class of rotationally symmetric scatterers. The rotationally symmetric scattering problem is depicted in Fig. 23. For this case the scatterer is symmetric about the z-axis, the incident field is axially incident, and the far field is computed in the backscatter direction. The contour of a rotationally symmetric object can be completely described by the radius vector ρ which varies as a function of z , and its projected area function can be expressed simply as

$$S = \pi \rho^2(z, t) .$$

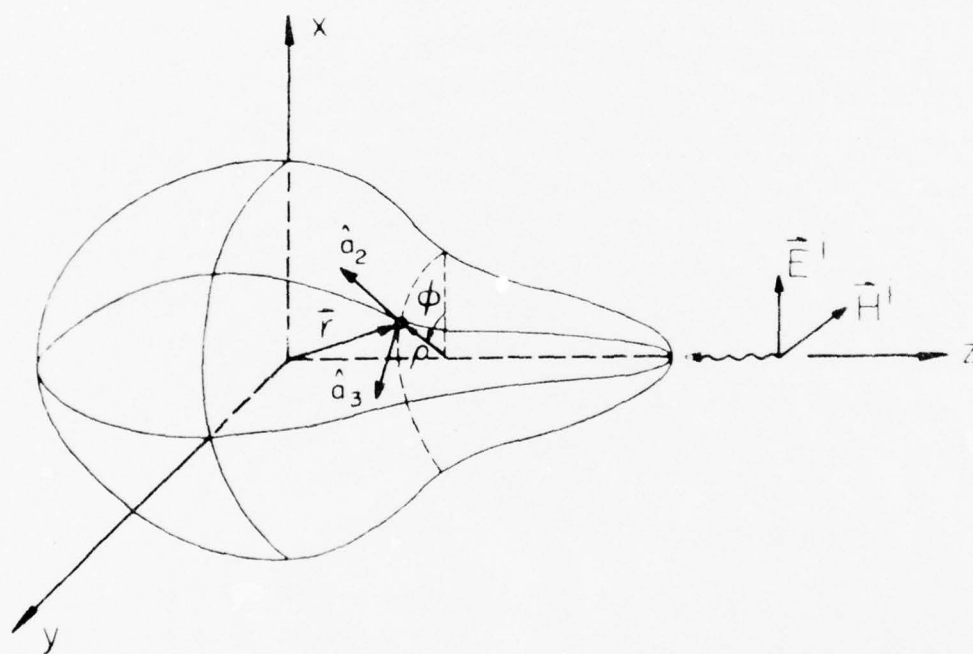


FIG. 23 Geometry of rotationally symmetric scattering problem.

Substituting this projected area function into Eq. (28) and rearranging terms yields the inversion equation for the rotationally symmetric case

$$\rho(z,t) = 2r_{OR} \vec{H}_R^S(\vec{r},t) - \frac{1}{2\pi} \frac{\partial}{\partial \tau} \int_S \vec{J}_{CR}(\vec{r}',\tau) \times \hat{a}_r ds' \quad (29)$$

$$\tau = t - R$$

This equation gives $\rho(z,t)$ in terms of the target ramp response, which is known, and in terms of the correction currents at earlier times, which have either been previously computed or are known to be zero.

To solve this equation a technique was developed under a previous program [5] which iterated on estimates of the entire target geometry. For this program it was proposed to improve this technique using a direct time domain approach. In this approach the target geometry is generated sequentially in time as the incident field moves across the target. Geometry values are determined from the incident field, previously computed geometry values, and correction currents set up on the structure as a result of surface current interaction.

A flow chart of the direct solution procedure is shown in Fig. 24. The general approach is to step along the target contour in equally-spaced intervals. The value of $\rho(z,t)$ is computed at the center of each interval at the time at which the initial return from that point reaches the far field observer. This insures that the correction currents at that time are a function only of currents flowing on the portion of the target whose contour is already known.

The solution procedure begins with an estimate of $\rho(z,t)$ for the first interval along the target contour. The placement of the interval is obtained by assuming the target is locally spherical at the specular point. The value of $\rho(z,t)$ at the center of the interval is computed from Eq. (29) by neglecting the surface integral, giving

$$\rho(z_1,t) = [2r_{OR} \vec{H}_R^S(\vec{r},t)]^{\frac{1}{2}}.$$

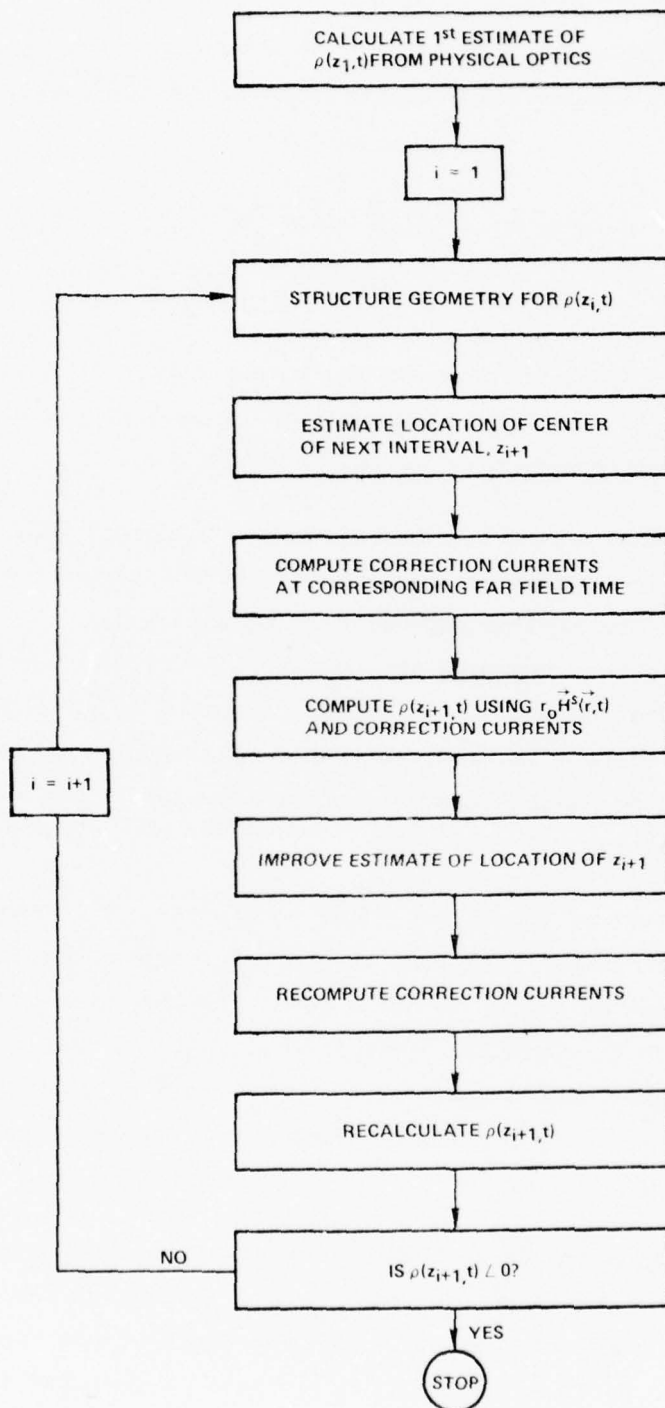


FIG. 24 Direct time domain solution procedure.

From this estimate, the geometry parameters necessary for the calculation of the correction currents are structured. This is accomplished by constructing a band around the target whose width is equal to that of the contour interval. The band is then divided into patches of equal area. The location of the center of the band z_1 , the corresponding radius vector $\rho(z_1, t)$, and the components of the unit normal at $\rho(z_1, t)$ are also necessary inputs.

Once the geometry of the first band has been structured, then an estimate is made of the location of the center of the next band. This is obtained by projecting the unit normal at $\rho(z_1, t)$ forward from $\rho(z_1, t)$ for one interval length and then finding the z_2 corresponding to the end of the interval. In order to compute the value of ρ at z_2 , it is necessary to compute the correction currents at the time t_2 at which the incident field reaches z_2 . This computation is done by an improved version of the program ROTSY which solves the direct scattering problem for rotationally symmetric targets. The details of this computation are described in Appendix 8.1. The radius vector $\rho(z_2, t)$ is then computed from Eq. (29) using the correction currents at t_2 and the value of the far scattered field at the time t_{f2} at which the initial return from z_2 reaches the far field observer.

The accuracy of the results obtained from the ROTSY program is improved if the target is divided into approximately equal bands. In order to insure this for the inversion solution, a second estimate is made of the location of the band center, z_2 . This estimate is obtained by constructing the band along the line between $\rho(z_1, t)$ and the first estimate of $\rho(z_2, t)$. Again, the correction currents are computed for the second estimate of z_2 and $\rho(z_2, t)$ is recalculated from Eq. (29).

Each value of $\rho(z_1, t)$ is tested to determine if it is negative. If it is, then the inversion procedure terminates. If it is not, then the geometry parameters for band i are computed and the structuring of band $i + 1$ begins. In this manner, the inversion technique generates the target geometry sequentially in time.

4.3 RESULTS

In order to test the direct solution procedure described in the previous section, a computer program INVERD was written to implement the procedure. This program was used to compute the contours of the four rotationally symmetric objects shown in Fig. 25:

- (1) A sphere
- (2) A cylinder with two sphere caps
- (3) A cylinder with a flat front end and a sphere-capped back end
- (4) A cylinder with a sphere-capped front end and a flat back end.

For the four objects, the radius of the spherical segments was 0.5 meters. The radius of the cylinder body was also 0.5 meters and its length was 1 meter. In all cases the incident field was axially incident and the far field was calculated in the backscatter direction. The ramp responses of the four objects are depicted in Fig. 26. Since these same four objects were also used to test the iterative solution technique which was previously developed [5], valid comparisons can be made between the two approaches.

The implementation of the direct solution procedure gave, in general, very good results. For all four targets the contours were reproduced with a high level of accuracy. The only discrepancies tended to occur at the back of the targets where the target size was slightly overestimated. Perspective plots were made of the actual target contours and the approximations to the contours using both the direct and iterative procedures. The coordinate axis and the view angle for the plots is shown in Fig. 27.

The results obtained for the four targets are shown in Figs. 28 - 31. For the case of the sphere (Fig. 28), the results are very close to the actual contour. The front of the sphere is reproduced exactly and there is only a slight overestimation of the back. For the cylinder with two sphere caps (Fig. 29), again there is the exact reproduction of the front sphere cap and the slightly enlarged back sphere cap. The cylinder side is esti-

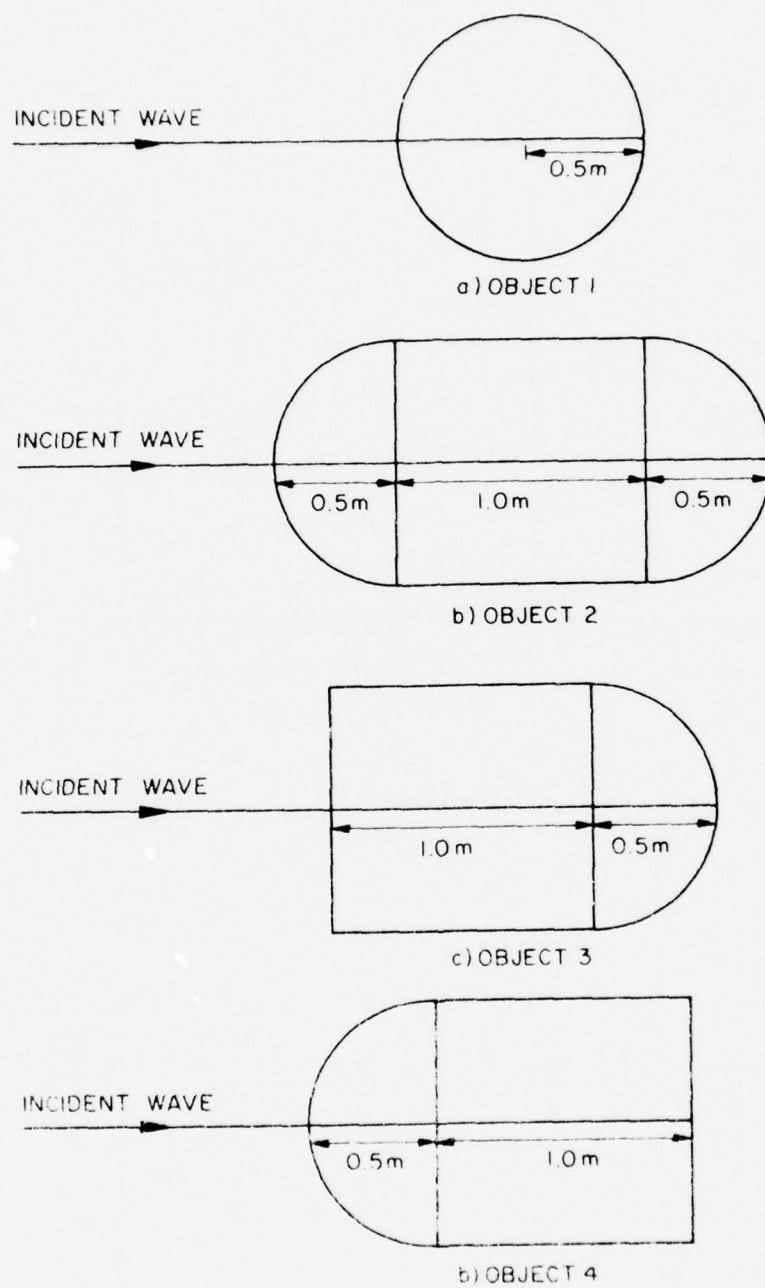


FIG. 25 Geometry of objects used for test of inversion procedure.

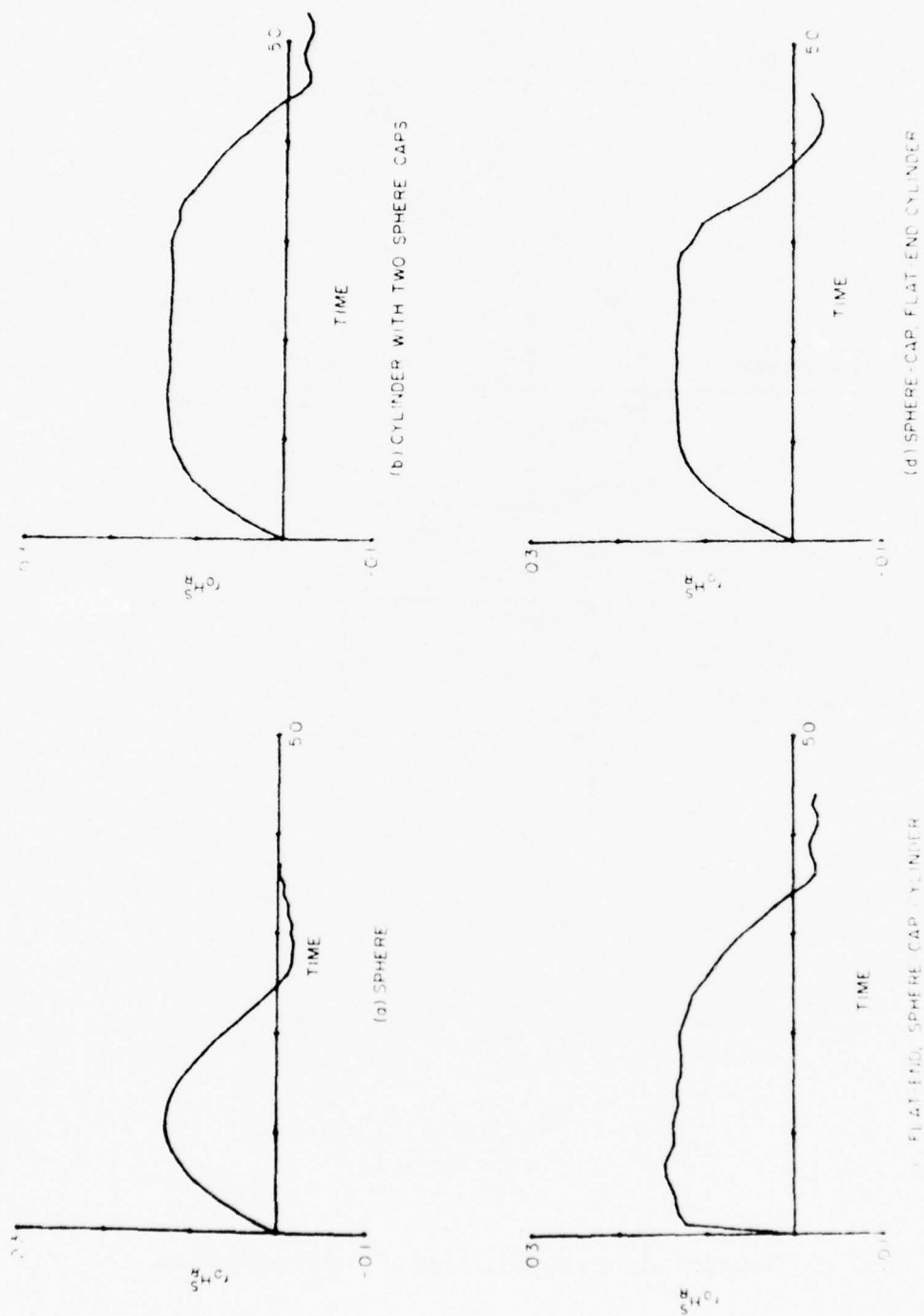


FIG. 26 Far field ramp response (backscatter direction) for four objects tested.

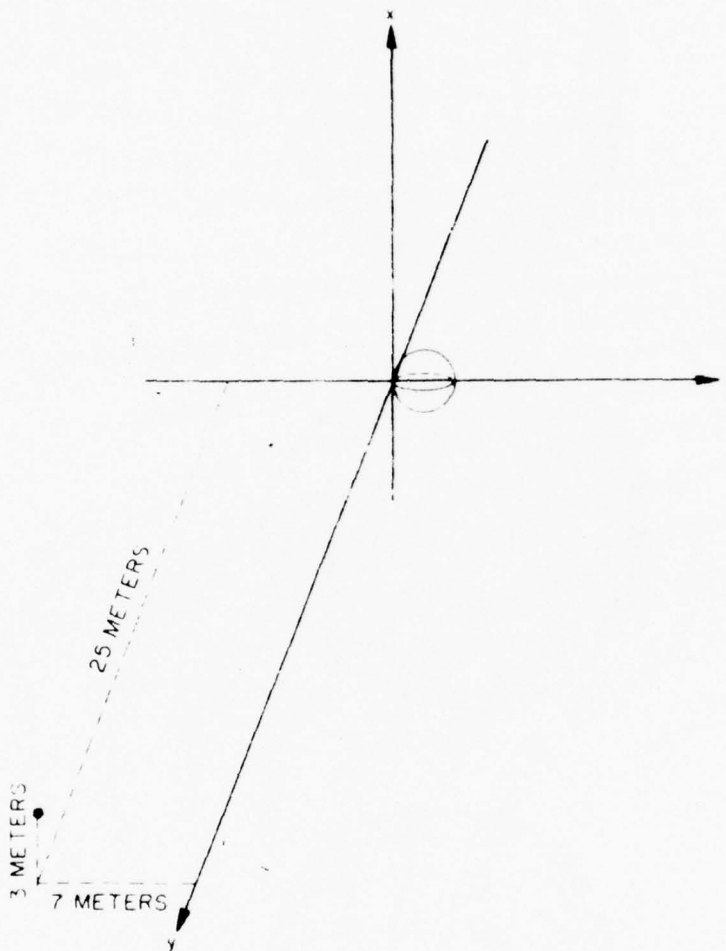
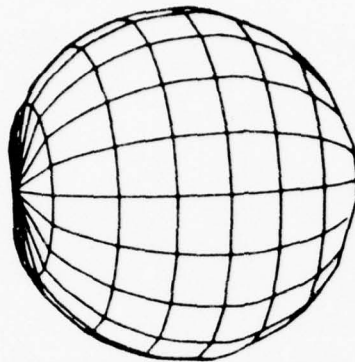
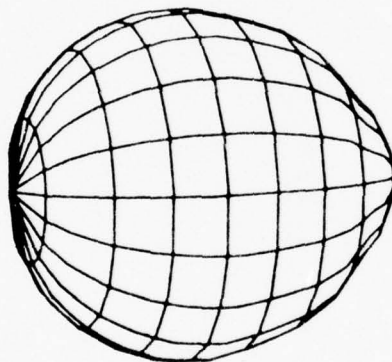


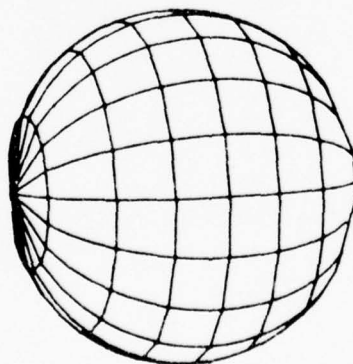
FIG. 27 Coordinate axes and view angle for perspective plots.



(a) Iterative Solution

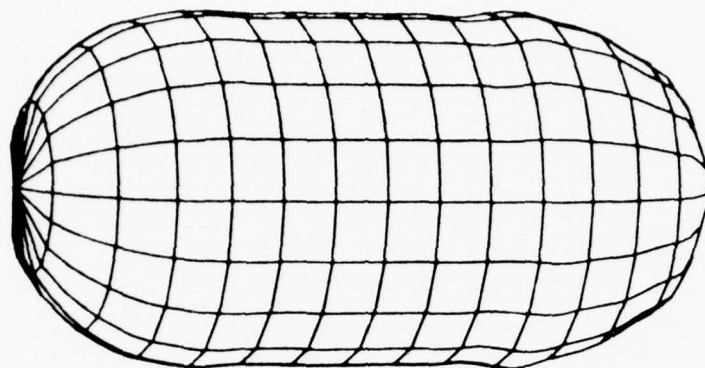


(b) Direct Solution

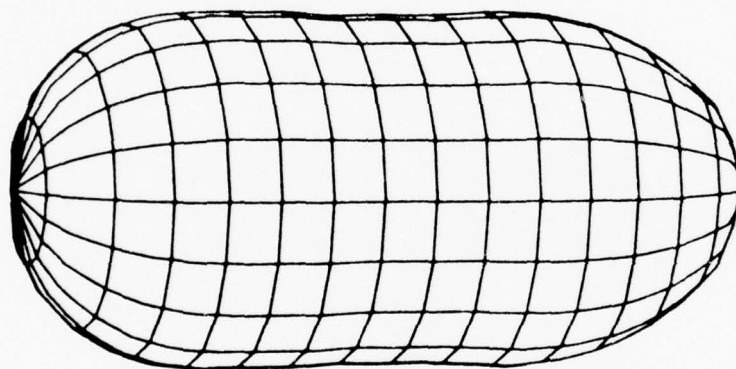


(c) Actual Contour

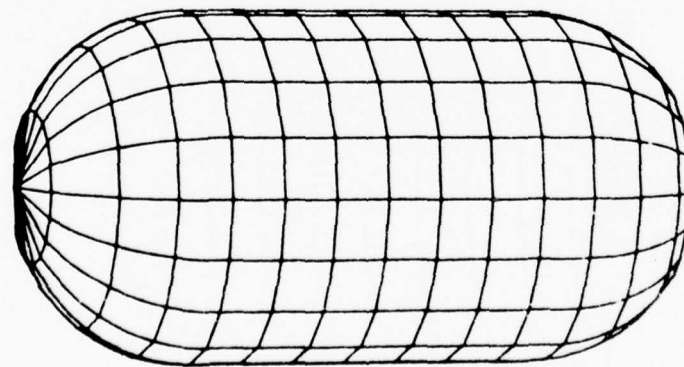
FIG. 28 Contour estimates for a sphere.



(a) Iterative Solution

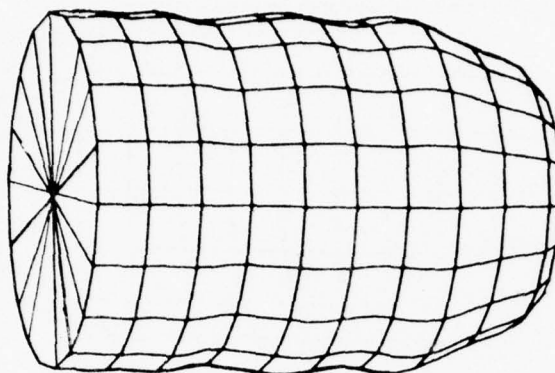


(b) Direct Solution

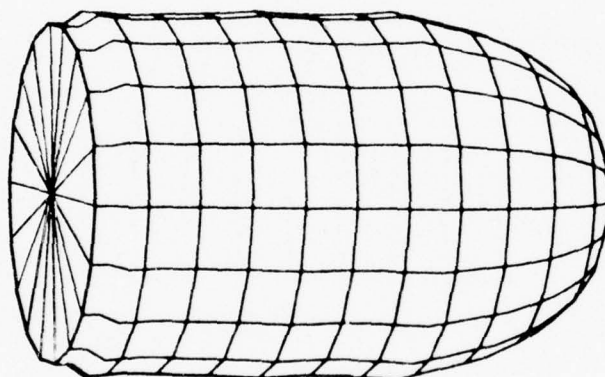


(c) Actual Contour

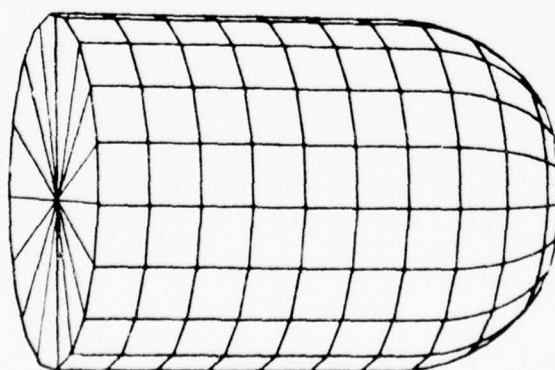
FIG. 29 Contour estimates for a cylinder with two sphere caps.



(a) Iterative Solution

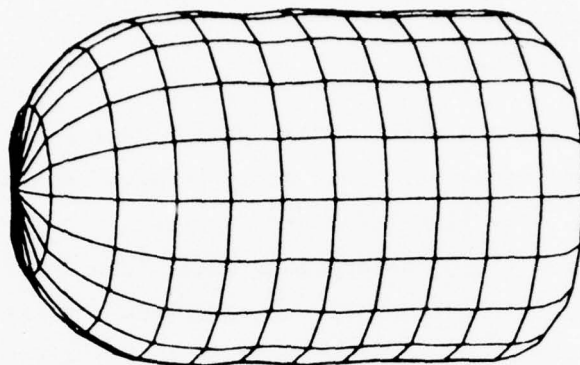


(b) Direct Solution

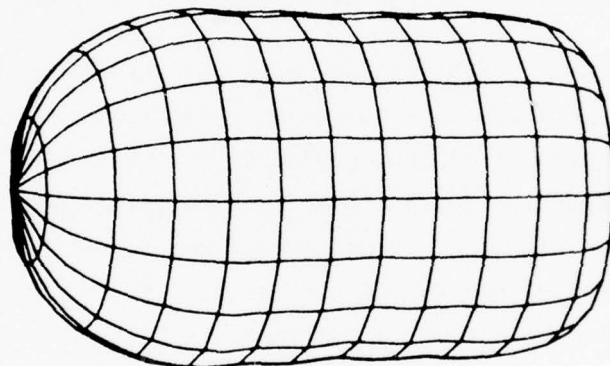


(c) Actual Contour

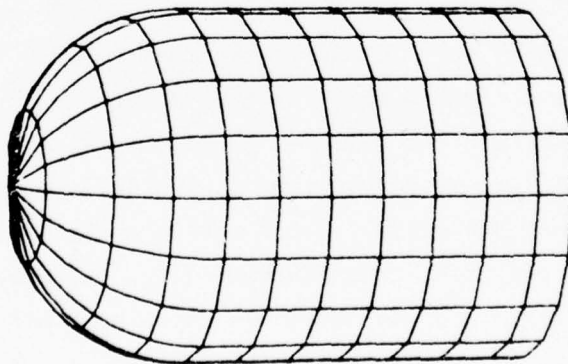
FIG. 30 Contour estimates for a cylinder with a flat front end and a sphere-capped back end.



(a) Iterative Solution



(b) Direct Solution



(c) Actual Contour

FIG. 31 Contour estimates for a cylinder with a sphere-capped front end and a flat back end.

mated quite accurately and is also somewhat smoother than estimate obtained using the iterative procedure.

Fig. 30 shows the results for the cylinder with the flat front end and the sphere-capped back end. This estimate also very closely approximates the target geometry. The flat front end is accurately recovered and there is again less oscillation along the cylinder sides than for the iterative results. As with the previous targets, there is the overestimation of the back sphere cap. It should be pointed out that for this target, it was determined from the initial $\rho(z,t)$ estimate that the front end of the target was flat and the geometry parameters were structured accordingly.

The results for the cylinder with the sphere-cap front and flat end back (Fig. 31) were not as accurate as for the other targets. This was expected, however, because of the difficulty in obtaining the numerical accuracy in the correction current computation necessary to exactly cancel the tail of the ramp response. Nonetheless, the direct approach did give a fairly close approximation to the flat back. It also very accurately reproduced the sphere-capped front and cylinder sides.

In comparing the direct solution to the iterative solution, the results indicate that the direct approach gives a better estimate for some cases while the iterative approach is better for others. The iterative solution is more accurate in reproducing the back sphere cap while the direct solution tends to approximate the cylinder sides more effectively and in general, give smoother target contours. The direct solution does, however, have one very important advantage. The solution technique allows for a substantial decrease in run time. The run time using the direct approach is cut by a factor equivalent to the number of iterations necessary for convergence in the iterative technique. This advantage, combined with the rather marginal differences in the results obtained, makes the direct technique a more favorable approach.

SECTION 5

TIME DOMAIN INVERSE SCATTERING - OBLIQUE INCIDENCE

In this section the problem of inverse scattering by rotationally symmetric targets with oblique incidence is considered. It is shown that the geometry of a scatterer can be obtained from simultaneous processing of its responses at two polarizations for the class of rotationally symmetric targets at arbitrary (known) angle of observation. Section 5.1 gives a background of the problem and the inverse scattering equations are derived in Sec. 5.2. The first order ramp response of a curvilinear square patch is developed in Sec. 5.3 and used in the numerical solution procedure that is described in Sec. 5.4. The results for three targets are presented in Sec. 5.5.

5.1 GENERAL PROBLEM

It has been known for some time that the impulse response of a scatterer in the physical optics limit is the second derivative of its projected area function [11]. Equivalently, the ramp response itself is simply the projected area function. Based on this physical optics approximation, reasonably accurate schemes have been developed for obtaining target geometry from the area function [12,13]. This technique is strictly valid only in the limit of very high frequencies, or equivalently, at the leading edge of the ramp response. When the wavelength is of the order of the target dimension, the solution is degraded due to the existence of surface current interactions. Using the space-time integral equation techniques, the effects of these "correction currents" can be included. This was first done [5] for rotationally symmetric bodies at axial incidence, using an iterative technique. In Sec. 4 of this report the technique was modified for direct solution for this class of targets.

In the physical optics approximation, the response is polarization independent. When the effect of correction currents is included in the analysis, it is seen that the difference in the responses at polarizations in two directions is related to the difference in the surface curvatures in two directions. This fact permits treatment of a more general class of targets provided that the relationship between local curvature and overall surface contour is known. In this report it is assumed that the surface is convex and rotationally symmetric and that the angle of incidence with respect to the axis of rotation is known. In addition symmetry about a plane perpendicular to the axis of rotational symmetry is assumed. It is believed that the removal of these (or equivalent) symmetry conditions from the general inverse scattering problem requires observation at several directions. A sketch of this target class appears in Fig. 32.

While the theoretical development which follows is valid for the class of targets described above, the numerical implementation of the technique was limited to broadside incidence (i.e., perpendicular to the axis of symmetry). The test cases were a sphere, a prolate spheroid and a cylinder.

5.2 DERIVATION OF INVERSE SCATTERING EQUATIONS

We write the far-field response in terms of the time-retarded surface currents:

$$\vec{r}_o \vec{H}(\vec{r}_o, t_f) = \frac{1}{4\pi} \frac{\partial}{\partial t} \int_S \vec{J}(\vec{r}, t) \times \hat{a}_{r_o} dS, \quad (30)$$

where

\hat{a}_{r_o} is the direction of observation,

$$t = t_f + \hat{a}_{r_o} \cdot \vec{r},$$

\vec{r} is a point on the surface S.

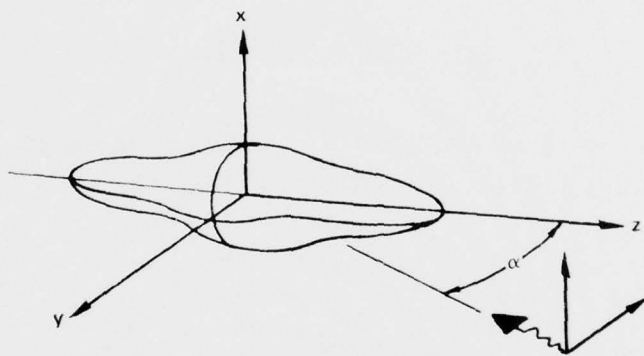


FIG. 32 Inverse scattering of rotationally symmetric surface.

The time origins are chosen such that an impulse from the origin at $t=0$ arrives in the far field at $t_f=0$. The units of time are light-meters. We will divide the surface current at a point into two parts, that due to the incident field and the part due to the other surface currents:

$$\vec{J}(\vec{r}, t) = \vec{J}_{Po}(\vec{r}, t) + \vec{J}_c(\vec{r}, t) \quad (31)$$

where

$$\vec{J}_{Po}(\vec{r}, t) = 2\hat{a}_n \times \vec{H}^{inc}(\vec{r}, t) \quad (32)$$

the part due to the incident field, is identical to the surface current in the zero order physical optics approximation; and

$$\vec{J}_c(\vec{r}, t) = \frac{1}{2\pi} \int_S \hat{a}_n \times [\mathcal{L} \vec{J}(\vec{r}', \tau) \times \hat{a}_R] dS \quad (33)$$

is called the "correction current". Here,

$$\mathcal{L} \text{ is the operator } \frac{1}{R^2} + \frac{1}{R} \frac{\partial}{\partial \tau},$$

\vec{r}' is a point on the surface,

$$R = |\vec{r} - \vec{r}'|,$$

$$\hat{a}_R = (\vec{r} - \vec{r}')/R,$$

$$\tau = t - R,$$

\hat{a}_n is the surface normal at \vec{r} .

The incident field is assumed to be a ramp arriving at the origin at $t=0$:

$$\begin{aligned} \vec{H}^{\text{inc}}(\vec{r}, t) &= \hat{a}_H(t + \hat{a}_{r_0} \cdot \vec{r}), \text{ for } (t + \hat{a}_{r_0} \cdot \vec{r}) \geq 0 \\ &= 0, \text{ for } (t + \hat{a}_{r_0} \cdot \vec{r}) < 0 \end{aligned} \quad (34)$$

The solution of these equations will proceed in the usual method of stepping along in time. Accordingly we divide S (the surface illuminated at the retarded time t corresponding to far field time t_f) into a part which is presumed known from determination at an earlier instance of t_f and the new part ΔS , which is unknown and which is just illuminated by the beginning of the incident ramp. Hence, we rewrite Eq. (30) as

$$\vec{H}(\vec{r}_0, t_f) = \frac{1}{4\pi} \frac{\partial}{\partial t} \int_{\Delta S} \vec{J}(\vec{r}, t) \times \hat{a}_{r_0} dS + \frac{1}{4\pi} \frac{\partial}{\partial t} \int_{S-\Delta S} \vec{J}(\vec{r}, t) \times \hat{a}_{r_0} dS \quad (35)$$

Since the incident ramp has just passed over the new area ΔS there are no contributions from ΔS to the surface currents $\vec{J}(\vec{r}, t)$ for \vec{r} in $(S-\Delta S)$; i.e., the integral in Eq. (33) is also over the known area $(S-\Delta S)$. Similarly, at a point \vec{r} in ΔS , there can be no contribution to $\vec{J}(\vec{r}, t)$ due to surface current in $(S-\Delta S)$. The two integrals in Eq. (35) are thus completely separated.

Consider first the integral over the known region. To evaluate this, the surface current \vec{J} must be computed. The integral Eq. (33) contains \vec{r} as an integration point. It is necessary to separate out the effect of the local region S_ϵ about \vec{r} in order to obtain $\vec{J}(\vec{r}, t)$ explicitly in terms of the incident field and the retarded currents elsewhere on the surface. Analytically S_ϵ can be considered to be an infinitesimal patch about \vec{r} , while in the numerical solution S_ϵ is the surface patch with center \vec{r} of the numerical representation of the target. The integration over S_ϵ is performed in Appendix 8.3 and gives rise to a "self patch correction factor", γ which is dependent upon polarization, patch curvature and patch size. In accordance with the result of Appendix 8.3 we reformulate expressions (31)-(33) as

$$\vec{J}(\vec{r}, t) = \vec{J}_{\text{POL}}(\vec{r}, t) + \vec{J}_c(\vec{r}, t) \quad (36)$$

where

$$\vec{J}_{\text{POL}}(\vec{r}, t) = \frac{i}{\gamma} (2\hat{a}_n \times \vec{H}^{\text{inc}}(\vec{r}, t)) \quad (37)$$

is the first order physical optics current and includes the effect of the self-patch; and where

$$\vec{J}_c(\vec{r}, t) = \frac{1}{2\pi\gamma} \int_{S-S_c} \hat{a}_n \times [\oint \vec{J}(\vec{r}', \tau) \times \hat{a}_R] dS \quad (38)$$

is the correction current due to the remainder of the surface. Note that \vec{J} in this integral in turn consists of the sum of the retarded first order physical optics currents and the correction currents at the integration point \vec{r}' , as in Eq. (35). In the numerical solution we need only store \vec{J}_c at all points (\vec{r}', τ) and compute the contribution due to $\vec{J}_{\text{POL}}(\vec{r}', \tau)$ directly when integrating Eq. (38). Also, as will be indicated later, the quantity of interest is actually $\partial \vec{J}_c(\vec{r}, t) / \partial t$. Differentiating Eq. (38) and integrating numerically over the discrete patches, we can take the derivative inside the integral for these patches which are fully covered by the incident field, while we need special treatment for the patches which are only partially excited by the incident field and for which $\partial S / \partial t$ is non-zero. Anticipating the results of the next subsection we will approximate this effect by substituting an effective area for the nominal patch area.

For an incident ramp we have simply:

$$\frac{\partial}{\partial t} \oint \vec{H}^{\text{inc}}(\vec{r}', \tau) = \frac{1}{2} \hat{a}_H$$

for $(\tau + \hat{a}_{r_0} \cdot \hat{r}') > 0$ and zero otherwise. We thus write numerically:

$$\frac{\partial \vec{J}_c(\vec{r}, t)}{\partial t} = \frac{1}{2\pi\gamma} \left[\hat{a}_n \times \sum_{\text{non-self } \ell} \left[\frac{\hat{a}_H}{2} + \oint \frac{\partial \vec{J}_c(\vec{r}_\ell, \tau)}{\partial t} \right] \times \hat{a}_{R_\ell} \frac{\Delta S_\ell}{\gamma_\ell} \right] \quad (39)$$

Where the summation is over all patches l except the self-patch and where ΔS_l is understood to be an effective area for partially excited patches. This is the expression that is coded in the computer program. The process of evaluating this expression will be referred to later as the process of "updating the correction currents". Note that \vec{J}_c at time t is given in terms of the \vec{J}_c at other points at previously calculated time point $\tau = t - R$.

We are now in a position to compute the second integral of Eq. (35) to obtain the contribution of the known area $(S - \Delta S)$ to the far field. As was done above, we take $\partial/\partial t$ inside the integral, keeping in mind the difficulty of partially excited patches. Substituting Eq. (36) into the second integral of Eq. (35) we write:

$$II_{(S-\Delta S)} = r_o \vec{H}_{PO1}(\vec{r}_o, t_f) + r_o \vec{H}_c(\vec{r}_o, t_f),$$

where

$$r_o \vec{H}_{PO1}(\vec{r}_o, t_f) = \frac{1}{4\pi} \sum_j \frac{2}{\gamma_j} (\hat{a}_{nj} \times \frac{\partial}{\partial t} \vec{J}_{PO}(\vec{r}, t)) \times \hat{a}_{r_o} \Delta S_j,$$

or, making use of Eq. (5) and expanding the vector triple product:

$$r_o \vec{H}_{PO1}(\vec{r}_o, t_f) = \frac{\hat{a}_H}{2\pi} \sum_j \frac{1}{\gamma_j} (\hat{a}_{nj} \cdot \hat{a}_{r_o}) \Delta S_j,$$

where summation is over all patches with \vec{r}_j in $(S - \Delta S)$. We recognize this as the projected area function of the physical optics approximation, modified by the individual self-patch correction factors, γ_j . (We also remember that ΔS_j is an effective area for partially excited patches.) The other part of II is written as

$$r_o \vec{H}_c(\vec{r}_o, t_f) = \frac{1}{4\pi} \int_{S-\Delta S} \frac{\partial \vec{J}_c}{\partial t}(\vec{r}, t) \times \hat{a}_{r_o} ds \quad (40)$$

This is also evaluated numerically by summing over all patches with \vec{r}_j in

(S- Δ S). (In this integral we need not worry about partially excited patches, since the correction currents are still zero at that time, so that such patches can simply be omitted.)

We return now to the first integral of Eq. (35) over the new region Δ S. We note that $\vec{J}(\vec{r}, t)$ in this integral consists only of the term \vec{J}_{POL} since the incident field has just passed over each patch in this region so that there are no contributions from the surface currents at other patches. We can thus write the first order physical optics contribution of the new region entirely in terms of known quantities by rewriting Eq. (35).

$$I(\vec{r}_o, t_f) \equiv \frac{1}{4\pi} \frac{\partial}{\partial t} \int_{\Delta S} \vec{J}_{\text{POL}}(\vec{r}, t) \times \hat{a}_{r_o} dS = r_o \vec{H}(\vec{r}_o, t_f) - r_o \vec{H}_{\text{POL}} - r_o \vec{H}_c, \quad (41)$$

where $r_o \vec{H}$ is the known ramp response of the surface and where $r_o \vec{H}_{\text{POL}}$ and $r_o \vec{H}_c$ are the contributions to the far field due to the known region (S- Δ S). The left-hand side of Eq. (41) can be integrated directly, as shown in the next subsection. Since the self-term correction factor (as it appears in Eq. 37) is dependent upon the surface geometry and the polarization, we can obtain the geometry characteristics by comparison of the responses at the two polarizations.

We can see now how the inversion process would proceed:

1. For the specular point the right-hand side of Eq. (41) is simply the leading edge of the ramp response, hence solution of the integral will yield the geometric properties of the region surrounding the specular point.
2. Knowing the region (S- Δ S), update the correction currents \vec{J}_c up to the retarded time corresponding to the new far field time t_f ; compute \vec{J}_c and \vec{J}_{POL} at the retarded time and their contributions \vec{H}_c and \vec{H}_{POL} to the far field.
3. Subtract these contributions from the known ramp response. Do this for both polarizations.
4. From the remaining contributions to the far field deduce the geometric properties of the new region Δ S.

5. The entire surface S is now known. Step to a later time t_f and repeat for a new region ΔS .

It remains to relate the characteristics of the surface to the leading edge of its first order ramp response.

5.3 FIRST ORDER RAMP RESPONSE OF CURVILINEAR PATCH

We want to reformulate the following integral, which represents the known contribution to the far field of the new unknown region ΔS :

$$I(\vec{r}_o, t_f) = \frac{1}{4\pi} \frac{\partial}{\partial t} \int_{\Delta S} \vec{J}_{POL}(\vec{r}, t) \times \hat{a}_{r_o} dS, \quad (42)$$

where ΔS is a region of as yet unknown geometry and where t_f is such that ΔS is just covered by the incident field at the corresponding retarded times $t = t_f + \hat{a}_{r_o} \cdot \vec{r}$. This is illustrated in Figure 33. We need to find an expression for this integral in terms of the geometric properties of ΔS .

By the result of Appendix 8.3 we have that

$$\vec{J}(\vec{r}, t) = \vec{J}_{POL}(\vec{r}, t) = \frac{1}{\gamma} (2\hat{a}_n \times \vec{H}^{inc}(\vec{r}, t)) \equiv \frac{1}{\gamma} \vec{J}^{inc}(\vec{r}, t).$$

To determine γ it is necessary to write \vec{J} explicitly in its u, v components (see Appendix 8.3):

$$J_u(\vec{r}, t) = \frac{J_u^{inc}(\vec{r}, t)}{1 - \zeta}, \quad J_v(\vec{r}, t) = \frac{J_v^{inc}(\vec{r}, t)}{1 + \zeta}, \quad (43)$$

$$\text{where} \quad \zeta = \frac{K_u - K_v}{4} \cdot R_o, \quad \text{and where} \quad (44)$$

R_o is the radius of the self-patch. The critical point here is that the value of R_o is proportional to the value of the incident ramp at (\vec{r}, t) . We see this as follows: The magnitude of \vec{J}^{inc} at (\vec{r}, t) is given by Eq. 34. $J^{inc}(\vec{r}, t) = (\hat{a}_{r_o} \cdot \vec{r}) + t$, while the magnitude at an integration point of the

self-patch is the retarded excitation:

$$J^{\text{inc}}(\vec{r}', \tau) = (\hat{a}_{r_0} \cdot \vec{r}') + \tau$$

or, using the usual definitions $\vec{R} = \vec{r} - \vec{r}'$, $\tau = t - R$:

$$J^{\text{inc}}(\vec{r}', \tau) = J^{\text{inc}}(\vec{r}, t) - R - (\hat{a}_{r_0} \cdot \vec{R}).$$

Note that if the curved patch is perpendicular to \hat{a}_{r_0} , the dot product term is small in comparison to R . On the other hand, if the patch is nearly tangent to \hat{a}_{r_0} , $(\hat{a}_{r_0} \cdot \vec{R}) \sim \pm R$. If we average the effects of 2 points on opposite sides of \vec{r}_0 , we can thus simplify the above as

$$J^{\text{inc}}(\vec{r}', \tau) = J^{\text{inc}}(\vec{r}, t) - R. \quad (45)$$

This is greater than zero for $R < J^{\text{inc}}(\vec{r}, t)$, hence the radius of the self-patch is

$$R_0 = J^{\text{inc}}(\vec{r}, t).$$

This is illustrated in Fig. 34: The self-patch that contributes to the surface current at (\vec{r}, t) for the leading edge of the incident ramp is only a small region about \vec{r} . We consider now two directions of polarization of \vec{H}^{inc} :

$$\hat{a}_x \text{ and } \hat{a}_p, \text{ where } \hat{a}_p = \hat{a}_x \times \hat{a}_{r_0}$$

(\hat{a}_p and \hat{a}_{r_0} are in the yz plane). In Appendix 3.4 it is shown that if we transform \vec{J} from the u, v coordinate system of Eqs. (43) to the x, p coordinate system and form the cross product required in Eq. (42), we can write

$$\vec{J}(\vec{r}, t) \times \hat{a}_{r_0} = 2(\hat{a}_n \cdot \hat{a}_{r_0}) \left(\frac{H_p^{\text{inc}}(\vec{r}, t) \hat{a}_p}{1 + \zeta} + \frac{H_x^{\text{inc}}(\vec{r}, t) \hat{a}_x}{1 - \zeta} \right) \quad (46)$$

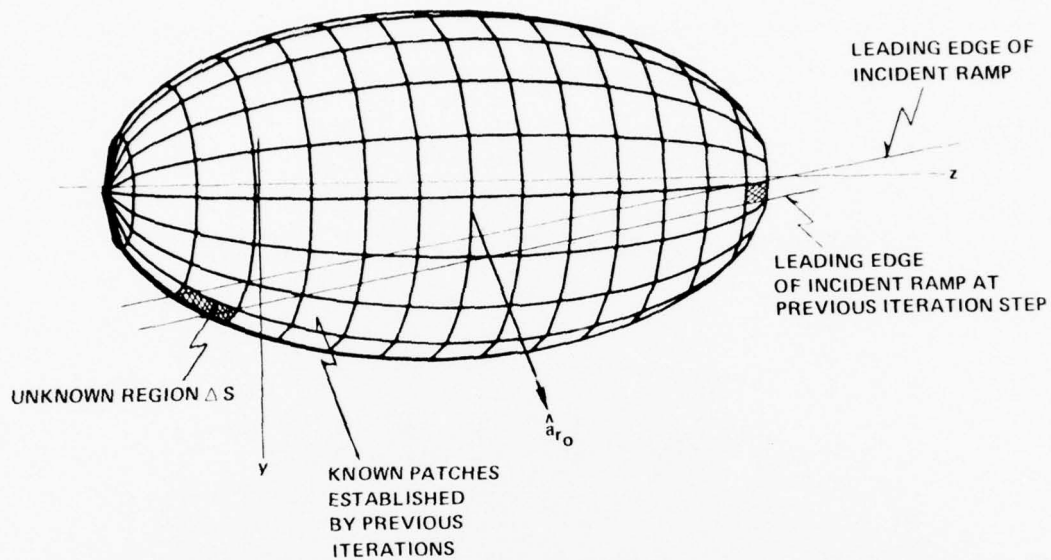


FIG. 33 Unknown region ΔS for body with rotational symmetry.

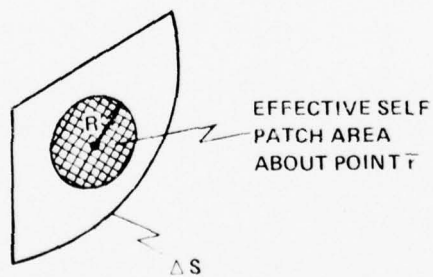


FIG. 34 Self-patch integration at point inside ΔS .

Here certain cross-terms are neglected, which cancel when the above is integrated over a surface with plane symmetry about the yz plane (as is the case for our bodies of revolution).

Let us concentrate on the \hat{a}_p component, and substitute Eq. (46) and the value of H^{inc} in the expression for the far field contribution (using $t = t_f + \hat{a}_{r_o} \cdot \vec{r}$):

$$I_p(r_o, t_f) = \frac{1}{2\pi} \frac{\partial}{\partial t} \int_{\Delta S} \frac{t_f + 2(\hat{a}_{r_o} \cdot \vec{r})}{(1 + \zeta)} (\hat{a}_n \cdot \hat{a}_{r_o}) dS$$

or

$$I_p(r_o, t_f) = \frac{1}{2\pi} \frac{\partial}{\partial t} \int_{\Delta S} \frac{t'}{(1 + \zeta)} dS_{proj}. \quad (47)$$

Here we have written $dS_{proj} = (\hat{a}_n \cdot \hat{a}_{r_o}) dS$, the projected area and $t' = t_f + 2(\hat{a}_{r_o} \cdot \vec{r})$. Note that $t' = 0$ at the far edge of ΔS where the leading edge of the ramp has just arrived and is >0 in the rest of ΔS . Also note that

$$\zeta = \frac{(K_u - K_v)}{4} \cdot t'.$$

Since the contribution to the integral at the edge goes to zero, we neglect the effect of time variation of the integration limits and take the time derivative inside the integral:

$$I_p(r_o, t_f) = \frac{1}{2\pi} \int_{\Delta S} \frac{dS_{proj}}{(1 + \zeta)^2} \quad (48)$$

This integral can be performed over t' , by writing dS_{proj} in terms of t' .

The limits of t' are $t' = 0$, corresponding to the far edge of ΔS , and $t' = \Delta t = 2\Delta(\hat{a}_{r_o} \cdot \vec{r})$, corresponding to the near edge of ΔS (which is the

edge of the known region). Expand ds_{proj} from a point, e , on the near edge:

$$\frac{ds_{\text{proj}}}{dt} = \left(\frac{ds_{\text{proj}}}{dt} \right)_e (\Delta t - t') + \left(\frac{d^2 s_{\text{proj}}}{dt^2} \right)_e (\Delta t - t')^2 + \dots$$

and expand

$$\frac{1}{(1 + \zeta)^2} = 1 - 2\zeta + 3\zeta^2$$

Integrating and retaining only second order terms

$$2\pi I_p = \left(\frac{ds_{\text{proj}}}{dt} \right)_e \Delta t + \left(\frac{d^2 s_{\text{proj}}}{dt^2} \right)_e \frac{\Delta t^2}{2} - \frac{(K_u - K_v)}{2} \left(\frac{ds_{\text{proj}}}{dt} \right)_e \frac{\Delta t^2}{2} \quad (49)$$

Similarly, for the other polarization, we obtain

$$2\pi I_x = \left(\frac{ds_{\text{proj}}}{dt} \right)_e \Delta t + \left(\frac{d^2 s_{\text{proj}}}{dt^2} \right)_e \frac{\Delta t^2}{2} + \frac{(K_u - K_v)}{2} \left(\frac{ds_{\text{proj}}}{dt} \right)_e \frac{\Delta t^2}{2} \quad (50)$$

The first two terms of these are the projected area of the new region ΔS , i.e.

$$\frac{\Delta S_{\text{proj}}}{2\pi} = \frac{I_x + I_p}{2}, \quad (51)$$

which is the polarization-independent physical optics term. Also, approximately, subtract Eqs. (49) and (50) obtaining

$$K_u - K_v = \left(\frac{I_x - I_p}{I_x + I_p} \cdot \frac{4}{\Delta t} \right) \quad (52)$$

To obtain K_u, K_v we need another relationship. At the specular point we can use the fact that (see Appendix 8.2)

$$\frac{ds_{\text{proj}}}{dt} = \frac{\pi}{\sqrt{K_u K_v}}$$

resulting in a quadratic equation in K_u or K_v when combined with Eq. (52).

On the preceding page, it is assumed that $K_u K_v \neq 0$. In Appendix 8.6 the case of a specular return from a cylindrical surface is described. At a non-specular point, we make use of our assumption that S is a surface of revolution about the z -axis. In Appendix 8.2 it is shown that

$$K_v = - \frac{1}{\rho \sqrt{1 + \left(\frac{d\rho}{dz}\right)^2}} \quad (54)$$

We know now the projected area of the new region, from Eq. (41), and we know its depth from our choice of t_f . Using the expression given in Appendix 8.5 relating the projected area of a section of a body of revolution to its dimensions we can solve for the ρ, z coordinates of the new region for the orientation $d\rho/dz$, and hence for K_u and K_v . (We can also find $d^2\rho/dz^2$ from the relation

$$K_u = - \frac{d^2\rho/dz^2}{\left(1 + \left(\frac{d\rho}{dz}\right)^2\right)^{3/2}}, \quad (55)$$

which is useful for the initial estimate of the location of the next unknown region.)

The new region is thus completely specified by this analysis. Some comments are required here indicating the assumptions made in this process: the new region consists of two parts, one to each side of the known region. Only for broadside or axial incidence will these two regions have the same geometric properties. For general oblique incidence, or for a body without the left-right symmetry assumed here, it would be required to use a somewhat more complicated process of curve fitting to find the best extension of the contour in each direction consistent with the calculated average values of the surface properties. Such a process appears to be a natural extension of the methods presented here, although it has not been implemented.

5.4 NUMERICAL SOLUTION PROCEDURE

By way of summary, we outline here the step by step inversion procedure, as implemented in the computer program INVR.

1. Input of the ramp responses $H_x(t)$ and $H_y(t)$. These are obtained from the space-time x integral^P equation solutions, as described elsewhere [4], augmented by the ideal specular response at $t=0$ (see Appendix 8.6), and given numerically at regular intervals of t .

2. Analysis of Specular Return

Equations (41) through (45) are applied at the leading edge of the response in the limit as $\Delta t \rightarrow 0$ (i.e. we actually calculate the derivatives of the responses), to establish the curvatures at the specular point. The accuracy of this process is limited by the fineness with which the ramp response is specified. On the assumption that the target is a body of revolution, and knowing the angle of incidence, we can establish bands along the radius of revolution through this point. This is our first known region.

3. Extrapolate from the known region by a small distance Δl to each side to obtain the approximate center of the next bands. The part of these bands that will be illuminated in accordance with step (4) is our new region ΔS .
4. Choose the far field time, t_f , such that the leading edge of the incident ramp just reaches the far edge in the y - z plane of the new region ΔS at the retarded time

$$t = t_f + \hat{a}_{r_0} \cdot \hat{r}_{\text{edge}}.$$

5. Update the surface correction currents at all points, i , in the known region up to their respective retarded times

$$t_i = t_f + \hat{a}_{r_0} \cdot \hat{r}_i, \text{ using Eq. (39).}$$

6. Calculate the contributions of the known region to the far field at time t_f (for each polarization) using Eqs. (39) and (40). Subtract these from the known responses; the remainder is due to the new region.
7. Apply the expressions (41), (42), (44) and the result of Appendix 8.5, to characterize the geometry of the new region.

Establish patches along the radius of rotation, which passes through the center of the new region. We have now extended our known region and continue from point (3) until the entire surface is covered. (For a body of revolution it is only necessary to pass halfway over the target.)

At point (2), the analysis of the specular return, the determination is made of the nature of the specular surface. That is, whether one or both of the curvatures are zero (See Appendix 8.6). In the case of the sphere-capped cylinder viewed on broadside, for example one of the curvatures is zero, and the initial known region is the entire cylinder body.

The core of the process, point (5), the updating of the surface currents is similar to the usual space-time integral equation scattering solution [4,5]; except that here the time-derivative of the correction currents are calculated rather than the usual total surface current. Also, the correction currents are calculated at the exact retarded time corresponding to the far field time under consideration, in addition to the calculations at the regular time grid. The patch interaction of the correction currents (Eq. 39) are calculated at the retarded times τ by interpolation on the time grid, whereas the effects of the incident field are calculated exactly.

5.5 INVERSE SCATTERING RESULTS

We present here the results of exercising the computer program INVRS on the test cases of a sphere, a prolate spheroid and a sphere-capped cylinder, all viewed at broadside.

A quadrant of the cross-section of a sphere is compared with the result from the inverse scattering calculation in Fig. 35. The arrow indicates the direction of incidence. Crosses indicate the sample points of the calculated contour. The agreement is very good up to the last point calculated near the axis of symmetry. At this point, the projected area of the new region is much smaller than its surface area; hence a small error in the calculation of the correction currents leads to a larger error in the surface contour. A perspective drawing is given in Fig. 36.

AD-A044 801

SPERRY RESEARCH CENTER SUDBURY MASS
IMPULSE RESPONSE TARGET STUDY.(U)

F/G 17/9

SEP 77 C L BENNETT, R HIERONYMUS, H MIERAS

F30602-76-C-0209

UNCLASSIFIED

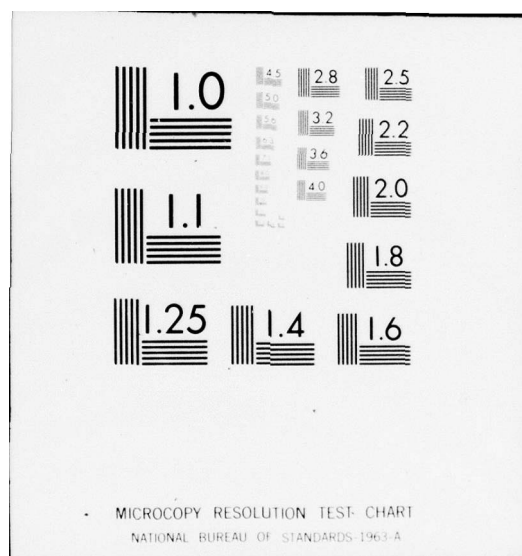
RADC-TR-77-273

NL

2 of 2
ADA044801



END
DATE
FILMED
10-77
DDC



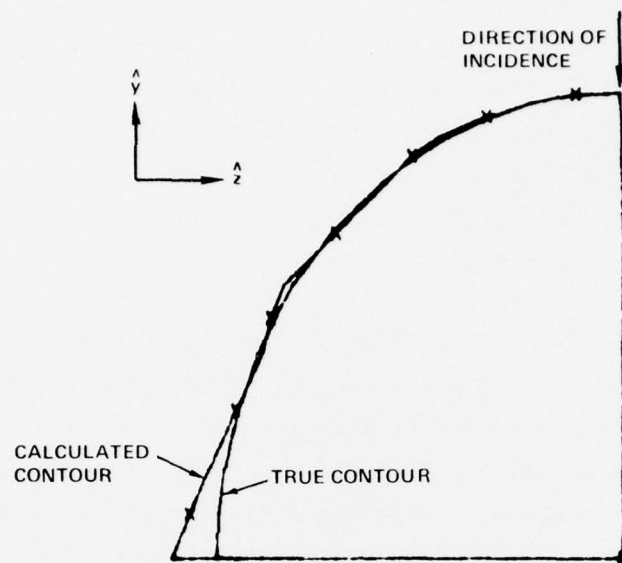


FIG. 35 Inverse scattering results — cross-section of sphere quadrant.

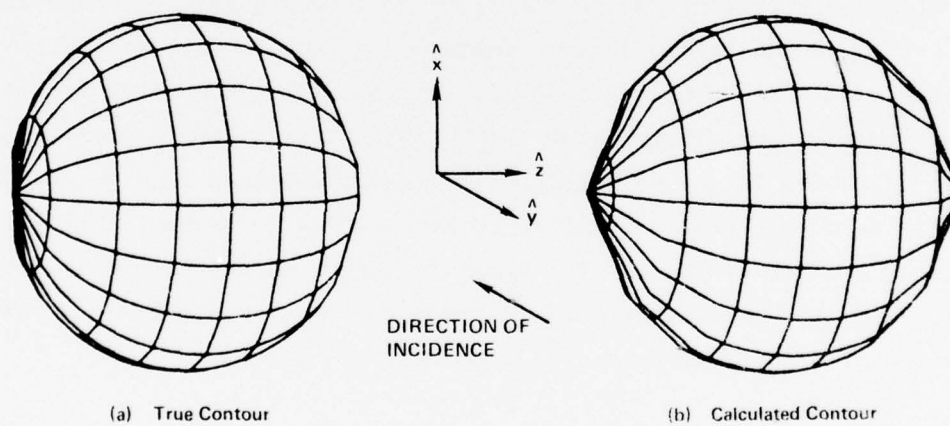


FIG. 36 Inverse scattering results — sphere.

A similar set of drawings is presented in Figs. 37 and 38 for a prolate spheroid of 2:1 axis ratio with its major axis along the axis of rotation. The contour agreement for this case is very good, although there is a 5% overestimate of the size. This small error is due to inaccuracies in the specular point analysis, caused by coarseness in the numerical representation of the ramp response.

The results for the sphere-capped cylinder are represented in Figs. 39 and 40. The cylinder length was 3 times its diameter. The results of this case were less satisfactory than for the other test cases. There are several problems in the analysis of this case: The analysis of the specular point (as described in Appendix 8.6) requires separating the part of the response due to the cylinder (which has a dependence of half-integral powers of time) from the response due to the smoothly curved cap (which has a dependence of integral powers of time). The numerical representation of the ramp response available was too coarse to permit an accurate analysis of this type. Instead, reasonable values for the dimensions of the cylinder as might be expected from the analysis of more accurate response data, were utilized in the solution. The remainder of the contour generation is reasonably good until the region closest to the axis of symmetry is reached. Here we have the same effect noted for the case of the sphere, namely that small inaccuracies in the calculation of the correction currents can produce large errors in that part of the contour which is nearly parallel to the direction of observation. The error is larger in the case of the cylinder than for the sphere, because of the much larger surface area over which the surface current error is accumulated.

In summary: It has been demonstrated that inverse scattering of rotationally symmetric bodies using the space-time integral equation approach yields reasonably accurate results for oblique incidence. Accurate specular analysis requires the representation of the response at intervals of $\Delta t = .05 \cdot R$, where R is the body radius ($\Delta t = 0.2 \cdot R$ was available for these test cases). Inaccuracies in the surface correction currents can probably be improved by greater attention to the details of surface excitation at

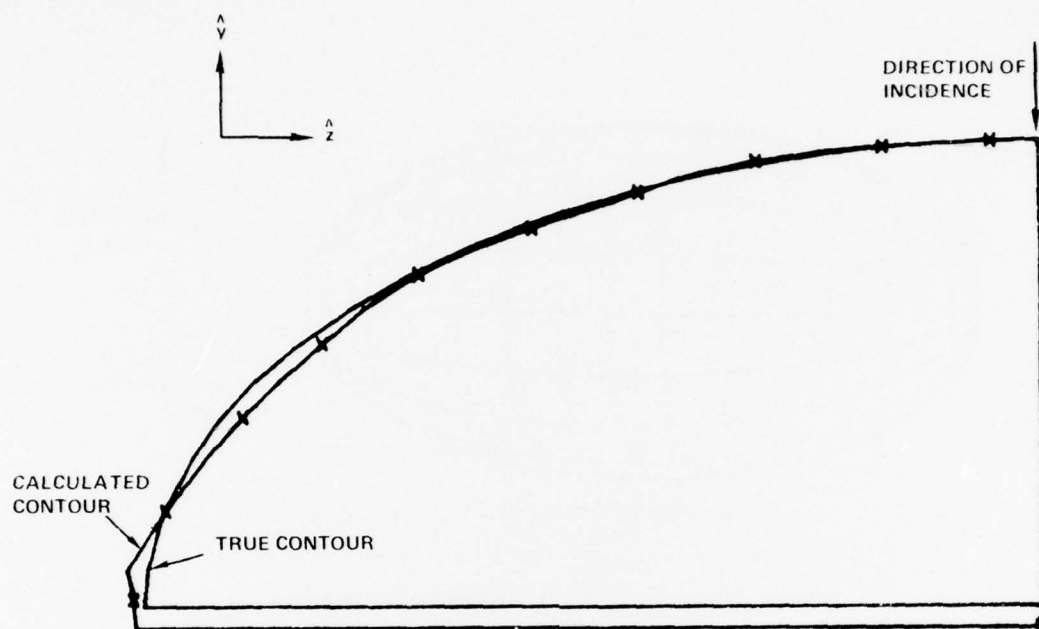


FIG. 37 Inverse scattering results — cross-section of prolate spheroid.

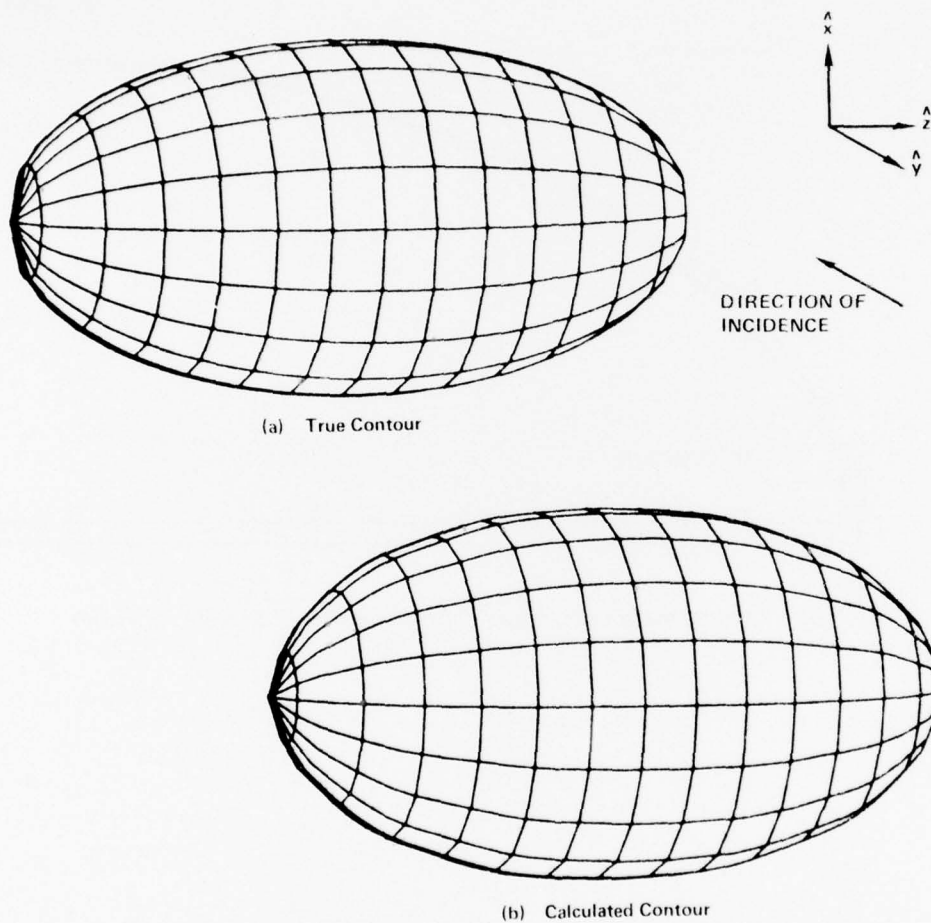


FIG. 38 Inverse scattering results — prolate spheroid.

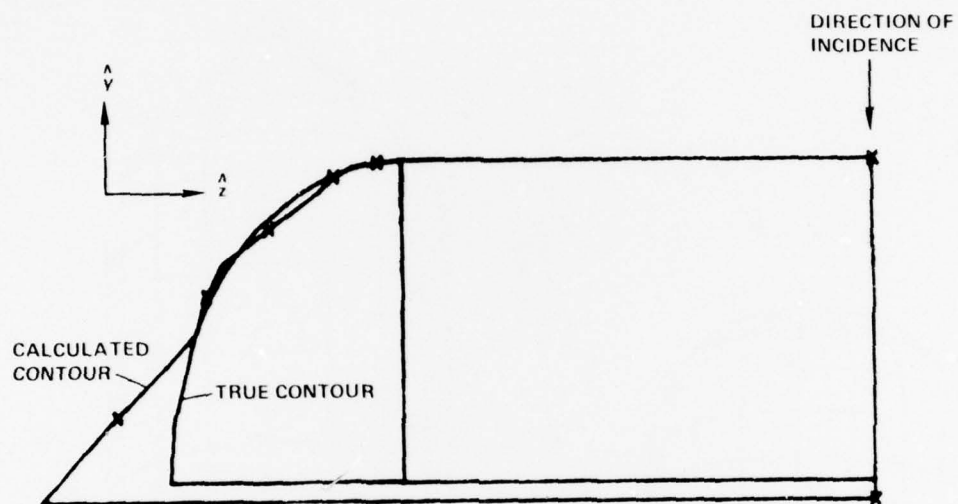


FIG. 39 Inverse scattering results — cross-section of sphere-capped cylinder.

the instant of the ramp initial incidence as was done for the case of axial incidence in Section 4. Also, although the test cases were for broadside incidence, it has been indicated in the body of the report that the method can be extended to arbitrary, but known, angle of incidence on surfaces of rotation.

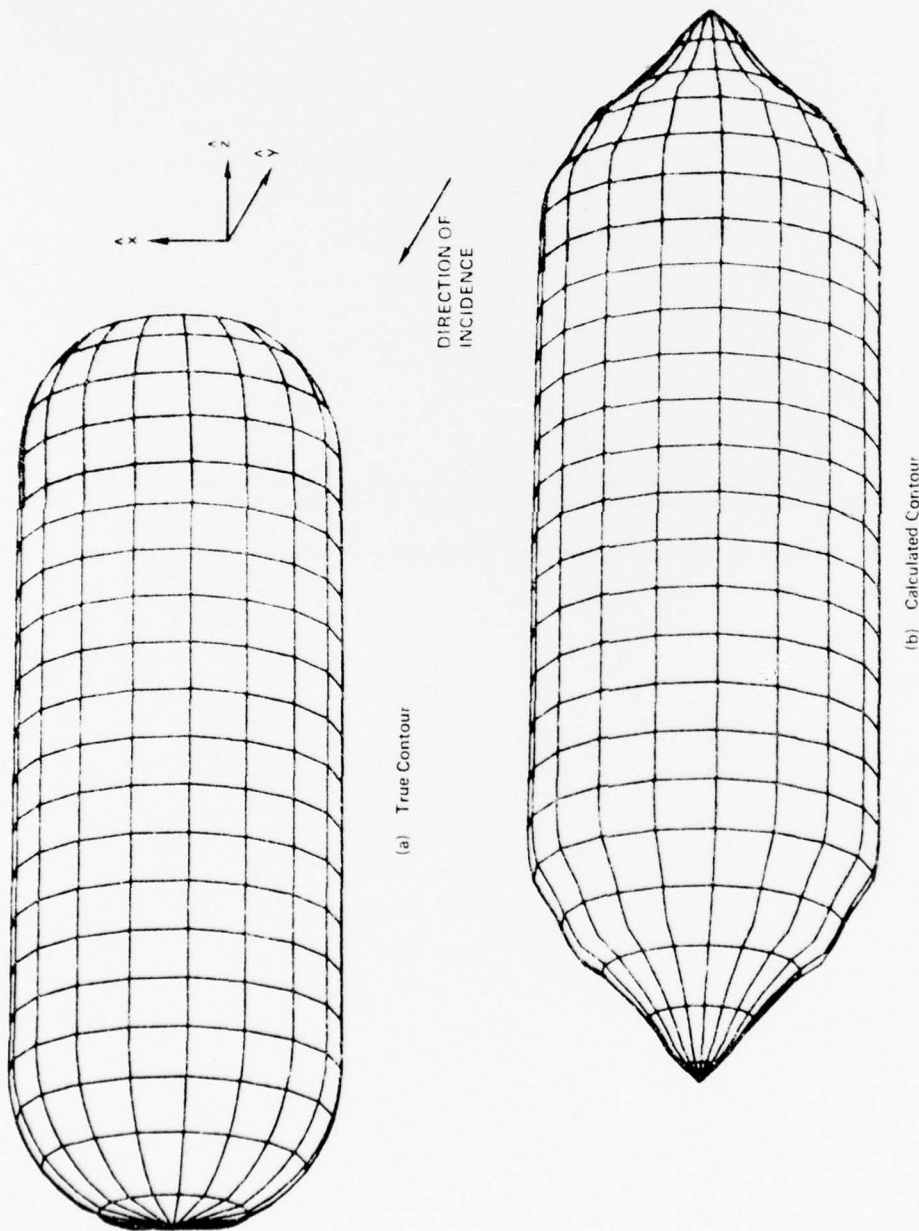


FIG. 40 Inverse scattering results — sphere-capped cylinder.

SECTION 6

SUMMARY AND CONCLUSIONS

In this study the technique for computing the smoothed impulse response has been extended to the case of scattering from simple aircraft models. These models consist of a cylindrical fuselage and rectangular plate wings, stabilizers, and rudder. To the knowledge of these writers this is the first time that a successful solution for this problem has been reported. Secondly, direct time domain techniques have been developed for the solution of the inverse scattering problem involving rotationally symmetric targets. Both the case of axial incidence and the case of oblique incidence were considered. The use of polarization information enabled the development of a solution for the case of oblique incidence. Finally, techniques for computing the impulse response have been developed for the case of cylinders with fins attached with non-axial incidence. The foundation of these techniques is the space-time integral equation approach to the solution of the electromagnetic scattering problem. This coupled with the impulse response augmentation technique, is used to yield the total impulse response or the frequency response over the entire spectrum. This, in turn, can be used to compute the response of a target due to any incident radar waveform, regardless of wave shape or carrier frequency.

Numerical procedures were developed for the solution of a space-time integral equation for computing the smoothed impulse response of simple aircraft models consisting of a cylindrical fuselage with rectangular plate wings, stabilizers, and rudder. These procedures were extensions of previously developed techniques for computing the smoothed impulse response of a cylinder with single fins attached. They consist of the simultaneous solution of two space-time integral equations for the surface current. One, an H-field type equation, is for the cylindrical fuselage surface current and it includes the effect of currents on the fuselage and currents on the wings, stabilizer, and rudder. The second equation, an E-field type equation, is for the current on the wings, stabilizer, and rudder and it includes the effect of both the wing, stabilizer and rudder currents and the

fuselage currents. Finally, at the boundary between the fins and the fuselage the physical boundary conditions are applied to specify the current in that region. This technique was verified by direct time domain calculations for a number of simple cases and found to be in good agreement. The technique was demonstrated on an aircraft model that consisted of a cylindrical fuselage with rectangular fins representing wings, stabilizers and rudder. These results are particularly encouraging and the techniques developed here should be extended to more refined aircraft models. These more refined models could consist of smooth fuselage representations which more closely approximate the real aircraft. In addition the wings, stabilizers, and rudders could be represented by quadrilateral flat plates instead of the now limiting rectangular flat plate geometries.

The impulse response augmentation technique was successfully extended to the case of scattering from a cylinder with a single pair of fins attached for oblique incidence. The augmentation functions for this target were based on the results previously obtained for the cases of square plates and right circular cylinders. By using a combination of these two sets of augmentation functions the necessary augmentation function for the case of a cylinder with fins attached was obtained. Results were computed for a cylinder with a length to diameter ratio of 2:1 and with one set of square fins whose size was equal to the cylinder diameter attached. These results were obtained for aspect angles of 0° , 30° , 60° , 90° , 120° , 150° , and 180° . The resulting impulse responses clearly show the singular contributions from the various scattering centers on this more complex target. The companion frequency responses display ripples that correspond to the interference between the returns from these different scattering centers. The results of this technique continue to be encouraging and should be extended to more complex targets and to non-rectangular fin plate targets.

A time domain approach to the inverse scattering problem was developed and demonstrated in this study. This approach starts with a space time integral equation that represents the inversion process. Previously, an iterative technique was developed for the solution of this inversion equation and applied to four target geometry cases. In this effort a direct

time domain solution technique was developed for the solution of this inversion equation and applied to the same four targets that were examined previously. Results were obtained for the case of axial incidence for a sphere, sphere-cap cylinder, and a flat-end sphere-cap cylinder. The direct solution technique results compared well with those obtained using the iterative solution technique and were in close agreement to the actual target geometries. However, the major advantage of the direct solution technique is that it requires substantially less computer time to obtain the solution. In addition to the case of axial incidence, the case of oblique incidence was also considered for the inverse problem. In the case of oblique incidence the direct time domain techniques were developed for the solution of the inverse scattering problem using polarization information together with the target's ramp response. As an example of these techniques, the case of broadside incidence on three targets was considered. The results were obtained for the case of a sphere, a sphere-cap cylinder, and a prolate spheroid. These results yielded a geometry estimate which was in close agreement with the actual geometry except at the ends of the targets. It was found that this technique requires only a single observation angle for the case of broadside incidence.

SECTION 7
REFERENCES

1. H. Mieras, "Improvements in Four Computer Programs for the Space-Time Integral Equation Solution of Scattering Problems," Sperry Research Center, Sudbury, Mass., Interim Report on Contract No. F30602-76-C-0209, January 1977.
2. C.L. Bennett, "A Technique for Computing Approximate Electromagnetic Impulse Response of Conducting Bodies," Ph.D. Dissertation, Purdue University, Lafayette, Indiana, August 1968.
3. C.L. Bennett, J.D. DeLorenzo and A.M. Auckenthaler, "Integral Equation Approach to Wideband Inverse Scattering," Sperry Research Center, Sudbury, Mass., Final RADC-TR-70-177 dated October 1970 (AD 876849).
4. C.L. Bennett, A.M. Auckenthaler, R.S. Smith and J.D. DeLorenzo, "Space-Time Integral Equation Approach to the Large Body Scattering Problem," Sperry Research Center, Sudbury, Mass., Final RADC-TR-73-70 dated May 1973 (AD 763794).
5. C.L. Bennett, K.S. Menger, R. Hieronymus et al, "Space-Time Integral Equation Approach for Targets with Edges," Sperry Research Center, Sudbury, Mass., Final Report on Contract No. F30602-73-C-0214, May 1974.
6. C.L. Bennett, R.M. Hieronymus, and D. Peterson, "Space-Time Integral Equation Approach to Targets with Fins," Sperry Research Center, Sudbury, Mass., Final RADC-TR-76-59 dated March 1976 (AD A023204).
7. J.D. DeLorenzo, Radar Target Identifying Apparatus, Patent No. 3,523,292, August 4, 1970.
8. C.L. Bennett and J.D. DeLorenzo, Short Pulse Response of Radar Targets, 1969 International Antenna and Propagation Symposium, Austin, Texas, 9-11 December 1969.
9. A.M. Nicolson et al, "Applications of Time Domain Metrology to the Automation of Broadband Microwave Measurements," IEEE Trans. Microwave Theory and Techniques MIT-20, 3-9 (January 1972).
10. Armen H. Zenanian, Distribution Theory and Transform Analysis, McGraw Hill, New York, 1965.
11. E.M. Kennaugh and R.L. Cosgriff, "The Use of Impulse Response in Electromagnetic Scattering Problems," 1958 IRE National Convention Record, Part I, pp. 72-77.

12. N.N. Bojarski, "Three-Dimensional Electromagnetic Short Pulse Inverse Scattering," Syracuse University Res. Corp., Syracuse, New York, February 1967.
13. R.M. Lewis, "Physical Optics Inverse Diffraction," IEEE Trans. Antennas and Propagation AP-17, No. 3, May 1969.
14. S.K. Chaudhuri and W.M. Boerner, "A Monostatic Inverse Scattering Model Based on Polarization Utilization," Applied Physics, Springer Verlag, 1976.
15. S.K. Chaudhuri and W.M. Boerner, "Polarization Utilization in Profile Inversion of a Perfectly Conducting Prolate Spheroid," IEEE Trans. on AP, 1976.

SECTION 8

APPENDIX

8.1 IMPROVED SPACE-TIME INTEGRAL EQUATION SOLUTION TECHNIQUE

To implement the solution for the inverse scattering problem described in Section 4, it is necessary to compute the correction currents, J_{CR} , for the surface. These currents represent the effect at a given point on the surface of currents flowing at other surface points. In this computation use is made of the rotational symmetry of the target. This allows for a substantial reduction in the computer time and memory requirements.

The geometry of the rotationally symmetric scattering problem is displayed in Fig. 23. For convenience the polarization of the incident field was taken to be vertical, since the ϕ reference is arbitrary in rotationally symmetric problems. The scatterer surface is defined by the contour

$$\rho = \rho(z)$$

where ρ (the usual cylindrical coordinate) is the distance from the z -axis. The contours, produced in the $y=0$ plane, starts at the most positive point in z and moves along the curve in the negative z -direction. The surface is then generated by rotating the contour about the z -axis. The unit vectors of interest are

\hat{a}_n = the unit vector normal to the surface

\hat{a}_2 = the unit vector tangent to the surface which lies in the plane generated by the z -axis and the position vector r . (This corresponds to \hat{a}_θ in the spherical coordinate system.)

\hat{a}_3 = the unit vector tangent to the surface which is perpendicular to \hat{a}_2 . (This corresponds to \hat{a}_ϕ in the spherical coordinate system.)

It is also convenient to define

$$g = \frac{1}{\sqrt{1 + \left(\frac{d\rho}{dz}\right)^2}}$$

$$g_p = \frac{\left(\frac{d\rho}{dz}\right)}{\sqrt{1 + \left(\frac{d\rho}{dz}\right)^2}}$$

which yield the following relations

$$\hat{a}_2 = -g_p \hat{a}_\rho - g \hat{a}_z$$

$$\hat{a}_3 = \hat{a}_\phi$$

$$\hat{a}_n = g \hat{a}_\rho - g_p \hat{a}_z$$

The expression for the total surface current J , which was derived in Section 4.1, is repeated here for the case of an incident ramp waveform

$$\vec{J}_R(\vec{r}, t) = 2\hat{a}_n \times \vec{H}_R^i(\vec{r}, t) + \vec{J}_{CR}(\vec{r}, t) \quad (56)$$

where

$$\vec{J}_{CR}(\vec{r}, t) = \frac{1}{2\pi} \int_S \hat{a}_n \times \left\{ \frac{1}{R^2} + \frac{1}{R} \frac{\partial}{\partial \tau} \right\} \vec{J}_R(\vec{r}', \tau) \times \hat{a}_R \Big|_{\tau=t-R} dS'$$

$$\tau = t - R$$

By virtue of the rotational symmetry in this problem, the total surface current can also be written as

$$\vec{J}_R(\vec{r}, t) = \hat{a}_2 J_{R_2}(\ell_z, t) \cos \phi + \hat{a}_3 J_{R_3}(\ell_z, t) \sin \phi \quad (57)$$

where ℓ_z is the position coordinate in the \hat{a}_2 direction. Combining these two equations and solving for \vec{J}_{CR} yields the coupled integral equations:

$$\begin{aligned}
J_{CR_2}(\ell_z, t) = & \frac{1}{2\pi} \int_S f_a \left[\frac{1}{R^3} + \frac{1}{R^2} \frac{\partial}{\partial \tau} \right] J_{R_2}(\ell'_z, \tau) dS' \\
& \tau = t - R \\
& + \frac{1}{2\pi} \int_S f_b \left[\frac{1}{R^3} + \frac{1}{R^2} \frac{\partial}{\partial \tau} \right] J_{R_3}(\ell'_z, \tau) dS' \quad (58a) \\
& \tau = t - R
\end{aligned}$$

$$\begin{aligned}
J_{CR_3}(\ell_z, t) = & \frac{1}{2\pi} \int_S f_c \left[\frac{1}{R^3} + \frac{1}{R^2} \frac{\partial}{\partial \tau} \right] J_{R_2}(\ell'_z, \tau) dS' \\
& \tau = t - R \\
& + \frac{1}{2\pi} \int_S f_d \left[\frac{1}{R^3} + \frac{1}{R^2} \frac{\partial}{\partial \tau} \right] J_{R_3}(\ell'_z, \tau) dS' \quad (58b) \\
& \tau = t - R
\end{aligned}$$

where

$$\begin{aligned}
f_a = & - \left[(g'_p \rho' + g'_p (z - z')) \cos \phi' - \rho g' \right] \cos \phi' \\
f_b = & - (z - z') \sin^2 \phi' \\
f_c = & \left[-g'_p g' \rho' + g'_p g \rho - g'_p g'_p (z - z') \right] \sin^2 \phi' \\
f_d = & \left[(g \rho - g'_p (z - z')) \cos \phi' - g \rho' \right] \cos \phi' .
\end{aligned}$$

The initial approach taken for the solution of Eq. (58) was that employed in the direct time domain solution. A grid is structured, as described in Section 4.2, on the portion of the target whose geometry has been determined. The incident field is taken to be a ramp defined by

$$H_R^i(z, t) = \begin{cases} 0 & ; \quad t + z < 0 \\ t + z & ; \quad t + z \geq 0 \end{cases}$$

For the numerical calculations Eq. (58) is represented as

$$\begin{aligned}
 J_{CR_2}(z_i, t) = & + \frac{1}{2\pi} \sum_j \sum_\ell f_{aij\ell} \left\{ \frac{1}{R_{ij\ell}^3} + \frac{1}{R_{ij\ell}^2} \frac{\partial}{\partial \tau} \right\} J_{R_2}(z_j, \tau) \Delta S_\ell \\
 & \tau = t - R_{ij\ell} \\
 & + \frac{1}{2\pi} \sum_j \sum_\ell f_{bij\ell} \left\{ \frac{1}{R_{ij\ell}^3} + \frac{1}{R_{ij\ell}^2} \frac{\partial}{\partial \tau} \right\} J_{R_3}(z_j, \tau) \Delta S_\ell \quad (59a) \\
 & \tau = t - R_{ij\ell}
 \end{aligned}$$

$$\begin{aligned}
 J_{CR_3}(z_i, t) = & + \frac{1}{2\pi} \sum_j \sum_\ell f_{cij\ell} \left\{ \frac{1}{R_{ij\ell}^3} + \frac{1}{R_{ij\ell}^2} \frac{\partial}{\partial \tau} \right\} J_{R_2}(z_j, \tau) \Delta S_\ell \\
 & \tau = t - R_{ij\ell} \\
 & + \frac{1}{2\pi} \sum_j \sum_\ell f_{dij\ell} \left\{ \frac{1}{R_{ij\ell}^3} + \frac{1}{R_{ij\ell}^2} \frac{\partial}{\partial \tau} \right\} J_{R_3}(z_j, \tau) \Delta S_\ell \quad (59b) \\
 & \tau = t - R_{ij\ell}
 \end{aligned}$$

where

z_i designates the band on which the observer is located.

z_j designates the band on which the integration point is located.

ϕ_ℓ designates the patch on band j on which the integration point is located.

$$f_{aij\ell} = -\cos \phi_\ell \left\{ \left[g_j \rho_j + g_{pj} (z_i - z_j) \right] \cos \phi_\ell - \rho_i g_j \right\}$$

$$f_{bij\ell} = -\sin^2 \phi_\ell (z_i - z_j)$$

$$f_{cij\ell} = \sin^2 \phi_\ell \left[g_{pj} g_i \rho_i - g_{pi} g_j \rho_j - g_{pi} g_{pj} (z_i - z_j) \right]$$

$$f_{dij\ell} = \cos \phi_\ell \left\{ \left[g_i \rho_i - g_{pi} (z_i - z_j) \right] \cos \phi_\ell - g_i \rho_j \right\}$$

$R_{ij\ell}$ = the distance between the observation point and the integration point.

ΔS_ℓ = the area of patch ℓ .

The time differentiation and interpolation necessary for the evaluation of the integrands in Eq. (59) are performed numerically by representing the surface current with a fourth-order polynomial. In order to achieve the best accuracy, the five points used for the representation were chosen such that the current would be evaluated as near as possible to the middle of them. The correction currents $J_{CR}(z_i, t)$ are computed for the time at which the leading edge of the incident field reaches z_i . This insures that all non-zero contributions to J_{CR} come from portions of the target whose geometry is already known.

For the calculation of $\rho(z, t)$ it is necessary to evaluate the time derivative of integral

$$\vec{I}(\vec{r}, t) = \int_S \left\{ \vec{J}_{CR}(\vec{r}', \tau) \times \hat{a}_r \right\} dS' \quad (60)$$

$\tau = t - R$

For the numerical implementation $\vec{I}(\vec{r}, t)$ is represented as

$$I(z, t) = \sum_i \sum_\ell \left[a_{i\ell} J_2(z_i, \tau) + b_{i\ell} J_3(z_i, \tau) \right] \Delta S_i \quad (61)$$

where

$$a_{i\ell} = -g p_i \cos^2 \phi_\ell$$

$$b_{i\ell} = -\sin^2 \phi_\ell .$$

The time derivative of the sum $I(z, t)$ is calculated using the central derivative formula

$$\frac{\partial I(z, t)}{\partial t} = \frac{I(z, t + \epsilon) - I(z, t - \epsilon)}{2\epsilon}$$

where $\epsilon = .01$.

The results obtained using this numerical implementation gave solutions which were quite close to the actual target contour. They did not, however, reproduce the contour exactly. In an attempt to improve the results, it was found that a more precise computational method was needed to account for the surface current interaction caused by the leading edge of the incident ramp waveform. The effect of the derivative in the expression for J_{CR} combined with the derivative necessary for the computation of $\rho(z,t)$ is to necessitate integrating an impulse in discrete space-time steps. This discontinuity occurs only at the leading edge of the incident ramp since the second derivative of the ramp at (z,t) is zero after the leading edge passes.

To obtain a new numerical representation the expression for the derivative of the correction currents, $\partial \vec{J}_{CR} / \partial t$ was expanded, to yield

$$\frac{\partial \vec{J}_{CR}(\vec{r}, t)}{\partial t} = \frac{1}{2\pi} \frac{\partial}{\partial t} \int_S \hat{a}_n \times \left\{ \frac{1}{R} + \frac{1}{R} \frac{\partial}{\partial \tau} \left[\vec{J}_{PO}(\vec{r}', \tau) + \vec{J}_{CR}(\vec{r}', \tau) \right] \times \hat{a}_R \right\} dS' \quad (62)$$

$\tau = t - R$

where

$$\vec{J}_{PO}(\vec{r}', \tau) = 2\hat{a}_n \times \vec{H}_R^i(\vec{r}', \tau).$$

Since the discontinuity occurs only at the leading edge, the contribution to $\partial \vec{J}_{CR} / \partial t$ due to \vec{J}_{PO} is the only portion of the equation which must be refined. It is necessary, then, to obtain a numerical representation for

$$\frac{\partial \vec{J}_{CR1}(\vec{r}, t)}{\partial t} = \frac{1}{2\pi} \frac{\partial}{\partial t} \int_S \hat{a}_n \times \left\{ \frac{1}{R} + \frac{1}{R} \frac{\partial}{\partial \tau} \left[\vec{J}_{PO}(\vec{r}', \tau) \times \hat{a}_R \right] \right\} dS' \quad (63)$$

$\tau = t - R$

For the numerical model the target is represented by a grid of circular patches. Each patch is considered to be in one of three states at time τ depending on whether the leading edge of the incident field has not yet reached, is located in, or has passed through the patch. If the

incident field has not yet reached the patch, then \vec{J}_{p0} and, consequently, $\partial \vec{J}_{CRL} / \partial t$ are zero. If the incident field has passed through the patch, then there is a contribution only from the $1/R^2$ term in Eq. (63) since the $\partial^2 \vec{J}_{p0} / \partial t^2$ is zero. For this case, Eq. (63) can be represented numerically in terms of its two components as

$$\frac{\partial J_{CRL2}(z_i, t)}{\partial t} = + \frac{1}{\pi} \sum_j \sum_l (f_{aijl} + f_{bijl} \cdot g_{pj}) \frac{1}{R_{ijl}^3} \Delta S_l \quad (64a)$$

$$\frac{\partial J_{CRL3}(z_i, t)}{\partial t} = + \frac{1}{\pi} \sum_j \sum_l (f_{cijl} + f_{dijl} \cdot g_{pj}) \frac{1}{R_{ijl}^3} \Delta S_l \quad (64b)$$

If the leading edge of the incident field is within the patch, then Eq. (63) can be expressed in terms of the fraction of the total patch area which is encompassed by the incident field. For this case, the components of $\partial \vec{J}_{CRL} / \partial t$ can be written as

$$\frac{\partial J_{CRL2}}{\partial t} = \frac{1}{\pi} \sum_j \sum_l (f_{aijl} + f_{bijl} \cdot g_{pj}) \left[\frac{1}{R_{ijl}^3} \frac{\partial A}{\partial t} + \frac{1}{R_{ijl}^2} \frac{\partial A'}{\partial t} \right] \quad (65a)$$

$$\frac{\partial J_{CRL3}}{\partial t} = \frac{1}{\pi} \sum_j \sum_l (f_{cijl} + f_{dijl} \cdot g_{pj}) \left[\frac{1}{R_{ijl}^3} \frac{\partial A}{\partial t} + \frac{1}{R_{ijl}^2} \frac{\partial A'}{\partial t} \right] \quad (65b)$$

where

$$\frac{\partial A}{\partial t} = \left[x \sqrt{a^2 - x^2} + a^2 \sin^{-1} \left(\frac{x}{a} \right) - \frac{\pi a^2}{2} \right] \frac{dx}{dt}$$

$$\frac{\partial A'}{\partial t} = -2 \sqrt{a^2 - x^2} \frac{dx}{dt}$$

$$a^2 = \frac{\Delta S}{\pi}$$

$$x = \frac{[R(\hat{a}_\rho \cdot \hat{a}_R) - t(\hat{a}_\rho \cdot \hat{a}_p)] - \sqrt{[R(\hat{a}_\rho \cdot \hat{a}_R) - t(\hat{a}_\rho \cdot \hat{a}_p)]^2 - [1 - (\hat{a}_\rho \cdot \hat{a}_p)^2][R^2 - t^2]}}{1 - (\hat{a}_\rho \cdot \hat{a}_p)^2}$$

$$\frac{dx}{dt} = \frac{-(\hat{a}_\rho \cdot \hat{a}_p) + [R(\hat{a}_\rho \cdot \hat{a}_R) - t(\hat{a}_\rho \cdot \hat{a}_p)] / \sqrt{[R(\hat{a}_\rho \cdot \hat{a}_R) - t(\hat{a}_\rho \cdot \hat{a}_p)]^2 - [1 - (\hat{a}_\rho \cdot \hat{a}_p)^2][R^2 - t^2]}}{1 - (\hat{a}_\rho \cdot \hat{a}_p)^2}$$

\hat{a}_R = unit vector from the integration point to the observation point

\hat{a}_p = unit vector in the direction of propagation of the incident field

$$\hat{a}_\rho = \frac{(\hat{a}_R - \hat{a}_p) - \hat{a}_n(\hat{a}_n \cdot \hat{a}_R - \hat{a}_n \cdot \hat{a}_p)}{|(\hat{a}_R - \hat{a}_p) - \hat{a}_n(\hat{a}_n \cdot \hat{a}_R - \hat{a}_n \cdot \hat{a}_p)|}$$

In the refinement of the numerical representation then, two different techniques are employed. The contribution to $\partial \vec{J}_{CR} / \partial t$ due to \vec{J}_{PO} is computed using Eqs. (64) or (65) depending on the state of the integration patch. For the contribution of \vec{J}_{CR} to $\partial \vec{J}_{CR} / \partial t$ in Eq. (62), the techniques devised for the direct approach are still used.

This second approach succeeded in further improving the approximations to the target contour. Although the solutions still did not exactly reproduce the target geometry, they have two basic advantages over the previous approach. First the contours produced tend to be more smooth than those previously obtained and secondly, the techniques itself yields a more stable solution. The results presented in Section 4.3 were obtained using this second approach.

8.2 USEFUL DIFFERENTIAL GEOMETRY RELATIONSHIPS

Consider a surface of revolution about the z-axis, where we give the radius of rotation $\rho = \rho(z)$. Denote derivatives by $\rho' = d\rho/dz$, etc. Note that ρ' has the opposite sign of z and that ρ'' is always negative. A point

on the surface is

$$\vec{r} = (\rho \cos \phi, \rho \sin \phi, z)$$

Choose the principal coordinates $u = -z$ and $v = \phi$. We then have

$$\frac{\partial \vec{r}}{\partial u} \equiv \vec{r}_u = (-\rho' \cos \phi, -\rho' \sin \phi, -1), \text{ where } E \equiv |\vec{r}_u|^2 = 1 + \rho'^2,$$

$$\frac{\partial \vec{r}}{\partial v} \equiv \vec{r}_v = (-\rho \sin \phi, \rho \cos \phi, 0), \text{ where } G \equiv |\vec{r}_v|^2 = \rho^2$$

and

$$\hat{a}_u = \vec{r}_u / \sqrt{E}; \quad \hat{a}_v = \vec{r}_v / \sqrt{G};$$

and where an element of length is given by

$$(dl)^2 = E du^2 + G dv^2.$$

The unit normal is

$$\hat{a}_n = \hat{a}_u \times \hat{a}_v = \frac{\cos \phi, \sin \phi, -\rho'}{\sqrt{E}}.$$

The second order relations are

$$\frac{\partial^2 \vec{r}}{\partial u^2} \equiv \vec{r}_{uu} = (\rho'' \cos \phi, \rho'' \sin \phi, 0)$$

$$\frac{\partial^2 \vec{r}}{\partial v^2} \equiv \vec{r}_{vv} = (-\rho \cos \phi, -\rho \sin \phi, 0)$$

with

$$L \equiv \vec{r}_{uu} \cdot \hat{a}_n = \rho'' / \sqrt{E}$$

$$N \equiv \vec{r}_{vv} \cdot \hat{a}_n = -\rho / \sqrt{E}$$

The principal curvatures are then

$$K_u = \frac{L}{E} = \rho''/E^{3/2}$$

$$K_v = \frac{N}{G} = -1/(\rho\sqrt{E})$$

For a prolate spheroid both curvatures are < 0 . For a cylinder $K_u = 0$ and $K_v < 0$. Our choice of principal coordinates assures that

$$F \equiv \vec{r}_u \cdot \vec{r}_v = 0$$

and

$$M \equiv \vec{r}_{uv} \cdot \hat{a}_n = 0.$$

8.3 INTEGRATION OVER SELF-PATCH

The following differs from previous formulations [4] by the inclusion of the effect of retardation of the surface current over the self-patch. The expression for the surface current is

$$\vec{J}(\vec{r}, t) = \frac{1}{2\pi} \int_S \hat{a}_n \times \{ \oint \vec{J}(\vec{r}', t) \times \hat{a}_R \} dS' . \quad (66)$$

We wish to evaluate the part of this integral due to patch S_ϵ containing r by direct integration.

$$\vec{J}_\epsilon(\vec{r}, t) = \frac{1}{2\pi} \int_{S_\epsilon} \hat{a}_n \times \{ \oint \vec{J}(\vec{r}', t) \times \hat{a}_R \} dS' , \quad (67)$$

where

\hat{a}_n is the unit normal at \vec{r}

$$R = |\vec{R}| = |\vec{r} - \vec{r}'|$$

$$\hat{a}_R = \vec{R}/R$$

$$\tau = t - R$$

$$\nabla = \frac{1}{R} \frac{\partial}{\partial \tau} + \frac{1}{R} \frac{\partial}{\partial \tau}$$

Write \vec{R} as a Taylor expansion about \vec{r} :

$$-\vec{R} = \vec{r}' - \vec{r} = \vec{r}_u du + \vec{r}_v dv + \frac{1}{2} \vec{r}_{uu} du^2 + \frac{1}{2} \vec{r}_{vv} dv^2 + \vec{r}_{uv} dudv, \quad (68)$$

where u, v are principal coordinates. Using the relationships of Appendix 8.2 we form:

$$\hat{a}_n \cdot \hat{a}_R = -\frac{1}{2R} (EK_u du^2 + GK_v dv^2). \quad (69)$$

Separate $\vec{J}(\vec{r}', \tau)$ into its two components

$$\vec{J}(\vec{r}', \tau) = J_u' \hat{a}_u' + J_v' \hat{a}_v', \text{ where}$$

$$\vec{r}_u' = \vec{r}_u + \vec{r}_{uu} du + \vec{r}_{uv} dv, \text{ hence}$$

$$\hat{a}_u' = \hat{a}_u + \frac{\vec{r}_{uu}}{\sqrt{E}} du + \frac{\vec{r}_{uv}}{\sqrt{E}} dv, \text{ and similarly} \quad (70)$$

$$\hat{a}_v' = \hat{a}_v + \frac{\vec{r}_{vv}}{\sqrt{G}} dv + \frac{\vec{r}_{uv}}{\sqrt{G}} du.$$

Expanding the vector triple product in (67) and considering only the J_u' component to second order:

$$\begin{aligned}
\hat{a}_n \times \left\{ \oint J'_u \hat{a}'_u \times \hat{a}_R \right\} &= \oint J'_u \left\{ \left[(\hat{a}_n \cdot \hat{a}_R) \hat{a}'_u \right] - \left[(\hat{a}_n \cdot \hat{a}'_u) \hat{a}_R \right] \right\} \\
&= \oint J'_u \left\{ \left[-\frac{\hat{a}_u}{2R} (EK_u du^2 + GK_v dv^2) \right] + \left[\hat{a}_u \frac{EK_u du^2}{R} + \dots \right] \right\} \quad (71) \\
&= \oint J'_u \frac{\hat{a}_u}{2R} (EK_u du^2 - GK_v dv^2) .
\end{aligned}$$

In the above, terms in odd powers of du or dv have been omitted, because their contributions will cancel when integrating. Similarly, for the J'_v component, obtain

$$\hat{a}_n \times \left\{ \oint J'_v \hat{a}'_v \times \hat{a}_R \right\} = \oint J'_v \frac{\hat{a}_v}{2R} (GK_v dv^2 - EK_u du^2) . \quad (72)$$

We can expand

$$J_u(\vec{r}', \tau) = J_u(\vec{r}, t) + R \frac{\partial J_u(\vec{r}, t)}{\partial R} + (\tau - t) \frac{\partial J_u(\vec{r}, t)}{\partial t}$$

We now assume that J_u is the same everywhere on the patch; ie.

$$\frac{\partial J_u}{\partial R} = 0 \quad \text{and} \quad \frac{\partial J_u(\vec{r}', \tau)}{\partial \tau} = \frac{\partial J_u(\vec{r}, t)}{\partial t}$$

then

$$\oint J'_u = \frac{J_u(\vec{r}', \tau)}{R^2} + \frac{\partial J_u(\vec{r}', \tau)}{R \partial t} = \frac{J_u(\vec{r}, t)}{R^2}$$

Similarly,

$$\oint J'_v = \frac{J_v(\vec{r}, t)}{R^2} .$$

The quantities J'_u , J'_v and \hat{a}_u , \hat{a}_v can thus be taken outside the integral of Eq. (67), which can be rewritten

$$\vec{J}_\epsilon(\vec{r}, t) = \frac{1}{4\pi} \left[J_u(\vec{r}, t) \hat{a}_u - J_v(\vec{r}, t) \hat{a}_v \right] \int_{S_\epsilon} \frac{(EK_u du^2 - GK_v dv^2)}{R^3} dS' \quad (73)$$

We will integrate over a circular patch of radius R_0 , by letting

$$\sqrt{E} du = R \cos \theta ; \sqrt{G} dv = R \sin \theta ; \text{ and } dS' = R dR d\theta$$

This integration yields

$$\vec{J}_\epsilon(\vec{r}, t) = \left[\hat{a}_u J_u(\vec{r}, t) - \hat{a}_v J_v(\vec{r}, t) \right] \left[\frac{(K_u - K_v)}{4} \right] R_0 \quad (74)$$

We will have occasion to use the abbreviation

$$\zeta = \frac{(K_u - K_v)}{4} R_0 . \quad (75)$$

Rewriting Eq. (66), we can substitute the above result:

$$\begin{aligned} \vec{J}(\vec{r}, t) &= \vec{J}_\epsilon(\vec{r}, t) + \frac{1}{2\pi} \int_{S-S_\epsilon} \dots dS' \\ &= \hat{a}_u \zeta J_u - \hat{a}_v \zeta J_v + \frac{1}{2\pi} \int_{S-S_\epsilon} \dots dS' , \end{aligned}$$

where the integrals are now over the reduced area, excluding the self-patch.

Hence:

$$\left\{ \begin{aligned} J_u(\vec{r}, t) &= \frac{1}{1-\zeta} \left[\frac{1}{2\pi} \int_{S-S_\epsilon} \dots dS' \right]_u \\ J_v(\vec{r}, t) &= \frac{1}{1+\zeta} \left[\frac{1}{2\pi} \int_{S-S_\epsilon} \dots dS' \right]_v \end{aligned} \right. \quad (76)$$

It will sometimes be convenient to write this as

$$\vec{J}(\vec{r}, t) = \frac{1}{\gamma} \frac{1}{2\pi} \int_{S - S_E} \dots dS',$$

where γ is understood to be evaluated in the above manner by separating into components. (If one of the components is zero, $\gamma = 1 \pm \zeta$.)

8.4 TRANSFORMATION OF SELF-PATCH CORRECTION TO THE INCIDENT H COORDINATE SYSTEM

The quantity to be evaluated in the far field integral Eq. (30) is

$$\vec{J}(\vec{r}, t) \times \hat{a}_{r_o}.$$

We are interested in simplifying the first order physical optics contribution

$$\frac{\vec{J}^{inc}}{\gamma} \times \hat{a}_{r_o}, \text{ where } \vec{J}^{inc} = 2\hat{a}_n \times \vec{H}^{inc},$$

γ is defined in Appendix 8.3, and

\hat{a}_{r_o} is the direction of the far field which is assumed to lie in the yz plane at angle α with the z axis.

The incident field \vec{H}^{inc} travels in the negative \hat{a}_{r_o} direction.

$$\vec{H}^{inc}(\vec{r}, t) = H^{inc}(r, t) \cdot \hat{a}_H$$

where

$$\hat{a}_p = \hat{a}_x \times \hat{a}_{r_o}$$

and where either

$$\hat{a}_H = \hat{a}_x ; \text{ TM mode, or}$$

$$\hat{a}_H = \hat{a}_p ; \text{ TE mode.}$$

$$\frac{\vec{J}^{inc}}{\gamma} = \frac{J_u^{inc} \hat{a}_u}{1 - \zeta} + \frac{J_v^{inc} \hat{a}_v}{1 + \zeta}$$

Consider the TM mode: $\hat{a}_H = \hat{a}_x$

$$J_u^{inc} = 2\hat{a}_u \cdot (\hat{a}_n \times \hat{a}_x) H^{inc}$$

$$J_v^{inc} = 2\hat{a}_v \cdot (\hat{a}_n \times \hat{a}_x) H^{inc}$$

It is convenient to write out the various unit vectors in Cartesian form:

$$\hat{a}_x = (1, 0, 0)$$

$$\hat{a}_{r_o} = (0, \sin \alpha, \cos \alpha)$$

$$\hat{a}_p = (0, -\cos \alpha, \sin \alpha)$$

$$\hat{a}_n = (n_x, n_y, n_z)$$

$$\hat{a}_u = (u_x, u_y, u_z)$$

$$\hat{a}_v = (v_x, v_y, 0),$$

making use of the assumption that the target is a body of rotation about the z-axis (see Appendix 8.2).

$$\hat{a}_u \cdot (\hat{a}_n \times \hat{a}_x) = u_y n_z - n_y u_z$$

$$\hat{a}_v \cdot (\hat{a}_n \times \hat{a}_x) = v_y n_z$$

$$\hat{a}_u \times \hat{a}_{r_o} = (u_y \cos \alpha - u_z \sin \alpha, -u_x \cos \alpha, u_x \sin \alpha)$$

$$\hat{a}_v \times \hat{a}_{r_o} = (v_y \cos \alpha, -v_x \cos \alpha, v_x \sin \alpha)$$

Consider now two points symmetric about the yz plane: the quantities u_x , v_y , and n_x have opposite signs. Hence neglecting terms that will cancel when integrating:

$$\frac{\vec{J}}{\gamma} \times \hat{a}_{r_o} = 2H^{inc} \hat{a}_x \frac{u_y n_z - n_y u_z}{1 - \zeta} \frac{u_y \cos \alpha - u_z \sin \alpha}{1 - \zeta} + \frac{v_y^2 n_z \cos \alpha}{1 + \zeta}$$

Only for the case $\alpha = 90^\circ$ (broadside incidence), this reduces to simply

$$\frac{\vec{J}}{\gamma} \times \hat{a}_{r_o} ds = \frac{2H^{inc} \hat{a}_x ds_{proj}}{(1 - \zeta)},$$

where

$$ds_{proj} = (\hat{a}_n \cdot \hat{a}_{r_o}) ds.$$

In the above, the expressions in Appendix 8.2 were used. Using a similar procedure we find that for the other polarization $\hat{a}_H = \hat{a}_p$:

$$\frac{\vec{J}}{\gamma} \times \hat{a}_{r_o} ds = \frac{2H^{inc} \hat{a}_p}{(1 + \zeta)} ds_{proj},$$

if and only if $\alpha = 90^\circ$.

8.5 PROJECTED AREA OF NEWLY ILLUMINATED REGION

The projected area of the new region needs to be related to its orientation in order to determine the coordinates and derivatives of the new region.

The region is illustrated in cross-section and perspective in Fig. 41. It is a slice of a skewband about the body of rotation. We

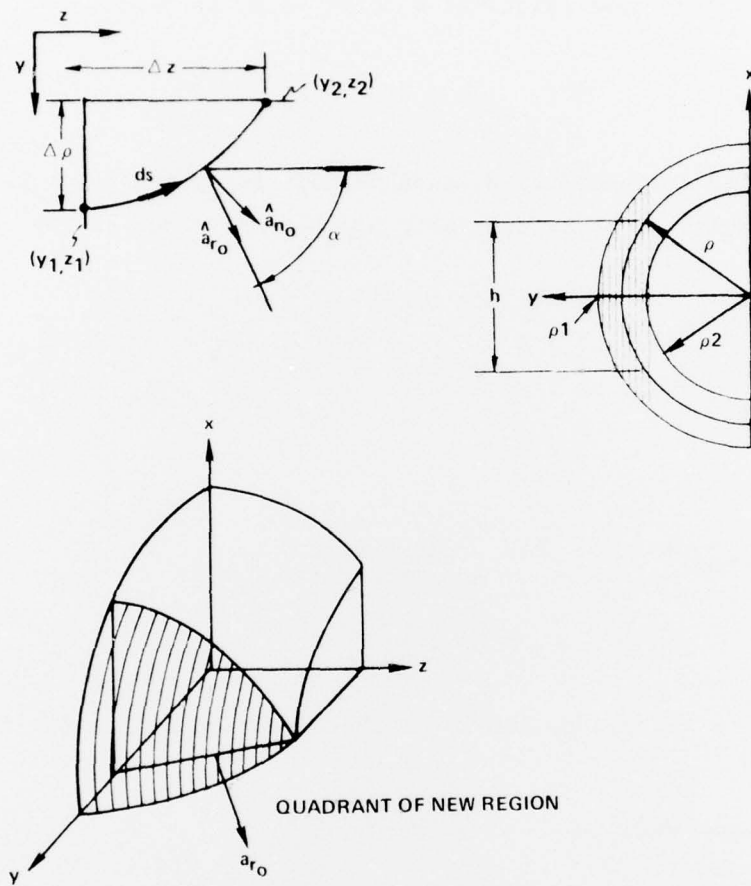


FIG. 41 Projected area of newly illuminated region.

consider first only one side of the new region, although in general there will be two disconnected pieces.

The projected height at a point (y,z) is given by

$$h = 2\sqrt{\rho^2 - \rho_2^2},$$

where ρ_2 is the radius of revolution through the point (y_2, z_2) , the far edge of the new region. Define similarly ρ_1 , the near edge of the region.

Let \hat{a}_{n_o} be the surface normal at $x=0$

$$\hat{a}_{n_o} = (0, 1, -\rho')/\sqrt{1 + \rho'^2}$$

then

$$\Delta S_{\text{proj}} = \int_{s_1}^s h(\hat{a}_{n_o} \cdot \hat{a}_{r_o}) ds,$$

where

$$\hat{a}_{r_o} = (0, \sin \alpha, \cos \alpha) \text{ is the direction to the far field.}$$

This expression needs to be simplified.

The average value of h is

$$h_{\text{av}} = \frac{1}{2} (h_1 - h_2) = \sqrt{(\rho_1 + \rho_2)(\rho_1 - \rho_2)} \approx \sqrt{2\rho\Delta\rho}$$

where ρ is the average of ρ_1, ρ_2 and $\Delta\rho = \rho_1 - \rho_2$. If ρ is taken as the value in the region center, h_{av} is then an underestimate of the effective h .

An upper limit on the effective h is

$$h_t = 2\sqrt{\rho^2 - \rho_2^2} = 2\sqrt{\rho\Delta\rho}$$

where again ρ is the value in the center.

Here we take an intermediate value

$$h_{\text{eff}} = \frac{\pi}{2} \sqrt{\rho \Delta \rho},$$

which is also the value obtained for a sphere, which can be calculated exactly. Also note that

$$ds = dz \sqrt{1 + \rho'^2}$$

Hence obtain

$$\Delta S_{\text{proj}} = \frac{\pi}{2} \sqrt{\rho \Delta \rho} (\Delta z \sin \alpha + \Delta \rho \cos \alpha),$$

where $\Delta \rho = \rho_1 - \rho_2$ and $\Delta z = z_2 - z_1$.

In the case of general oblique incidence, the ΔS on the two sides are different, but in the case of $\alpha = 90^\circ$ we multiply the above by 2, to account for both sides. For the case of $\alpha = 90^\circ$, including both pieces of the new region, we write

$$\Delta z = \frac{\Delta S_{\text{proj}}}{\pi \sqrt{\rho \Delta \rho}};$$

i.e. we can obtain Δz and hence $\rho' = \Delta \rho / \Delta z$ since ΔS_{proj} and $\rho \Delta \rho$ are known from the far field response.

In the case of $\alpha = 0^\circ$, it is simpler to use the fact of rotational symmetry and write

$$\Delta S_{\text{proj}} = \pi (\rho_2^2 - \rho_1^2)$$

or

$$\rho = \frac{1}{2} \left(\rho_1 + \sqrt{\rho_1^2 + \frac{\Delta S_{\text{proj}}}{\pi}} \right)$$

For general oblique incidence, the main problem is in determining the relative size of the regions on each side.

8.6 INITIAL RAMP RESPONSE OF SPECULAR POINT

As a first step in the inverse scattering process, the leading edge of the ramp response is analyzed in order to obtain the geometric characteristics of the specular point. The response of a curvilinear patch was derived in Section 5.3. Specializing those results to the specular point and writing S for the projected area and t for the time since incidence gives:

$$\begin{aligned} r_{oHr}(t) = & \frac{1}{2\pi} \frac{dS}{dt} \Big|_0 t + \frac{1}{2\pi} \frac{d^2S}{dt^2} \Big|_0 \frac{t^2}{2} \pm \frac{(K_u - K_v)}{4\pi} \frac{dS}{dt} \Big|_0 \frac{t^2}{2} \\ & + \left(\frac{3}{2} \left(\frac{K_u - K_v}{2} \right)^2 \frac{dS}{dt} \Big|_0 \pm \frac{(K_u - K_v)}{2} \frac{d^2S}{dt^2} \Big|_0 \right) \frac{t^3}{6} \end{aligned} \quad (77)$$

The first two terms are the projected area to second order; the last terms are the polarization dependent physical optics corrections, where the sign is + for x polarization and - for y polarization.

The derivation of the above assumed that both curvatures were non-zero. Additional terms arise if only one of the curvatures is non-zero as in the case of a cylinder viewed at broadside.

The projected area of a cylinder viewed at broadside is

$$S = 2L \sqrt{t(a - t/4)},$$

where a is the radius. At t close to zero we can approximate

$$dS = 2L \sqrt{a} t^{-\frac{1}{2}} dt.$$

We use this expression for dS in Eq. (48) for the integral over the self-patch to obtain the next, polarization dependent term:

$$r_{or} H_r(t) = \frac{L\sqrt{a}}{\pi} t^{\frac{1}{2}} \pm \frac{L}{6\pi\sqrt{a}} t^{3/2} + r_{or} H_r^{\text{cap}}(t) \quad (78)$$

In the above, we have used the facts that $K_u = 0$, $K_v = -\frac{1}{a}$, and where H_r^{cap} is the initial ramp response of the caps as given by Eq. (77). The + sign in the polarization dependent term refers to the case of x-polarization, the - sign to p-polarization.

In the inverse procedure we take the average of the responses at the two polarizations and test for the presence of a $t^{\frac{1}{2}}$ dependence. The coefficient of this dependence, by Eq. (78), is expected to be

$$G \equiv \frac{L\sqrt{a}}{\pi} \quad (79)$$

From the remaining terms due to the caps, the two principal curvatures at the cap-side of the boundary, and hence, the radius a is determined by the methods of Section 5.3. Eq. (79) then gives the length of the cylinder body.

For reference, the ideal specular response of a prolate spheroid is evaluated. The area function of a prolate spheroid viewed at angle α with respect to the z -axis (axis of rotational symmetry) is

$$S(t) = \pi a^2 b (t\sqrt{B} - t^2/4) / B^{3/2},$$

where

$t=0$ at time of incidence at the specular point,

a, b are the ellipse axes

b is the axis of rotation (\hat{z})

$$B = b^2 \cos^2 \alpha + a^2 \sin^2 \alpha.$$

Taking the derivatives of the above, evaluating at $t=0$ and substituting in Eq. (77) yields

$$r_{O H_r}(t) = \frac{a^2 b}{2B} t - \frac{a^2 b}{4B^{3/2}} \frac{t^2}{2} \pm \frac{a^2 b}{2B} \left(\frac{K_u - K_v}{2} \right) \frac{t^2}{2} \\ + \left\{ \frac{3}{2} \left(\frac{K_u - K_v}{2} \right)^2 \frac{a^2 b}{2B} \mp \left(\frac{K_u - K_v}{2} \right) \frac{a^2 b}{4B^{3/2}} \right\} \frac{t^3}{6} . \quad (80)$$

The top signs here refer to the x-polarization.

At broadside ($\alpha = 90^\circ$), which is the test case of this report, the above reduces to

$$r_{O H_r}(t) = \frac{b}{2} t - \frac{b}{4a} \frac{t^2}{2} \pm \frac{b}{2} \left(\frac{K_u - K_v}{2} \right) \frac{t^2}{2} + \left\{ \frac{3}{2} \left(\frac{K_u - K_v}{2} \right)^2 \frac{b}{2} \mp \left(\frac{K_u - K_v}{2} \right) \frac{b}{4a} \right\} \frac{t^3}{6} \quad (81)$$

For a sphere, both polarizations reduce to

$$r_{O H_r}(t) = \frac{a}{2} t - \frac{1}{4} \frac{t^2}{2} . \quad (82)$$

*MISSION
of
Rome Air Development Center*

RADC plans and conducts research, exploratory and advanced development programs in command, control, and communications (C³) activities, and in the C³ areas of information sciences and intelligence. The principal technical mission areas are communications, electromagnetic guidance and control, surveillance of ground and aerospace objects, intelligence data collection and handling, information system technology, ionospheric propagation, solid state sciences, microwave physics and electronic reliability, maintainability and compatibility.

